CONFINED BOILING HEAT TRANSFER OVER A SATURATED POROUS STRUCTURE

CONFINED BOILING HEAT TRANSFER OVER A SATURATED POROUS STRUCTURE

By

MEROUANE KHAMMAR, B. Eng.

A Thesis

Submitted to the School of Graduate Studies

In Partial Fulfillment of the Requirements of the Degree

Master of Applied Science

McMaster University, Hamilton, Ontario, Canada

MASTER OF APPLIED SCIENCE (2004) MCMASTER UNIVERSITY

(Mechanical Engineering) Hamilton, Ontario, Canada

TITLE: Confined Boiling Heat Transfer Over a Saturated Porous Structure.

AUTHOR: Merouane Khammar, B.Eng. Mechanical Engineering, Ecole Nationale Polytechnique, Algiers, Algeria

SUPERVISORS: Dr.C.Y.Ching and Dr.D.Ewing

NUMBER OF PAGES: xvi, 107

Abstract

An experimental investigation was performed to study the confined boiling heat transfer characteristics over a saturated porous structure using distilled water as the working fluid. A thin stainless steel resistive foil stretched between two copper electrodes was used to heat a saturated porous plate with an effective pore size of 50 μm. The temperature distribution on the foil heater was measured using a high speed thermal imaging camera. The effect of the gap height between the heater and the porous plate on the heat transfer was investigated for gap heights ranging from 0 μm to 1000 μm and for heat fluxes ranging from 11.7 kW/m^2 to 58.3 kW/m^2. It was observed that the highest heat transfer rate was obtained at a gap height of approximately 600 μm. The main heat transfer mechanism is thought to be confined boiling in the small gap between the heating surface and the saturated porous structure. It was observed that the effect of the subcooled liquid temperature did not have a significant effect on the heat transfer. The effect of the pore size in the porous plate was investigated by repeating the measurements with a porous plate of 200 μm pore size. It was observed that the thermal resistance for the plate with a 200 μm pore size was significantly higher than the plate with 50 μm pores for gaps less than 300 μm. At a larger gap height of 600 μm, similar heat transfer performances were obtained for the two porous media.

Acknowledgments

The author dedicates this thesis to his parents, sisters Wafaa and Habiba, brother Hichem, and to Djamila.

The author also wishes to express his gratitude to his supervisors Dr. C.Y.Ching and Dr. D.Ewing for their continuous encouragement and advice through the course of this study.

The author greatly appreciates the time and effort of Dr R. Judd and Dr J.S. Chang in reviewing this thesis.

Gratitude is also extended to Mr Andrew Buyers, Mr Ron Lodewyks, Mr Dave Schick, and Mr. Joe Verhaeghe for their help through all stages of this project.

Table of content

Chapter 1.	Introduction	1
Chapter 2.	Literature Review	
	2.1. Review of the heat transfer investigations of the capillary evaporator	5
	2.2. Review of boiling in a confined space	16
Chapter 3.	Experimental Facility and Methodology	
	3.1. Experimental facility	25
	3.2. Experimental procedure	33
	3.3. Evaluation of the energy balance	35
	3.4. Error analysis	37
Chapter 4.	Experimental Results and Discussion	
	4.1. Effect of the gap height on the confined boiling	39
	4.2. Effect of the subcooled liquid temperature on the confined boiling	68
	4.3. Effect of the pore size on the confined boiling	80
	4.4. Discussion and proposed model	95
Chapter 5.	Conclusions and Recommendations	
	5.1. Conclusions	100
	5.2. Recommendations	101
References		103

List of Figures

1.1. Schematic of a typical capillary pumped loop. 2

1.2. Cross section of a typical evaporator used in capillary pumped loops. 2

2.1. Two dimensional model of the capillary evaporator proposed by Cao et al(1994a). 7

2.2. Three dimensional capillary evaporator model proposed by Cao et al(1994b). 7

2.3. Heat transfer coefficient versus heat flux obtained by Khrustalev et al(1995). 9

2.4. Heat transfer operating conditions of the capillary evaporator proposed by Demidov et al(1994), for (a) at low heat fluxes, (b) at high heat fluxes. 11

2.5. Variation of the heat transfer coefficient with heat flux during evaporation from a saturated porous structure obtained by Zhao et al (2000a), ■ Theoretical predictions, □ Experimental results. 15

2.6. Gap between the heating fin and the saturated wick proposed by Figus et al(1996). 15

2.7. Schematics of the thin liquid film on the heating surface during boiling of water in a confined gap of 0.97mm obtained by Ishibashi et al(1969). 17

2.8. Effect of the gap size S on an upward facing confined boiling

obtained by Katto et al (1977). Δ S=0.1mm, ○ S=0.2mm,
□ S= 0.5mm, ■ S=1.0mm. 17

2.9. Boiling phenomena in confined gaps as described by Yao et al(1983). 19

2.10. Boiling curve for water at atmospheric pressure in a confined annulus obtained by Yao et al(1983). For gap sizes of: ▲ S=0.32mm,
■ S=0.80mm, ● S=2.58mm. 19

2.11. Boiling map generated by Yao et al (1983) defining the boundaries between different confined boiling regimes. 21

2.12. Experimental results obtained by Fujita et al(1988) for gap sizes of ▲ 0.6mm, ■ 2.0mm and predictions of the sensible and latent heat model for gap sizes of Δ 0.6mm, □ 2.0mm. 21

2.13. Schematic of the liquid flow to the microlayer region driven by the capillary pressure proposed by Lee et al (1992). 1. Dry region 2. Interline evaporating region 3. Bulk layer region 4. Liquid vapor interface. δ_0. Equilibrium film thickness. 23

3.1. Schematic of the experimental facility. 26

3.2. Schematic of the test section. 28

3.3. Photographs of (a) the main test section, (b) the experimental facility. 29

3.4. Top view of the test section (a) schematic and (b) photograph. 30

3.5. Cross sectional view of the main test section. 32

4.1. Distribution of the time averaged temperature on the foil for (a) q''=11.7 kW/m^2, (b) q''=28.4 kW/m^2 and (c) q''=25.1 kW/m^2. 40

4.2. Distribution of the instantaneous temperature for a heat flux of 11.7 kW/m^2 when the foil was in contact with the porous plate. 42

4.3. Distribution of the instantaneous temperature for a heat flux of 18.4 kW/m^2 when the foil was in contact with the porous plate. 43

4.4. Probability density function of the temperature on the foil at zero gap height (a) on a linear scale and (b) on a logarithmic scale. 44

4.5. Change in the average foil temperature $\overline{T}_{ave}$ with heat flux for a zero gap height. 46

4.6. Change in the heat transfer coefficient $\overline{h}$ with heat flux for a zero gap height. 46

4.7. Change in the temperature distribution on the foil with heat flux for a 300 μm gap between the foil and the porous plate. 48

4.8. Change in the temperature distribution on the foil with heat flux for a 600 μm gap between the foil and the porous plate. 49

4.9. Change in the average temperature $\overline{T}_{ave}$ with heat flux for cases where the gap between the plate and the foil was (a) □ 0 μm , Δ 100 μm, + 200 μm, ◊ 300 μm and × 400 μm, (b) ○ 600 μm , Δ 700 μm, × 1000 μm. 50

4.10. Change in the average heat transfer coefficient with heat flux for cases where the gap between the foil and the porous plate was (a) □ 0 μm , Δ 100 μm, + 200 μm, , ◊ 300 μm, × 400 μm, and (b) ○ 600 μm , Δ 700 μm, × 1000 μm. 52

4.11. Instantaneous temperature distribution for cases where the gap

is 300 μm and the heat flux was 11.7 kW/m^2. 54

4.12. Instantaneous temperature distribution for cases where the gap is 300 μm and the heat flux was 18.4 kW/m^2. 55

4.13. Instantaneous temperature distribution for cases where the gap is 300 μm and the heat flux was 31.7 kW/m^2. 56

4.14. Instantaneous temperature distribution for cases where the gap is 600 μm and the heat flux was 11.7 kW/m^2. 58

4.15. Instantaneous temperature distribution for cases where the gap is 600 μm and the heat flux was 31.7 kW/m^2. 59

4.16. Instantaneous temperature distribution for cases where the gap is 600 μm and the heat flux was 58.3 kW/m^2. 60

4.17. Instantaneous temperature distribution for cases where the gap is 1000 μm and the heat flux was 11.7 kW/m^2. 61

4.18. Instantaneous temperature distribution for cases where the gap is 1000 μm and the heat flux was 31.7 kW/m^2. 62

4.19. Instantaneous temperature distribution for cases where the gap is 1000 μm and the heat flux was 51.7 kW/m^2. 63

4.20. Probability density function of the temperature distribution on the foil for a gap of 300 μm (a) on a linear scale and (b) on a logarithmic scale. 64

4.21. Probability density function of the temperature distribution on the foil for a gap of 600 μm for different heat fluxes. 66

4.22. Probability density function of the temperature distribution on

a logarithmic scale for gaps of (a) 600 μm and (b) 1000 μm. 67

4.23. Time average temperature distribution for a gap size of 0 μm and a heat flux of 11.7 kW/m^2 for (a) liquid temperature of 60°C, (b) liquid temperature of 75 °C, and (c) liquid temperature of 90°C. 70

4.24. Time averaged temperature contours for a gap of 100 μm and (i) a liquid temperature of 60°C, (ii) a liquid temperature of 75°C, (iii) a liquid temperature of 90°C, and (a) an applied heat flux of 11.7 kW/m^2, (b) an applied heat flux of 18.4 kW/m^2 and (c) an applied heat flux of 25.1 kW/m^2. 71

4.25. Time averaged temperature contours for a gap of 600 μm, (i) a liquid temperature of 60°C, (ii) a liquid temperature of 75°C, (iii) a liquid temperature of 90°C, and (a) an applied heat flux of 11.7 kW/m^2, (b) an applied heat flux of 31.7 kW/m^2, and (c) an applied heat flux of 51.7 kW/m^2. 73

4.26. Comparison of the average temperature of the foil $\overline{T}_{ave}$ for a gap of 100 μm and Δ a liquid temperature of 60°C, □ a liquid temperature of 75°C, ○ a liquid temperature of 90°C. 74

4.27. Comparison of the average temperature $\overline{T}_{ave}$ for a gap of 200 μm and Δ a liquid temperature of 60°C, □ a liquid temperature of 75°C, ○ a liquid temperature of 90°C. 74

4.28. Comparison of the average temperature $\overline{T}_{ave}$ for a gap of 600 μm and Δ a liquid temperature of 60°C, □ a liquid temperature

of 75°C, ○ a liquid temperature of 90°C. 75

4.29. Temperature distribution on the foil surface for a gap of 600 μm and a subcooled liquid temperature of 60°C, and at heat fluxes of q″ of + 11.7 kW/m^2, ○ 18.4 kW/m^2, * 45.1 kW/m^2, for (a) linear scale, (b) logarithmic scale. 77

4.30. Temperature distribution on the foil surface for a gap of 600 μm and a liquid temperature of 75°C and at heat fluxes q″ of + 11.7 kW/m^2, ○ 18.4 kW/m^2, * 45.1 kW/m^2 , for (a) linear scale, (b) logarithmic scale. 78

4.31. Temperature distribution on the foil surface for a gap of 600 μm and a liquid temperature of 90°C, and at heat fluxes q″ of + 11.7 kW/m^2, ○ 18.4 kW/m^2, * 45.1 kW/m^2 for (a) linear scale, (b) logarithmic scale. 79

4.32. Distribution of the time averaged temperature for a gap of 0 μm at a heat flux of 11.7 kW/m^2 and a liquid temperature of 75°C for (a) a pore size of 50 μm (b) a pore size of 200 μm. 81

4.33. Distribution of the time averaged temperature on the foil for a gap of 100 μm for (i) a pore size of 50 μm and (ii) a pore size of 200 μm and (a) an applied heat flux of 11.7 kW/m^2, (b) an applied heat flux of 18.4 kW/m^2, and (c) an applied heat flux of 25.1 kW/m^2. 82

4.34. Distribution of the time averaged temperature for a gap of 200 μm, (i) a pore size of 50 μm (ii) a pore size of 200 μm and applied heat fluxes of (a) 11.7 kW/m^2, (b) 18.4 kW/m^2, (c) 25.1 kW/m^2 and (d) 31.7 kW/m^2. 84

4.35. Distribution of the time averaged temperature contours for a gap of

600 μm and (i) a pore size of 50 μm (ii) a pore size of 200 μm,
at applied heat fluxes of 11.7 kW/m^2, (b) 31.7 kW/m^2 and (c) 51.7 kW/m^2. 85

4.36. Comparison of the average temperature $\overline{T}_{ave}$ for a gap of
100 μm on the plates with □ 50 μm pore size , Δ 200 μm pore size. 86

4.37. Comparison of the average temperature $\overline{T}_{ave}$ for a gap of 200 μm
on the plates with □ 50 μm pore size , Δ 200 μm pore size. 86

4.38. Comparison of the average temperature $\overline{T}_{ave}$ for a gap of 600 μm
on the plates with □ 50 μm pore size , Δ 200 μm pore size. 87

4.39. Temperature distribution on the foil surface for a gap of 200 μm
and a pore size of 50 μm, and at heat fluxes q″ of + 11.7 kW/m^2,
○ 18.4 kW/m^2 for (a) linear scale, (b) logarithmic scale. 89

4.40. Temperature distribution on the foil surface for a gap of 200 μm
and a pore size of 200 μm and at heat fluxes q″ of + 11.7 kW/m^2,
○ 18.4 kW/m^2 for (a) linear scale, (b) logarithmic scale. 90

4.41. Temperature distribution on the foil surface for a gap of 600 μm
and a pore size of 50 μm and at heat fluxes q″ of + 11.7 kW/m^2,
○ 18.4 kW/m^2, * 45.1 kW/m^2 for (a) Linear scale, (b) Logarithmic scale. 93

4.42. Temperature distribution on the foil surface for a gap of 600 μm
and a pore size of 200 μm and at heat fluxes q″ of + 11.7 kW/m^2,
○ 18.4 kW/m^2, * 45.1 kW/m^2 for (a) linear scale, (b) logarithmic scale. 94

4.43. Schematic of the proposed heat transfer mechanisms during boiling
in a confined gap over a saturated porous structure. 96

List of Tables

Table 3.1. List of variables and uncertainties for the applied heat flux. 38

Nomenclature

A	Area of the heating surface, m^2.
a_l	Thermal diffusivity of the liquid, m^2/s.
B_l	Boiling number, $\left(\frac{q_w L}{h_{fg}\rho_g SV}\right)$.
Bo	Bond number, $\frac{S}{\left[\sigma / g(\rho_l - \rho_g)\right]^{\frac{1}{2}}}$.
D	Diameter of annulus gap, m.
q''	Heat flux, kW/m^2.
q_w	Heat flux applied on the wall, kW/m^2.
f	Void fraction.
g	Gravity acceleration, m/s^2.
$\overline{h}$	Average heat transfer coefficient, W/m^2 K.
h_{fg}	Latent heat of evaporation, kJ/kg.
I	Current, A.
k	Conductivity, W/m^2.K.
k_v	Effective conductivity of the vapor zone in the wick, W/m.K.
L	Characteristic length, m.
S	Gap between the heating surface and the porous plate, m.
t	Time, s.
T	Temperature, °C.

T_∞ Ambient temperature, °C.

$\overline{T}_{ave}$ Time and space averaged temperature of the heating surface, °C.

T_b Bulk liquid temperature, °C.

v Vapor bubble velocity, m/s.

V Electric potential across the electrodes, Volts.

β Ratio between the gap size and the pore size.

δ_l Thickness of the liquid film, m.

δ_v Thickness of the vapor zone in the wick, m.

δ_0 Equilibrium film thickness, m.

δ Thickness of the Stainless Steel foil, m.

ρ_g Density of the vapor, kg/m^3.

ρ_l Density of the vapor, kg/m^3.

σ Surface tension, N/m.

ε Emissivity of the heating surface.

Chapter 1. Introduction

Capillary pumped loops (CPL), such as that shown in figure 1.1, are passive two phase heat transfer devices that transport heat by evaporating the working fluid at a heated evaporator section and condensing it at a cooler condenser section (Faghri et al 1995). A capillary pumped loop utilizes the capillary pressure developed in a porous wick in the evaporator to circulate the working fluid in the loop. Unlike a heat pipe where the wick structure extends from the evaporator to the condenser, the CPL contains a wick structure only in the evaporator and the liquid and vapor flow through separate smooth wall tubings (Faghri et al 1995). This significantly reduces the pressure drop in the liquid return line and permits the capillary pumped loop to transport heat over long distances. Capillary pumped loops were first developed in 1960s and have been the subject of extensive research since the 1980s. Much of this research has focused on space applications because it is thought that capillary pumped loops are particularly suited for cooling electronic devices in these applications, since they don't require external power or moving mechanical parts.

A schematic of the evaporator design commonly used in capillary pumped loops is shown in figure 1.2 (Faghri et al 1995). This evaporator design consists of a metallic grooved wall with solid fins that contact a tubular porous wick structure. In this design, the subcooled liquid enters the evaporator through the center of the saturated porous

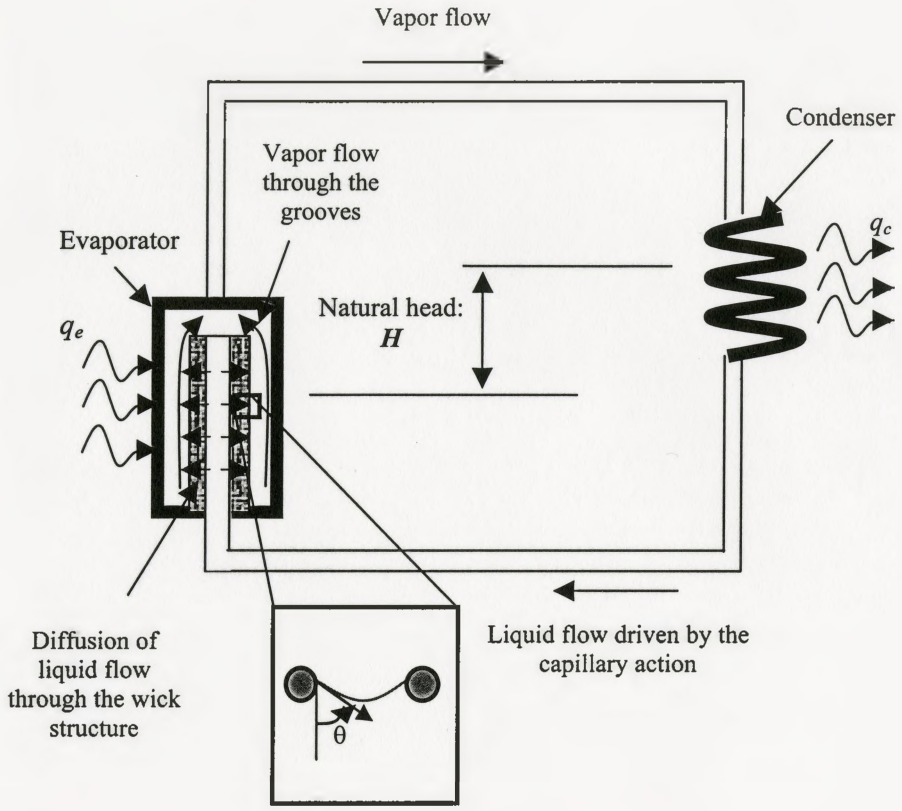

Figure 1.1. Schematic of a typical capillary pumped loop.

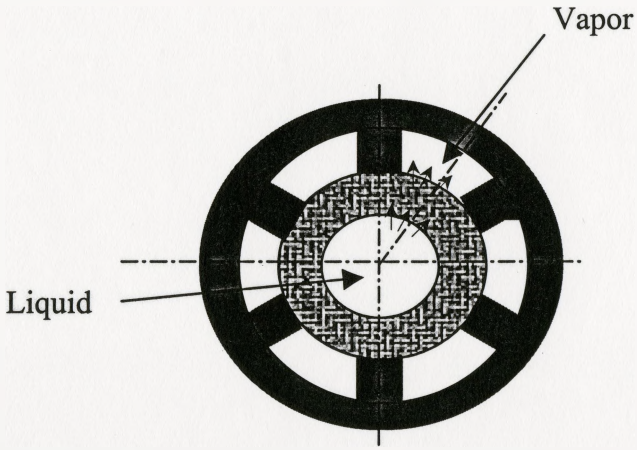

Figure 1.2. Cross section of a typical evaporator used in capillary pumped loops.

structure and passes through the wick to the outside channels. When heat is applied through the fins, the liquid boils and the vapor escapes through the grooves to the outside of the evaporator. This vapor then travels through the vapor line to the condenser. The condensed liquid is driven back to the evaporator by means of the capillary pressure developed by the evaporating meniscus on the wick surface. Thus, the capillary evaporator in the CPL provides both the heat and the driving force to the working fluid in the loop, and thus understanding the heat transfer mechanisms governing the evaporation from the wick is of significant interest in designing capillary pumped loops.

A number of investigations (eg. Embacher et al 1990, Figus et al 1996) have proposed that the heat transfer from the fin to the porous structure results in boiling at the interface between the wick structure and the heating fin. It is thought that this results in the formation of a vapor zone in the wick, which can significantly increase the thermal resistance of the capillary evaporator and potentially deprime the evaporator resulting in its failure. One method that has been proposed to overcome the formation of the vapor zone is to leave a gap between the heating fin and the porous structure, or to machine microgrooves into the heating fins that allow the vapor to escape from the gap between the fin and wick.

The objective of this investigation was to examine the effect that leaving a gap between a downward facing heating surface and a saturated porous structure has on the heat transfer in the gap. Experiments were performed by using a thin foil stretched between two electrodes to evaporate the liquid in the saturated porous structure. A high speed thermal imaging camera was used to measure the unsteady temperature distribution

on the outer surface of the heating foil. The effect that the gap size, the level of subcooling, and the pore size in the porous structure had on the heat transfer were investigated. A review of the literature related to the heat transfer in the gap is outlined in the next section. The experimental apparatus and the experimental methodology used in this investigation are then presented. The results are presented and discussed in the following section. Finally, the conclusions of the investigation are presented.

Chapter 2 Literature Review

There have been a number of investigations to develop models (eg. Embacher et al 1990, Cao et al 1994ab, Demidov et al 1994, Figus et al 1996) and experimentally characterize (eg. Wulz et al 1992, Platel et al 1996, Dupont et al 2003, Figus et al 2003) the heat transfer performance in the capillary evaporator used in capillary pumped loops. An overview of these investigations is outlined in this chapter. The geometry of the capillary evaporators with a gap between the heating fins and the porous structure suggests that confined boiling could be one of the governing heat transfer mechanisms. Thus, an overview of the previous work on boiling in confined gaps is also presented.

2.1. Review of heat transfer studies on the capillary evaporator.

One of the simplest approaches to model the heat transfer mechanisms in the capillary evaporator was to assume that the heat transferred from the heating fin was conducted through the saturated porous media to the liquid free surface under the grooves in the evaporator as shown in figure 2.1. In these cases, it was assumed that the liquid evaporates at the free interface on the wick. Cao et al (1994a) used this approach in a two-dimensional analysis of the fluid flow and heat transfer in the evaporator in order to predict the superheat at the contact between the wick and the fin. Cao et al (1994b) also

performed a conjugate heat transfer analysis of the capillary evaporator that included heat conduction through the solid fin in addition to the heat transfer through the wick and evaporation at the free interface. In this case, they also considered the three-dimensional vapor flow in the grooves (fig. 2.2). The energy and momentum equations were solved using a control volume finite difference approach. They found that the nature of the vapor flow in the grooves was highly dependent on the working fluid. In particular, the vapor velocity for freon and ammonia was negligible relative to that for water. In all cases, however, the pressure drop in the wick and the grooves was small relative to the capillary pressure.

Cao et al (1994b) proposed that any boiling that occurred at the contact surface between the fin and the porous media disturbed the meniscus in the evaporator, and caused a loss of the capillary pumping force. This would then limit the performance of the capillary evaporator. There have been a number of investigations (eg. Embacher et al 1990, Wulz et al 1992, Demidov et al 1994) that considered that boiling at the interface between the heating fin and the wick structure could be a steady state mechanism in the capillary evaporator. For example, Embacher et al (1990) considered the case where a vapor zone of constant thickness existed at the fin-wick interface. They numerically solved the steady state two dimensional momentum and energy equations for a partially heated saturated porous structure, and observed that the vapor zone in the wick would be the most significant thermal resistance in the evaporator. Embacher et al (1990) proposed that in this case, the overall heat transfer coefficient of the capillary evaporator could be approximated by

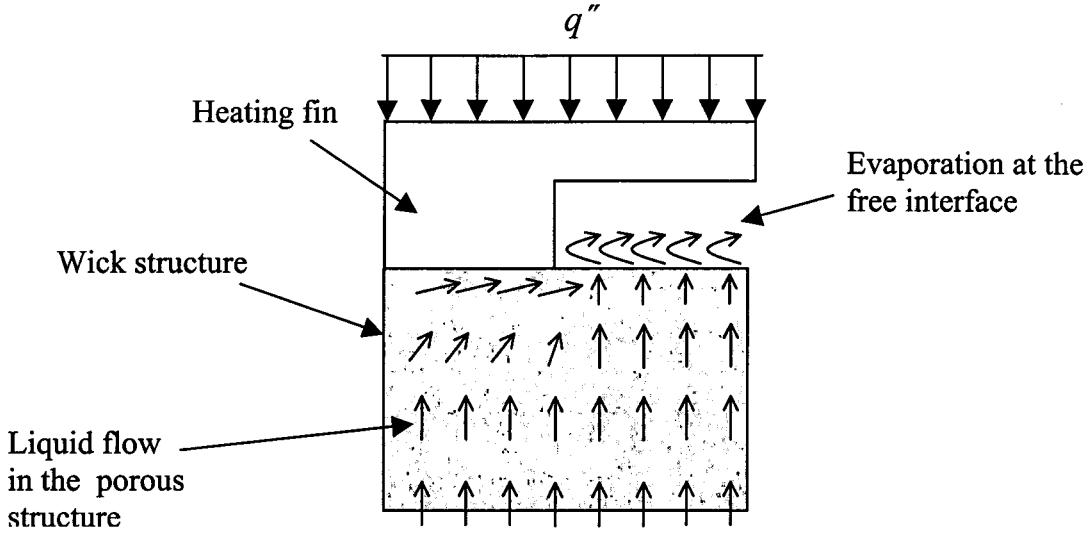

Figure 2.1. Two dimensional model of the capillary evaporator proposed by Cao et al (1994a).

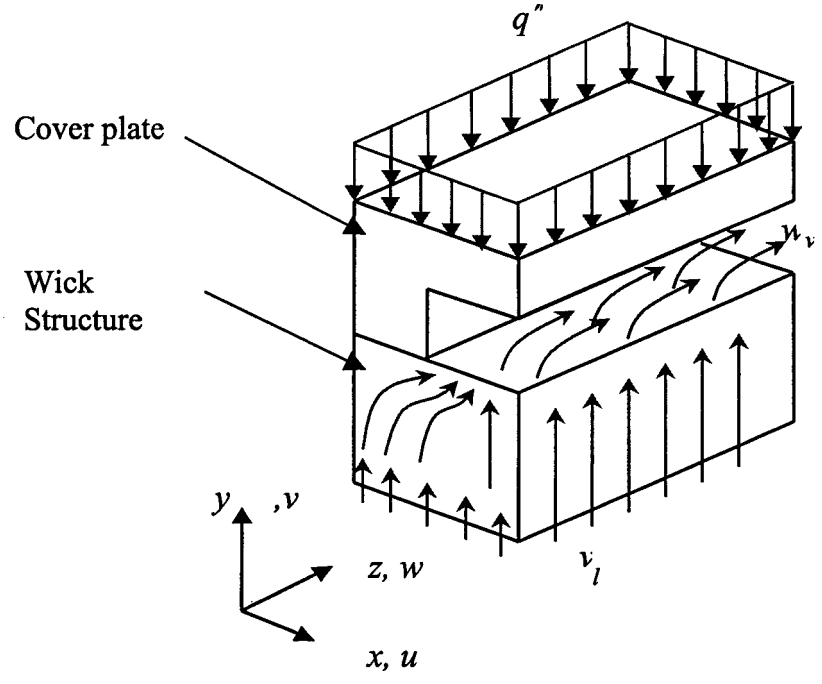

Figure 2.2. Three dimensional capillary evaporator model proposed by Cao et al (1994b)

$$\bar{h} = \frac{k_v}{\delta_v}, \tag{2.1}$$

where k_v is the effective thermal conductivity of the wick and δ is the thickness of the vapor zone in the wick. They argued that the thickness of the vapor zone δ_v was independent of the heat flux, so that the resulting heat transfer coefficient would be independent of the heat flux. Wulz et al (1992) tested the heat transfer performance of a capillary evaporator for different conditions and compared the experimental results to the model predictions of Embacher et al (1990). They observed that for low and moderate heat fluxes the heat transfer coefficient of the evaporator was constant, but it decreased at higher heat fluxes. They argued that at these higher heat fluxes the capillary evaporator was in a dry out mode, but did not provide a specific mechanism to explain the decrease of the heat transfer coefficient.

Khrustalev et al (1995) later extended the one dimensional model developed by Embacher et al(1990) to consider the heat conduction through the solid fin, heat transfer and vapor flow in the wick and meniscus evaporation from the pores. This model predicted that the thickness of the vapor blanket beneath the heating fin increased as the heat flux increased that in turn decreased the heat transfer coefficient of the evaporator as shown in figure 2.3.

The vapor zone model was extended by Demidov et al (1994) who considered a two-dimensional vapor zone in the wick and postulated there were two different operating conditions for the evaporator. At low and moderate heat fluxes, the vapor zone would be small and would not exceed the contact zone of the heating fin (fig.2.4.a).

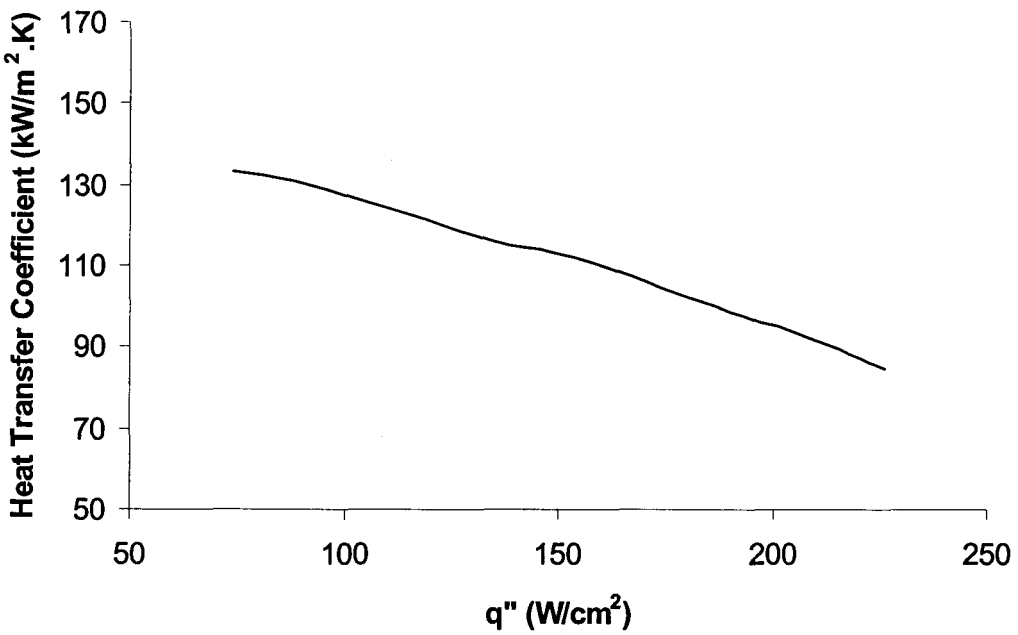

Figure 2.3. Heat transfer coefficient versus heat flux obtained by Khrustalev et al(1995).

Under these conditions, there would be a meniscus of liquid near the corner of the fin. At higher heat fluxes, however, the vapor zone could exceed the width of the heating fin so that the vapor would cover the whole heating fin surface (fig.2.4.b). This would increase the thermal resistance of the evaporator. Demidov et al (1994) numerically solved the two dimensional momentum and energy equations to determine the interfacial boundary between the liquid and the vapor for different heat fluxes, and the distribution of the temperature and pressure fields in the wick. The numerical results predicted that when the meniscus of the liquid vapor interface contacts the heating fin, the intensity of evaporation at the meniscus exceeded the evaporation at the free surface of the liquid under the groove by a factor of two to three. There were, however, no experimental measurements to validate the numerical results.

The two dimensional evolution of the vapor zone in the wick was also investigated by Figus et al (1996), who used a two dimensional numerical front tracking method to examine the expansion of the vapor zone in the wick. This model predicted that the two dimensional vapor zone expanded into the wick when the heat flux increased which significantly limited the heat transfer performance of the evaporator. Figus et al (1999) later studied the effect of the pore size distribution in the porous structure on the shape and the location of the interfacial boundary in the wick using both continuum and network models. The continuum approach was similar to the approach developed previously by Figus et al (1996), while the network approach treated the porous media as a network of sites (pores) and bonds (throats). They predicted that when the porous structure was characterized using a single pore size, the network and continuum models

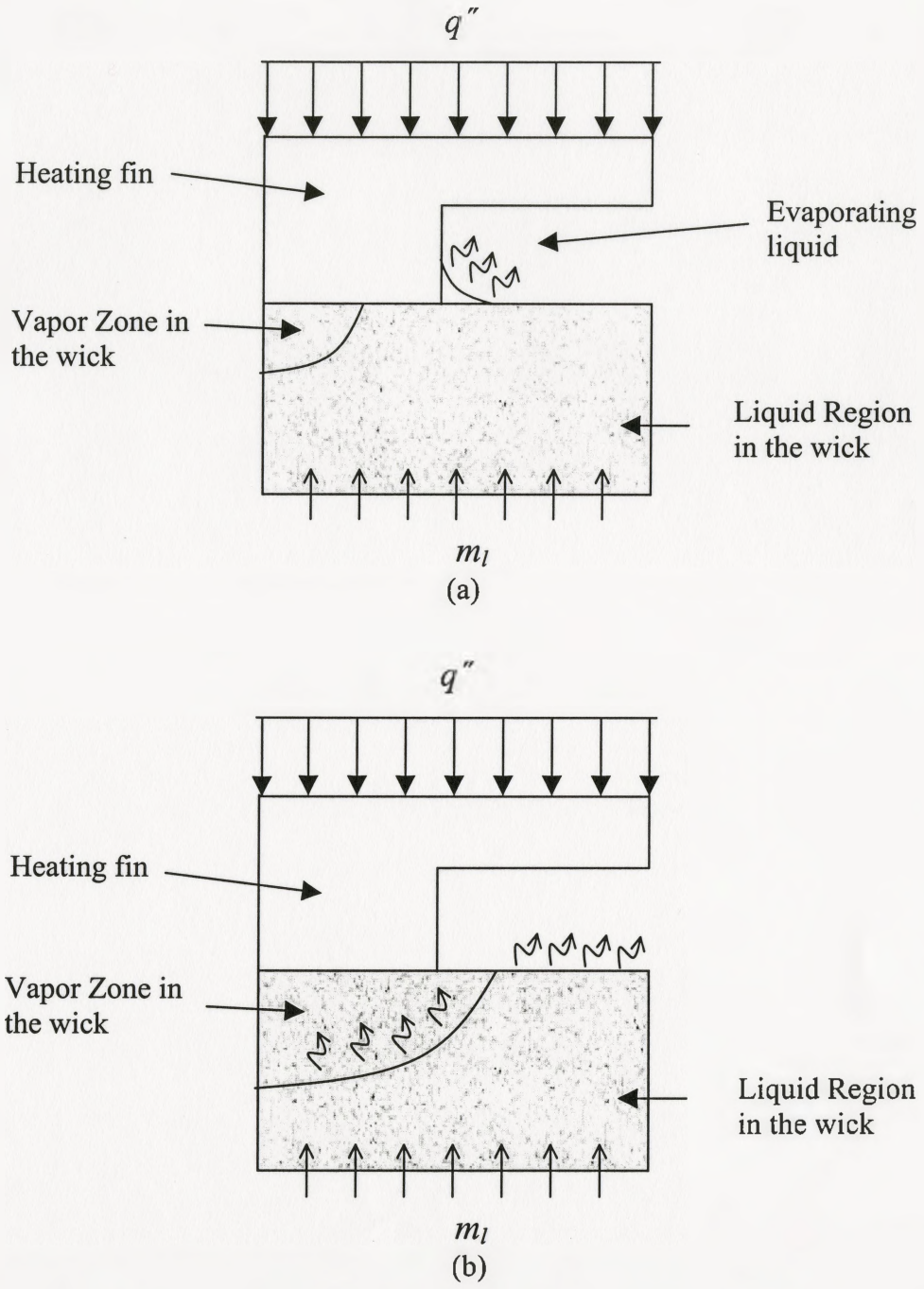

Figure 2.4. Heat transfer operating conditions of the capillary evaporator proposed by Demidov et al(1994), for (a) at low heat fluxes, (b) at high heat fluxes.

led to the same solution for the liquid-vapor front. When there was a pore size distribution, however, the network simulation predicted an earlier breakthrough of the vapor zone through the wick that would cause the evaporator to dry out. Figus et al (2003) also performed experiments using a cylindrical evaporator with a plastic wick structure to test these predictions. There was a good agreement between the experimental and simulation results for the heat transfer coefficient of the evaporator. In particular, they observed that the heat transfer coefficient decreased with the heat flux in both the experiments and the simulations.

Zhao et al (2000a) proposed that a two phase zone develops at the interface between the fin and the porous media in the capillary evaporator of the CPL. They modeled the heat transfer in this zone using a one dimensional separated flow model. The results were compared with the experimental measurements obtained for a packed glass porous media. They observed that the heat transfer coefficient in both the experiment and the model increased with heat flux until the capillary limit was reached. Thereafter, the heat transfer coefficient decreased as the heat flux increased and then decreased as a two phase zone began to expand in the wick (fig. 2.5). Yan et al (2003) used a two-dimensional numerical model with a two phase model to study the effect of the heat load, liquid subcooling, and wick conductivity on the vapor formation in the liquid core of a cylindrical capillary evaporator. They predicted that the heat applied to the outer surface of the wick was transferred by two mechanisms in these simulations. Some of the heat was conducted through the wick to the liquid core, and some transferred by convection to the interface of vaporization. It was predicted that increasing the heat flux or the liquid

flow through the wick reduced the heat conduction to the liquid core. A similar effect was observed when the wick conductivity was decreased. In both cases, this decreased the liquid core temperature and would prevent the formation of vapor in the liquid core. The same effect was also obtained when the liquid subcooling was increased.

The presence of the two-phase zone in the wick was visualized by Zhao et al (2000b) for a staggered copper cylinder porous medium heated by a finned copper block. They observed that the two-phase zone consisted of isolated bubbles that formed, grew, and then collapsed at the upper boundary of the wick. The frequency of the bubble growth cycle was found to increase from 3 Hz to 12 Hz when the applied heat flux was raised from 37 kW/m^2 to 277 kW/m^2. The macrocopic visualizations revealed that the two-phase zone in the wick expanded laterally and shrank vertically when the heat flux applied to the wick increased, which resulted in an increase of the heat transfer coefficient. They observed that the heat transfer coefficient started to decrease at higher heat fluxes when a vapor blanket began to form beneath the heating fin in the wick. The effect of the liquid inlet temperature was investigated, and it was observed that higher heat transfer performance was obtained when the temperature of the liquid below the wick approached the saturation temperature. It was argued this occurred because there were more nucleation sites created when the temperature of the bulk liquid approached the saturation temperature. The main limitation to the application of the experimental results conducted by Zhao et al (2000) was the relatively large scale of the pore size (~1mm) that makes the boiling in the pores similar to that of confined boiling. The vapor bubble dynamics would likely be different for a wick structure with smaller pore sizes

because the characteristic vapor bubble diameter would be significantly larger than the pore size.

There have been a number of investigations that have examined different methods of modifying the evaporator to overcome the decrease in the heat transfer caused by the vapor zone forming in the wick. For example, Figus et al (1996) proposed that the vapor zone could be reduced by including a small gap between the fin and the wick that would permit the vapor to escape. The vapor flow through the gap was modeled as a laminar Poiseuille flow. Their model predicted that a small gap of 10 μm between the heating fin and the saturated porous structure (fig. 2.6) would decrease the evaporator wall temperature. The heat transfer performance of a heated wick with a gap between the heating fin and the wick was also experimentally investigated by Platel et al (1996). They found that leaving a 100 μm gap between the fins and a porous structure with 20 μm pores prevented the vapor from being forced back into the wick. They also suggested that the gap size would depend on the porous structure. In particular, it should be larger than the pore size to prevent vapor penetration in the wick. However, at large gap sizes the evaporator can be deprimed. For example, Dupont et al (2003) found that the superheat of the evaporator wall required to initiate boiling was strongly dependent on the wick fit. For a tight fit with no gap, the superheat was typically 2-5°C, but when the gap was 1400 μm the superheat was 7.5°C to 16°C. This was associated with a sharp change in the differential pressure.

Platel et al (1996) also proposed that the build up of the vapor zone in the wick could be reduced by machining microgrooves on the heating interface of the fins. They

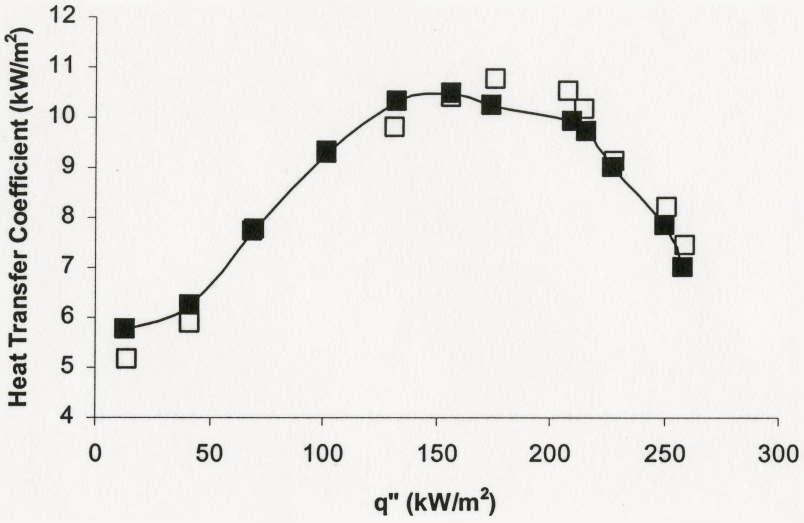

Figure 2.5. Variation of the heat transfer coefficient with heat flux during evaporation from a saturated porous structure obtained by Zhao et al (2000a), ■ Theoretical predictions, □ Experimental results.

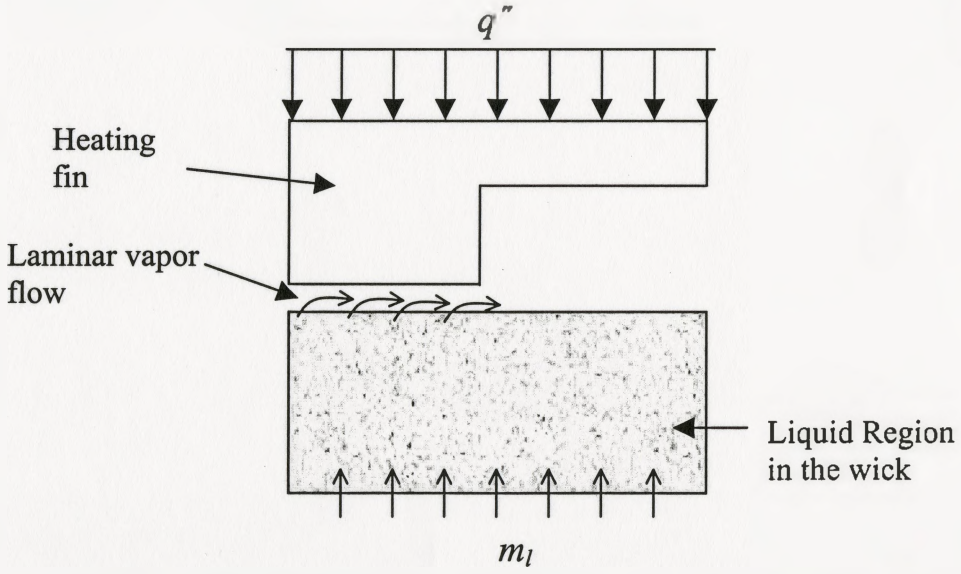

Figure 2.6. Gap between the heating fin and the saturated wick proposed by Figus et al(1996).

observed that the heat transfer coefficient for the fins with microgrooves increased by a factor of up to three as compared with smooth fins and argued the grooved fins allowed the vapor to migrate to the channels without being trapped in the wick which increased the maximum heat transfer coefficient.

2.2. Review of boiling in a confined space

The previous investigations on the capillary evaporator have shown that one method of overcoming the formation of the vapor zone in the wick was to leave a gap between the heating fin and the porous structure. The heat transfer mechanisms in this case, however, have not been investigated. The geometry suggests that it could be similar to boiling in a confined space. The investigations of the nucleate boiling in confined gaps have found that the heat transfer in this case was larger than that in conventional pool boiling (eg. Ishibashi et al 1969, Katto et al 1977, Yao et al 1983). They attributed this to the microlayer evaporation mechanism, where the applied heat is conducted through a thin liquid layer that forms between the heating surface and the coalesced vapor bubbles in the confined gap.

Ishibashi et al (1969) visually observed the thin liquid film on the heating surface occupied by a vapor bubble during boiling of water in a confined annulus space at a heat flux of 9.2 kW/m^2. A series of photographs (fig.2.7) taken at different times showed that the thin liquid film can cover the whole area between the vapor bubble and the heating surface, or can be partially dried out. Katto et al (1977) later visualized the boiling mechanism in an upward facing confined boiling geometry and observed the presence of

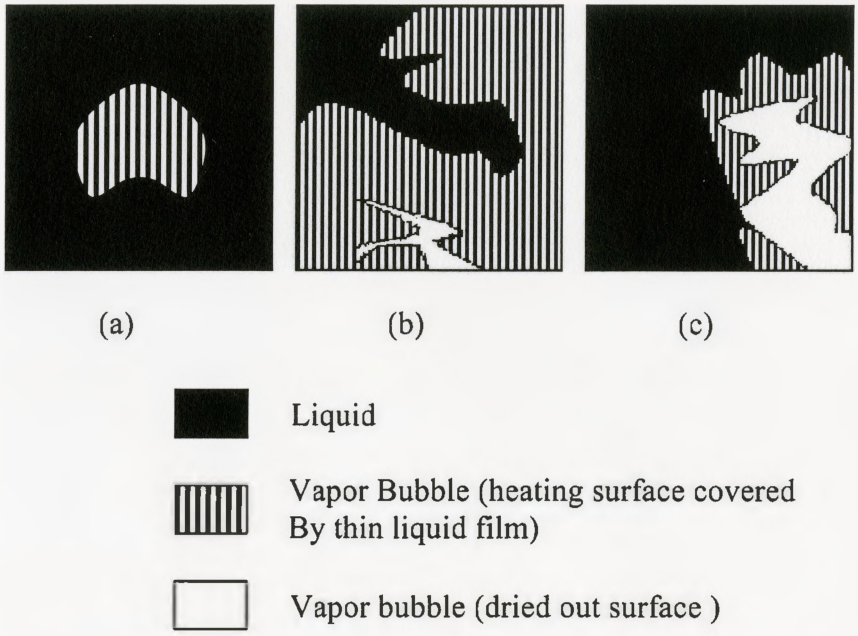

Figure 2.7. Schematics of the thin liquid film on the heating surface during boiling of water in a confined gap of 0.97mm obtained by Ishibashi et al(1969).

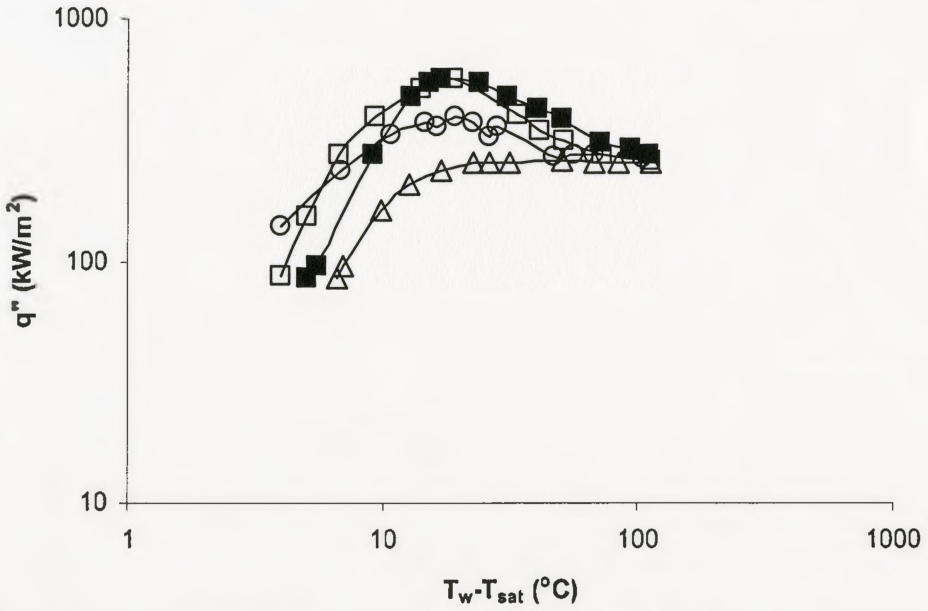

Figure 2.8. Effect of the gap size S on an upward facing confined boiling obtained by Katto et al (1977). Δ S=0.1mm, ○ S=0.2mm, □ S= 0.5mm, ■ S=1.0mm.

a static thin liquid layer between the vapor bubbles and the heating surface. They observed that the heat transfer performance for gaps of 200 μm and 500 μm (fig. 2.8) was significantly better than the performance for a gap of 1000 μm. They attributed this difference to the evaporation through the thin liquid layer. The poor performance observed at 100 μm was attributed to the formation of a large dry region on the heating surface.

Yao et al (1983) attempted to develop a map to predict the boiling regimes present in confined boiling. They performed boiling experiments in a vertical confined annulus space of 0.32mm, 0.80mm and 2.58mm for Freon-113, acetone and water. They observed that the boiling phenomenon changed with the size of the gap and the heat flux as shown in figure 2.9. For the small gap sizes, 0.32mm and 0.80mm, and heat fluxes, the boiling curve was a straight vertical line and the superheat was 0.6 K (fig.2.10). In this case, a thin liquid layer was maintained between the vapor bubbles and the heating surface. At higher heat fluxes, the vapor bubbles coalesced and temporary reversible dry regions appeared on the heating surface due to the temporary dry out that had occurred under the expanding bubbles. When the heat flux approached the dry out limit, the liquid film on the heated surface evaporated extensively and a dry region formed on the heating surface. In this case, the outgoing vapor flow from the gap was sufficient to prevent the liquid from getting into the crevice and rewetting the heating surface. For a large gap size (2.8mm) and high heat fluxes, nucleation occurred on the heated surface and the bubbles were slightly deformed. This regime can be considered as a transition from confined boiling to conventional pool boiling. Yao et al (1983) proposed that the boundaries

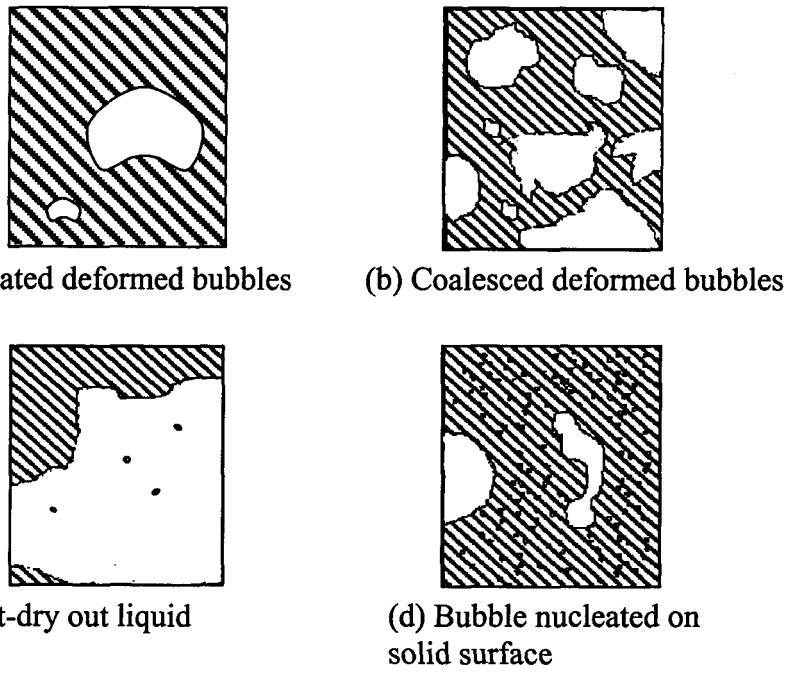

Figure 2.9. Boiling phenomena in confined gaps as described by Yao et al(1983).

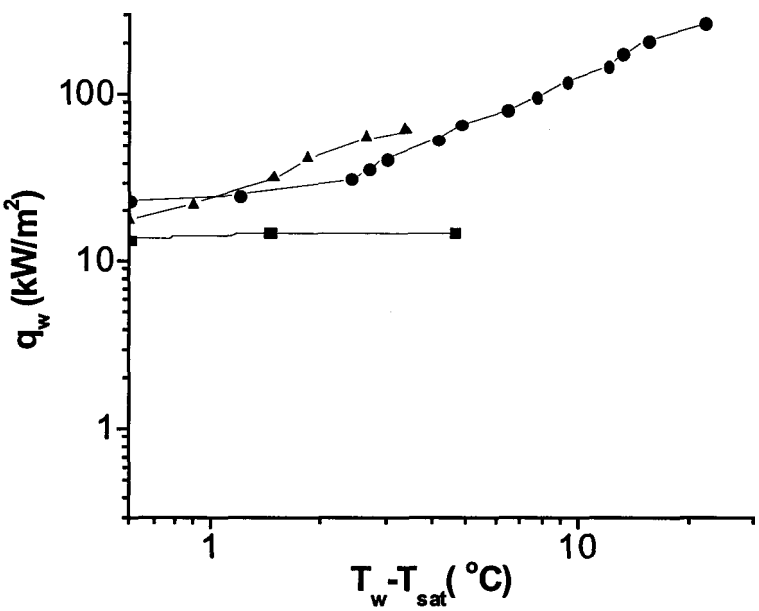

Figure 2.10. Boiling curve for water at atmospheric pressure in a confined annulus obtained by Yao et al(1983). For gap sizes of: ▲ S=0.32mm, ■ S=0.80mm • S=2.58mm.

between the different boiling regimes could be defined in terms of the boiling number defined by

$$B_l = \left(\frac{q_w L}{h_{fg} \rho_g S v} \right), \tag{2.2}$$

and the Bond number defined by

$$Bo = \frac{S}{\left[\sigma / g(\rho_l - \rho_g) \right]^{\frac{1}{2}}}, \tag{2.3}$$

The boiling number here represents the ratio of the characteristic time of the bubble rise through the gap and the characteristic time of the bubble expansion in the gap given by $\left(\frac{q_w}{\rho_g h_{fg} S} \right)^{-1}$. The Bond number represents the ratio of the gap size to the nominal bubble diameter. The resulting boiling map is shown in figure 2.11.

A model for the heat flux in the coalesced bubble region conditions for a confined boiling between two parallel surfaces was proposed by Fujita et al (1988). They attributed the high heat transfer performance to the microlayer evaporation on the deformed bubbles and the total heat flux was given by

$$q = (1 - f) q_l + q_v, \tag{2.4}$$

where f is the void fraction, q_l is the sensible heat flux removed by the liquid given by

$$q_l = \frac{2 k_l \Delta T_{sat}}{\sqrt{\pi a_l t_l}}, \tag{2.5}$$

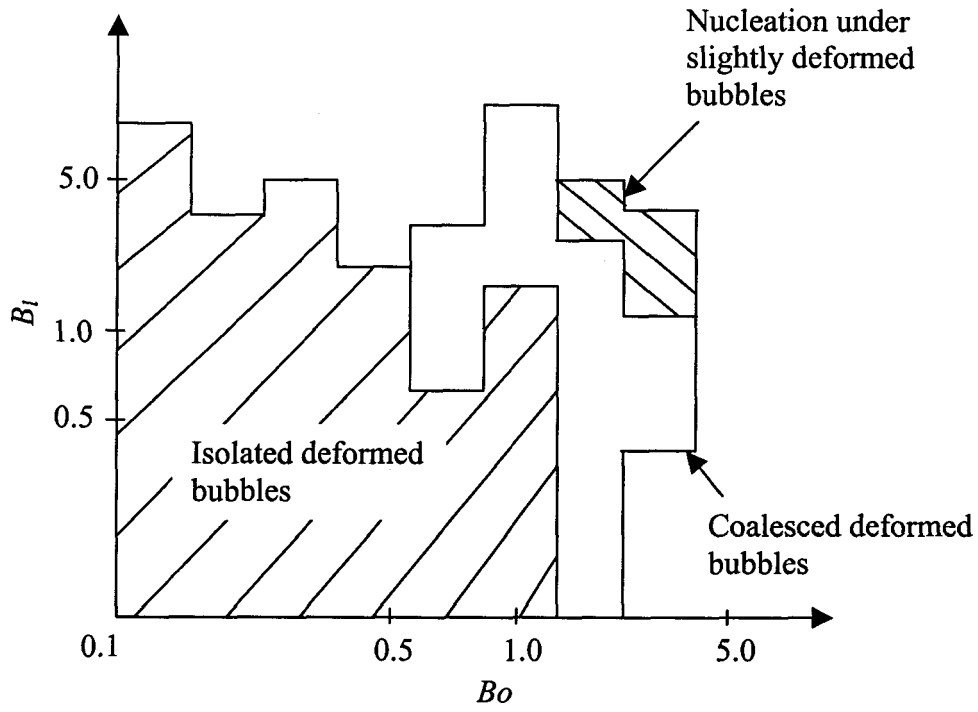

Figure 2.11. Boiling map generated by Yao et al (1983) defining the boundaries between different confined boiling regimes.

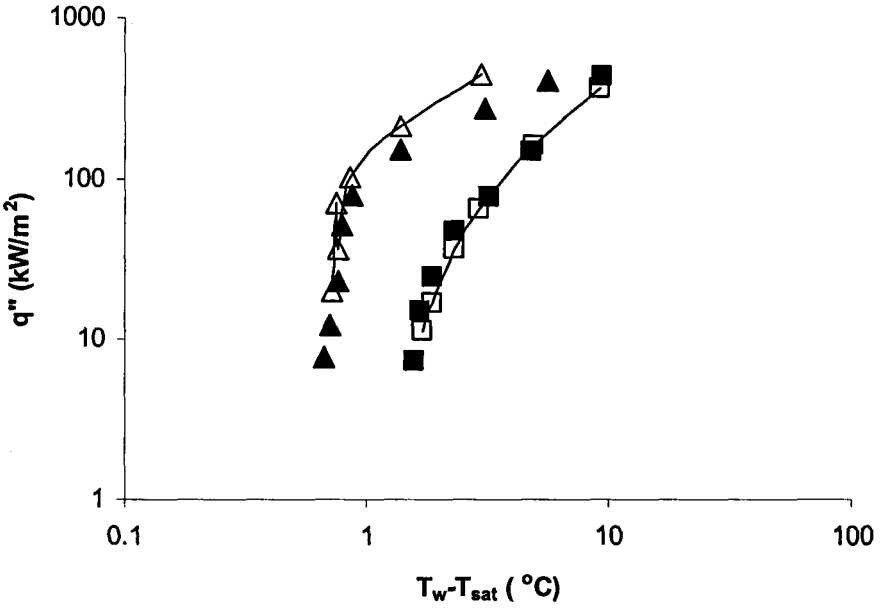

Figure 2.12. Experimental results obtained by Fujita et al(1988) for gap sizes of ▲ 0.6mm, ■ 2.0mm and predictions of the sensible and latent heat model for gap sizes of Δ 0.6mm, □ 2.0mm.

and q_v is the latent heat across the thin liquid film formed between the vapor bubble and the heated surface given by

$$q_v = \frac{k_l}{\delta_l} \Delta T_{sat}. \tag{2.6}$$

The results showed that the model over predicted the total heat flux at small gap sizes (figure 2.12). This was attributed to the formation of reversible dry regions on the heating surface observed in the experiment.

A mechanism for the liquid flow in the evaporative microlayer was proposed by Lee et al (1992), who performed a study on confined boiling on an upward facing surface, where a thin liquid layer separates the vapor bubble from the heating surface. They suggested that the liquid flow from the bulk fluid to the evaporative microlayer was driven by the capillary pressure created from the curvature at the liquid vapor interface as shown in figure 2.13.

Passos et al (2004) observed that the heat transfer characteristics in confined pool boiling from a downward facing heating surface were similar to the mechanisms for an upward facing heating surface. In this case, they investigated the confined boiling for FC 72 and FC 87. They observed that the optimal heat transfer performance at low heat fluxes was obtained for a gap size of 500 μm. The visualizations of the subcooled boiling at different gap sizes and heat fluxes revealed that the increase in heat flux was accompanied by an increase in the vapor bubble density at all gap sizes. For small gap sizes between 200 microns and 500 microns, isolated deformed bubbles and coalesced deformed bubbles coexist and covered a large area of the heater surface. This increased

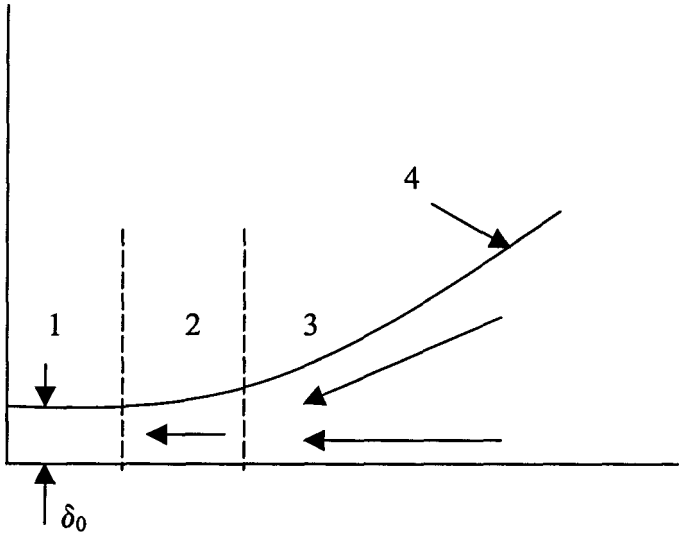

Figure 2.13. Schematic of the liquid flow to the microlayer region driven by the capillary pressure proposed by Lee et al (1992). 1. Dry region 2. Interline evaporating region 3. Bulk layer region 4. Liquid vapor interface. δ_0. Equilibrium film thickness.

the area of the liquid film evaporation and enhanced the heat transfer performance. For larger gap sizes of 1mm and 13mm, relatively small isolated circular vapor bubbles nucleate on the heating surface. These observations can explain the higher heat transfer performance of the confined boiling at relatively small heat fluxes.

Chapter 3. Experimental Facility and Methodology

An experimental investigation was performed to study the heat transfer characteristics of a saturated porous structure partially heated at the upper boundary. The experiments were performed for alumina porous plates heated with a thin foil. The experimental facility used in this investigation is presented in the next section. The experimental methodology and the analysis of the experimental uncertainty are then presented.

3.1. Experimental facility

A schematic of the test facility used in this investigation is presented in figure 3.1. The facility consists of a main test section with a heating foil and a porous media, a constant head tank that supplies preheated water to the test facility, a pump and a secondary tank. The water level in the main test facility was maintained using the constant head tank on an adjustable platform. The level of the liquid in the constant head tank was maintained by pumping fluid into the constant head tank and having the excess fluid above an overflow height return to the secondary tank. The water in the constant head tank was preheated using a 1 kW plug heater. The temperature in this tank was

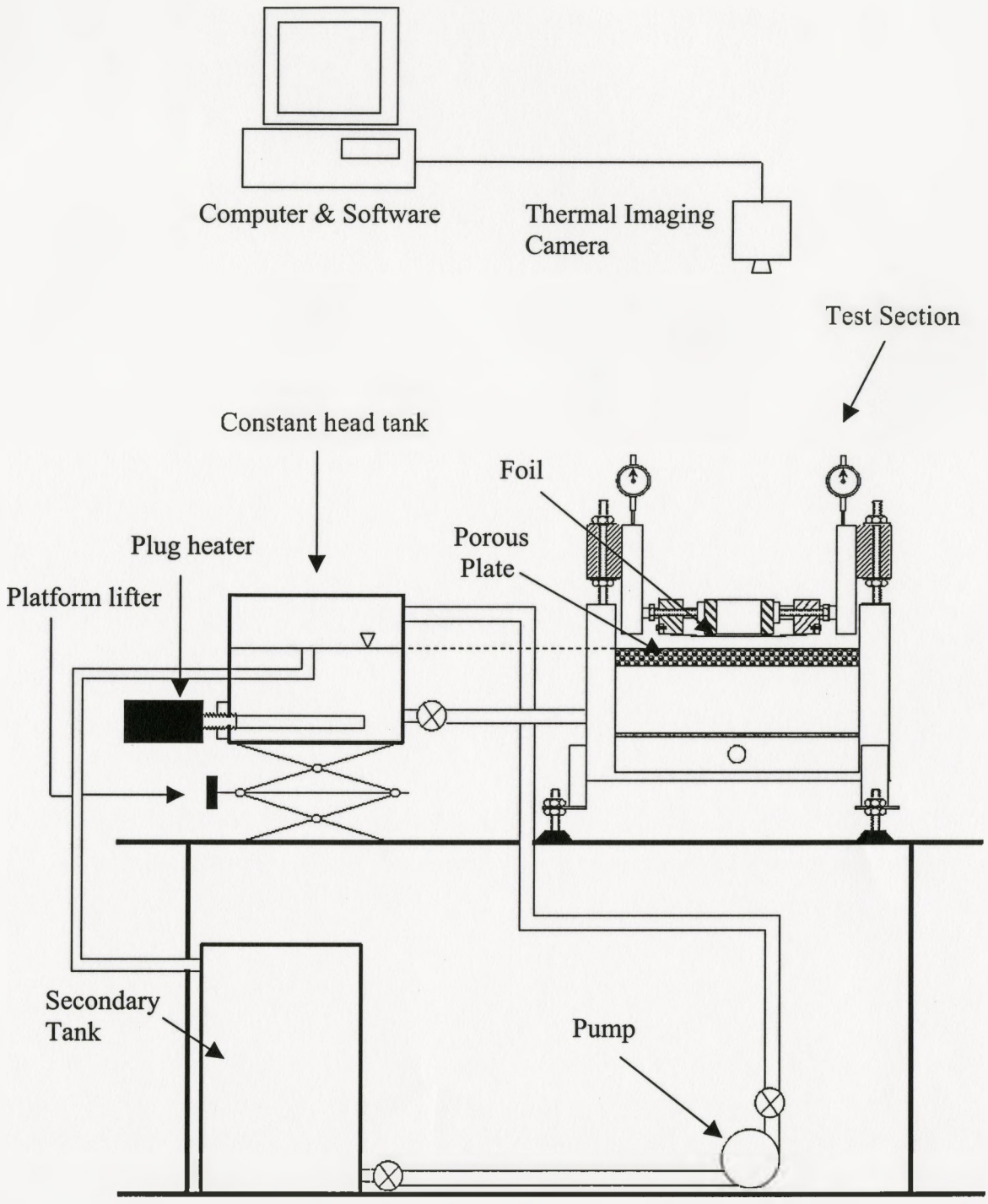

Figure 3.1. Schematic of the experimental facility.

measured using a T type thermocouple that provided input to a PID temperature controller for the heaters. The sides of the constant head tank were insulated with a fiber glass insulation to reduce the heat losses by natural convection.

A schematic of the main test section with the heater assembly and the porous structure is shown in figure 3.2. The experiments were performed for porous alumina plates (Al_2O_3) that were 19 mm thick and 118 mm by 255 mm with a porosity Φ of 50 % and nominal pore sizes of 50 μm and 200 μm. The alumina has a thermal conductivity of 27.6 W/m.K. The porous plate was placed in a 310 mm by 145 mm by 179 mm container of water. The plate was supported on two stainless steel bars fixed to the side walls of the container at a height of 137 mm from the bottom surface. The temperature of the water was controlled using two 100 Watt plug heaters that were threaded into the side walls of the tank. A copper screen mesh clamped between two perforated stainless steel plates was positioned 80 mm below the porous plate to reduce the spanwise temperature variations in the water. The temperature of the water was measured using thermocouples positioned 6.5 mm, 26.5 mm, and 46.5 mm below the porous structure. The top of the porous plate was electrically heated using a 25 μm thick stainless steel resistive foil that was 35 mm wide and 170 mm long. The foil was clamped at each end to copper electrodes using two #8 stainless steel screws. The electrodes were designed to slide along two 12.7 mm diameter rods on glass filled Teflon bearings that electrically isolated the electrodes from the rods. The foil was stretched using two stainless steel screws threaded into the copper electrodes that butted against a Teflon block as shown on figure 3.4 (a). A nylon

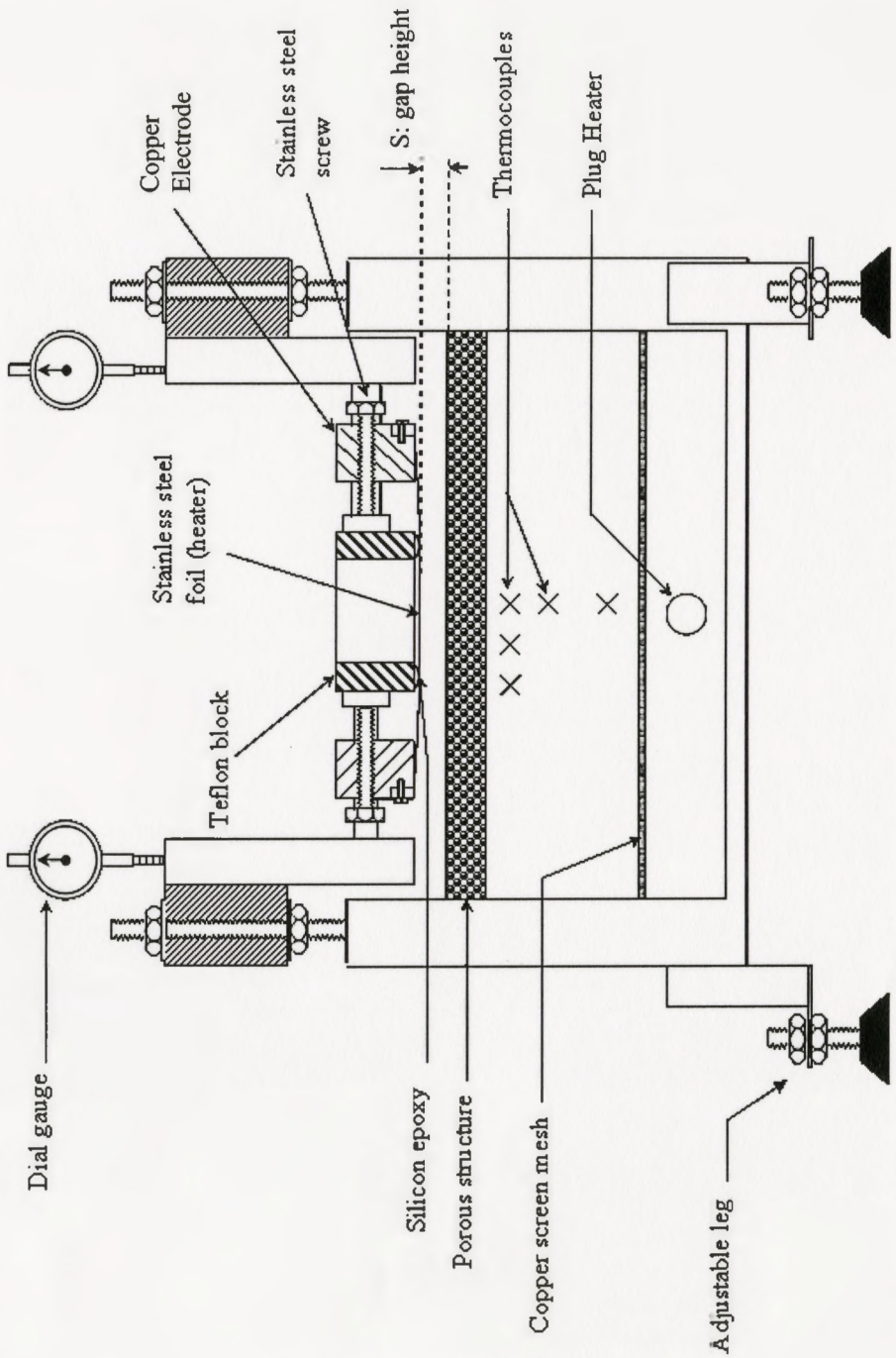

Figure 3.2. Schematic of the test section.

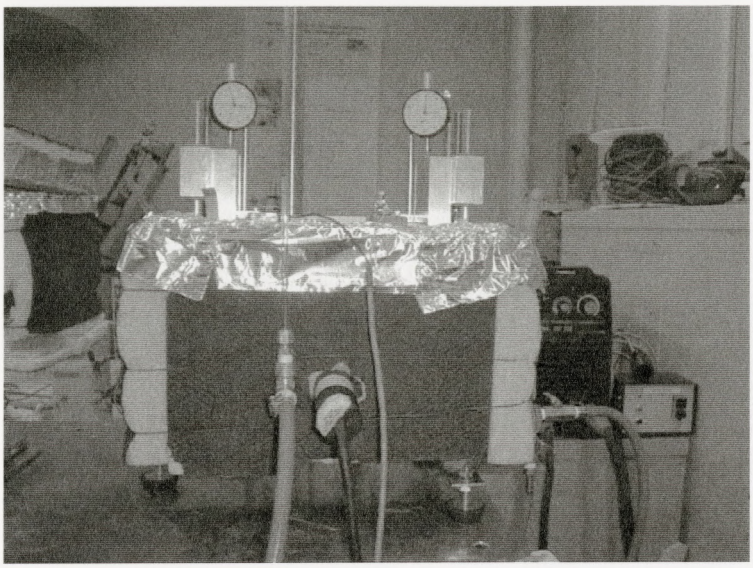

(a)

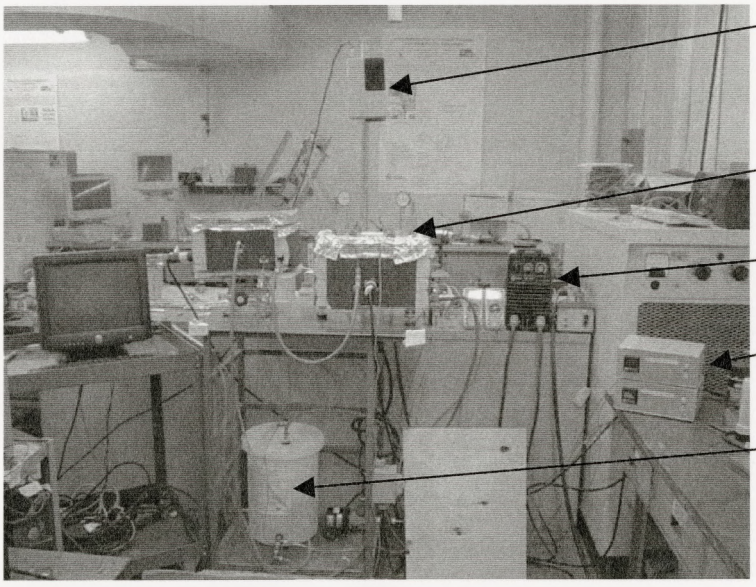

(b)

Figure 3.3. Photographs of (a) the main test section, (b) the experimental facility.

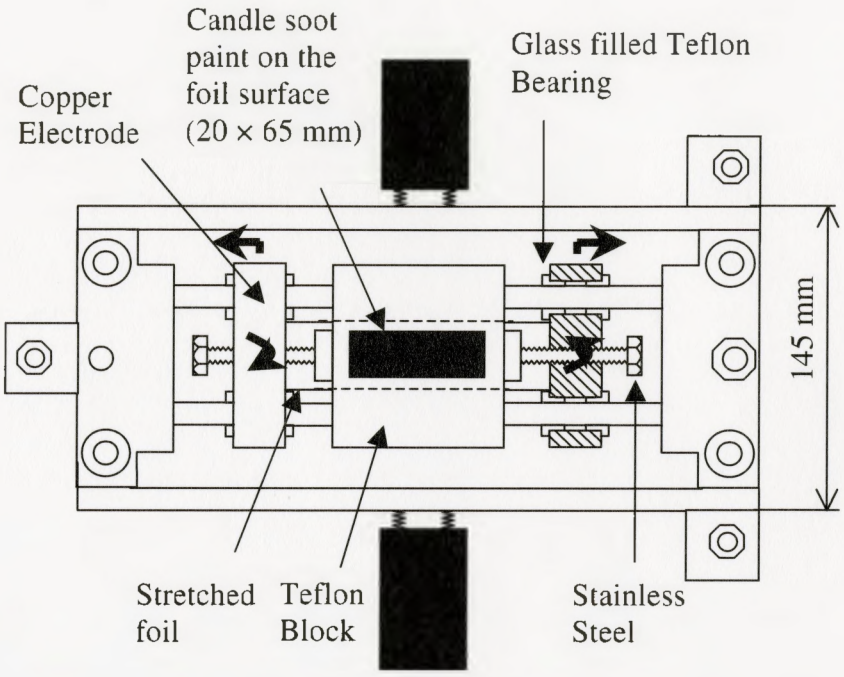

(a)

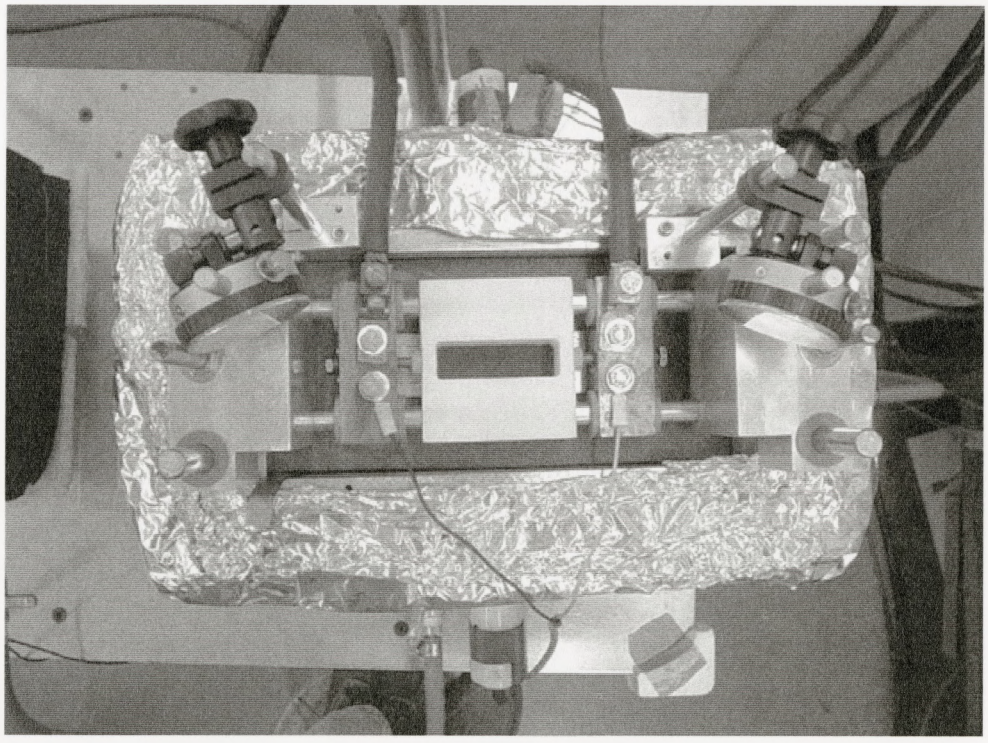

(b)

Figure 3.4. Top view of the test section (a) schematic and (b) photograph.

cylindrical disk was fixed at the end of each screw to prevent the Teflon from being worn.

The foil was heated using a Miller 250 ST DC power supply that could supply a maximum current of 200A at 100% duty cycle. The power supply was connected to the electrodes by two heavy gauge (0/1) copper wires. The current through the foil was determined by measuring the voltage drop across a 50mV-200A shunt. The voltage drop across the electrodes was measured using a Fluke 175 multimeter.

The entire heating assembly was mounted on two 90 mm by 50 mm aluminum blocks. Both blocks slide vertically on two 12.5 mm rods that allowed the whole heating assembly to move vertically relative to the porous structure. The aluminum blocks were set at the desired height using two nuts on a 9.5 mm diameter threaded rod (fig 3.2) located between the vertical rods (fig 3.5). The distance between the heating foil and the porous media was measured at each end using a Mututoyo dial gauge with an accuracy of ±12 μm. These dial gauges were mounted on the container surface and positioned at the top of the aluminum moving blocks as shown in figure 3.2.

The Teflon block had a 65 mm by 20 mm opening that allowed the upper surface of the stretched stainless steel foil to be viewed from above. A FLIR 3000 SC high speed thermal imaging camera, with a resolution of 0.5 mm/pixel, was used to measure the temperature distribution on the upper surface of the thin stainless steel foil heater at a frequency of 60 Hz. The time constant of the foil heater, for which the temperature of the foil upper surface reaches 63.2 % of the bottom surface temperature, is given by

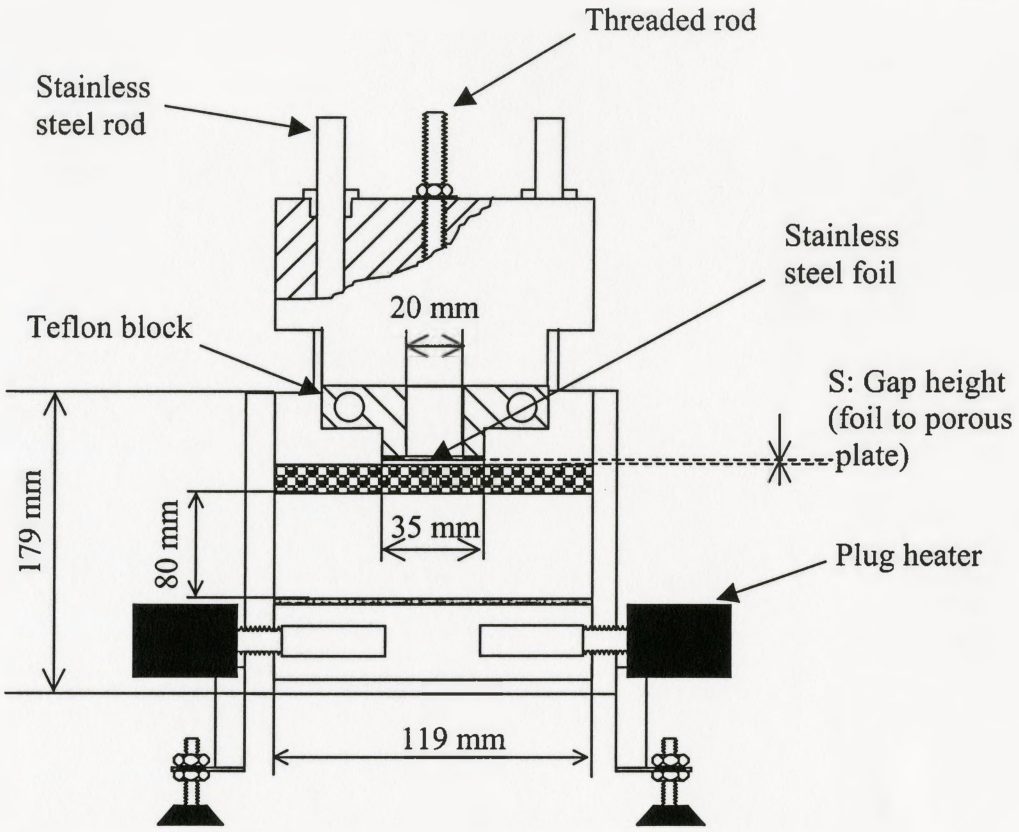

Figure 3.5. Cross sectional view of the main test section.

$$\tau \approx \frac{\rho C_p}{k}\delta^2, \tag{3.1}$$

where δ, ρ, C_p , k are the thickness, the density, the specific heat and the conductivity of the foil. It was found that the time constant of the foil is 0.16 ms which is much smaller than the time scale of the thermal image recordings (17.00 ms). Therefore the temperature measured by the thermal imaging camera on the top of the foil can be considered to be equivalent to the temperature of the bottom surface of the foil.

The upper surface of the foil was painted with a thin layer of a candle soot black paint to ensure it had a uniform emissivity near 1. Gao (2000) reported that the emissivity of a similar foil with the candle soot paint was 0.96 ± 0.01. The distance between the lens and the foil surface was 0.4 m. The ratio of foil area to surrounding area is small so it is reasonable to assume that the ambient emissivity is 1.

3.2. Experimental procedure

In each experiment, the porous plate in the test section was initially leveled by changing the position of the nuts on the adjustable legs welded to the main test section. The level was checked using a level gauge on the test section surface. The distilled water in the constant head tank was then boiled for approximately 10 min before each experiment to degas the water. This procedure was repeated until the test section was filled with preheated water. The two 100 Watt heaters in the test section were then switched on and the PID controller was set to the desired temperature of the subcooled liquid T_b. The pump was switched on to supply water to the constant head tank and

maintain a constant level of water at the test section. The level of water was then adjusted to a level above the porous plate and a heat flux q″ of 11.7 kW/m^2 was applied on the heater to check for the presence of any initial air bubbles. Once it was established that there were no air bubbles trapped under the heater surface, the heater was then lowered until it was in contact with the porous structure. Contact was determined by pushing at each side of the heating assembly on the porous structure until there was no change observed in the dial gauge indicators. The positions of the dial gauges were then zeroed. The level of water was adjusted to the level of the porous plate surface using a sight glass indicator and by shining a flash light on the upper surface of the porous plate. The level was then determined by lowering the water level on the porous structure, until the solid phase of the porous plate could be distinguished. A moderate heat flux (~20.0 kW/m^2) was applied for about two hours to degas the interfacial region between heating foil and the porous structure before measurements were taken.

For each porous media, measurements were performed for gaps ranging from 0 μm to 1000 μm. At each gap height, the power applied was varied from 11.7 kW/m^2 to a heat flux where hot spots were observed over the heating surface. At each heat flux, the system was allowed to reach steady state which required approximately 20 minutes. The surface temperature distribution was then measured at a sampling frequency of 60 Hz for a period of 20 seconds using the thermal camera. The instantaneous probability density function of the temperature distribution over the foil surface was determined for 100 frames. An averaged pdf distribution was then determined and the mean temperature $\overline{T}_{ave}$ associated to the time averaged pdf temperature distribution was computed.

3.3. Evaluation of the energy balance

The electrical power added to the foil heater is generated as heat by Joule heating. This heat is transferred to the water and the saturated porous structure below the foil and partly lost at the upper surface by radiation and natural convection to the ambient, it was also transferred by lateral conduction through the foil. Thus the heat flux to the water and the saturated porous plate can be estimated by

$$q_{boil} = q_{elec} - q_{rad} - q_{nat\,conv} - q_{cond}, \tag{3.2}$$

where q_{elec} is the electrical power provided to the foil. The radiation to the ambient was estimated by assuming the foil was a gray body exchanging energy with the ambient surface at T_∞. Thus, the heat losses by radiation from the foil surface were estimated by

$$q_{rad} = \varepsilon_u \sigma \left(T_w^4 - T_\infty^4\right), \tag{3.3}$$

where ε_u the emissivity of the upper surface was 0.96. The temperature of the heating foil T_w was near 100°C in most cases, while the ambient temperature was 25°C . In these cases the total heat loss by radiation was 0.6 kW/m^2.

The heat transfer by natural convection to the ambient was estimated from

$$q_{nat\,conv} = \bar{h}_{nat\,conv}\left(T_w - T_\infty\right), \tag{3.4}$$

where $\bar{h}_{natconv}$ is the natural convection heat transfer coefficient. This heat transfer coefficient was estimated using the McAdams correlation (Incropera et al 1990) given by

$$\bar{h}_{natconv} = 0.54\frac{k}{L}Ra_L^{1/4} \tag{3.5}$$

The fluid proprieties in this correlation were evaluated at the film temperature $\left(\frac{T_w + T_\infty}{2}\right)$. It was found that the natural convection heat transfer coefficient $\bar{h}_{natconv}$ was approximately 13.3 W/m^2.K and the resulting natural convection heat flux would be 1.0 kW/m^2 when the average foil temperature was at 100°C.

The maximum lateral conduction heat flux can be estimated by considering the case where a permanent high temperature region with a maximum temperature of 300°C formed over the foil surface, the temperature gradient obtained for this case was 36 363 ± 1655 K/m. This would correspond to a heat of flux 2.5 W, which represents 1 % of the electrical power that was applied. Therefore, the lateral conduction through the foil is neglected in this study.

In the case where high temperature regions form over the heating surface, the temperature distribution over the foil would vary from 100°C up to a maximum of 300°C. which would vary the distribution of the heat losses by radiation over the heating surface from 0.6 kW/m^2 to 5.4 kW/m^2 and the heat losses by natural convection from 1.0 kW/m^2 to 3.7 kW/m^2 . Therefore, the total heat losses on the heating surface would vary from 1.6 kW/m^2 up to a maximum of 9.1 kW/m^2 which makes the assumption of uniform heat flux boundary condition no longer valid in these cases.

In this work, the estimated net heat flux was assumed to be uniform and accounted for the heat losses by natural convection and radiation for an average foil surface at 100°C for all the cases. Thus, the heat flux to the saturated porous structure

was computed by subtracting the heat fluxes by radiation and natural convection from the electrical power applied. The heat flux to the saturated porous structure was given by

$$q_{boil} = \frac{IV}{A} - \varepsilon_u \sigma\left(T_w^4 - T_\infty^4\right) - \bar{h}\left(T_w - T_\infty\right) \tag{3.6}$$

3.4. Error analysis

The uncertainty in the reported measurements were estimated using the method given by Kline and McClintock (1953). Therefore, the uncertainty of the heat flux to the saturated porous structure is given by

$$u_{q''_{boil}} = \sqrt{\sum\left(\frac{\partial q''_{boil}}{\partial x_i} u_i\right)^2}, \tag{3.7}$$

where x_i are the independant variables, and u_i the uncertainty associated with each variable x_i. The error associated with each variable in equation (3.6) is shown in table 3.1. the resulting uncertainty of the heat flux to the saturated porous structure was found to be

$$\frac{u_{q''_{boil}}}{q''_{boil}} = \frac{\sqrt{\sum\left(\frac{\partial q_{boil}}{\partial x_i} u_i\right)^2}}{q''_{boil}} \approx 3.2\%. \tag{3.8}$$

The error of the average foil temperature is caused by the error due to the accuracy of the thermal camera (0.20°C), to the uncertainty of the surface emissivity (0.64°C), and to the estimation of the average foil temperature over 100 frames. The error associated with the estimation of the averaged temperature over 100 frames is determined using the method

given by Bendat and Piersol (1980). In this approach the estimation error of the real average temperature $\overline{T}_{real}$ using the mean temperature over N data points is given by

$$\varepsilon_T = \left|\overline{T}_{estimated} - \overline{T}_{real}\right| = \frac{1}{\sqrt{N}}\sigma_T, \tag{3.9}$$

where σ_T is the standard deviation of the temperature measurements over N frames. The corresponding standard deviation σ_{Tmin} of the temperature is 10.51°C for the case where the fluctuating hot spots appeared on the foil, eg, for 51.7 kW/m^2 at a gap height of 600 μm. The uncertainty in the temperature for this case over 100 frames is 1.04°C.

The uncertainty associated with the gap height measurements ΔS was assumed to be due to the error of the dial gauges (±12 μm).

	x_i	u_i	$\left\|\frac{\partial q''}{\partial x_i}u_i\right\|$ (W/m^2)
ε	0.96	0.01	651.2
T_w (°C)	100.0	1.8	46.2
T_∞(°C)	25.0	0.5	9.5
Current (A) I	47.2	0.40	510.5
Voltage (V) V	6.7	0.01	89.9
Foil Area (m^2) A	0.00525	0.00015	1721.0

Table 3.1. List of variables and uncertainties for the applied heat flux.

CHAPTER 4. Experimental Results and Discussion

The objective of this investigation was to examine the effect of the gap height on boiling heat transfer in a confined space between a heated surface and a saturated porous structure. The experiments were initially performed for a porous plate with a nominal pore size of 50 μm and a subcooled liquid temperature of 60°C. The effect of the subcooled liquid temperature and the pore size on the boiling in the confined gap was then investigated by performing experiments at subcooled temperatures of 75°C and 90°C and with a porous plate of 200 μm pore size.

4.1. Effect of the gap height on the confined boiling.

Experiments were initially performed for a 50 μm porous plate and a subcooled liquid temperature of 60°C. The distribution of the time averaged temperature on the foil for heat fluxes of 11.7 kW/m^2, 18.4 kW/m^2 and 25.1 kW/m^2 when the foil was in contact with the porous plate are shown in figure 4.1. For the heat flux of 11.7 kW/m^2, the time averaged temperature over the entire foil surface was near the saturation temperature of water. However, when the heat flux was increased to 18.4 kW/m^2, there was a high temperature region on the foil surface with a maximum of 155°C. The temperature and

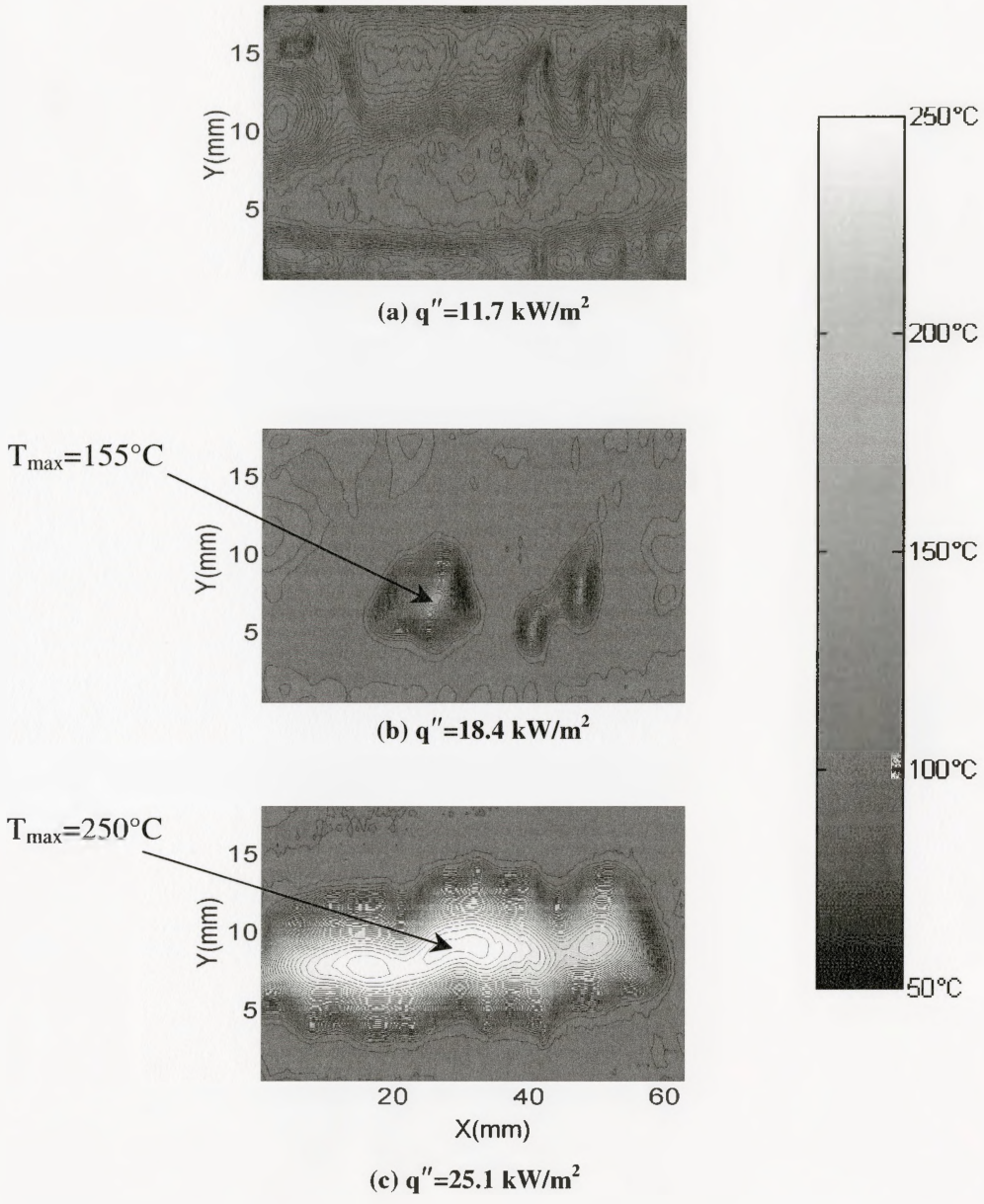

Figure 4.1. Distribution of the time averaged temperature on the foil for (a) q″=11.7 kW/m^2, (b) q″=28.4 kW/m^2 and (c) q″=25.1 kW/m^2.

the extent of the high temperature region increased when the heat flux was increased further to 25.1 kW/m^2. In this case, the maximum temperature in the region increased to 250°C.

Typical time sequences of the instantaneous temperature distribution on the heating surface when the foil was in contact with the porous plate for heat fluxes of 11.7 kW/m^2 and 18.4 kW/m^2 are shown in figure 4.2 and figure 4.3. The scale in these figures is 98°C to 104°C. It is clear that when the heat flux was 11.7 kW/m^2, there are two different types of regions present over much of the foil. There are regions where the temperature is between 100°C and 104°C that are superheated, and regions where the temperature is between 99°C and 100°C suggesting that the temperature is at the saturation temperature of water. During the period shown in figure 4.2, the saturated region expanded on the surface and covered the entire heating foil at t = 0.066 s, and later at t = 0.133 s it shrank back to its initial size. Thus, the distribution of the two regions is changing with time due to the expansion and shrinking of the saturated regions over the foil surface. When the heat flux was increased to 18.4 kW/m^2, the distribution of the saturated and superheated regions are still time dependent. In this case, the saturated region covered most of the heating surface at all sequences. There were also high temperature regions formed on the foil where the maximum temperature was 155°C.

The characterization of the surface temperature distribution can be extended to longer time series by computing the probability density function of the instantaneous temperature distributions over the foil surface for 100 frames. These distributions are averaged and the resulting time averaged probability density functions are shown in

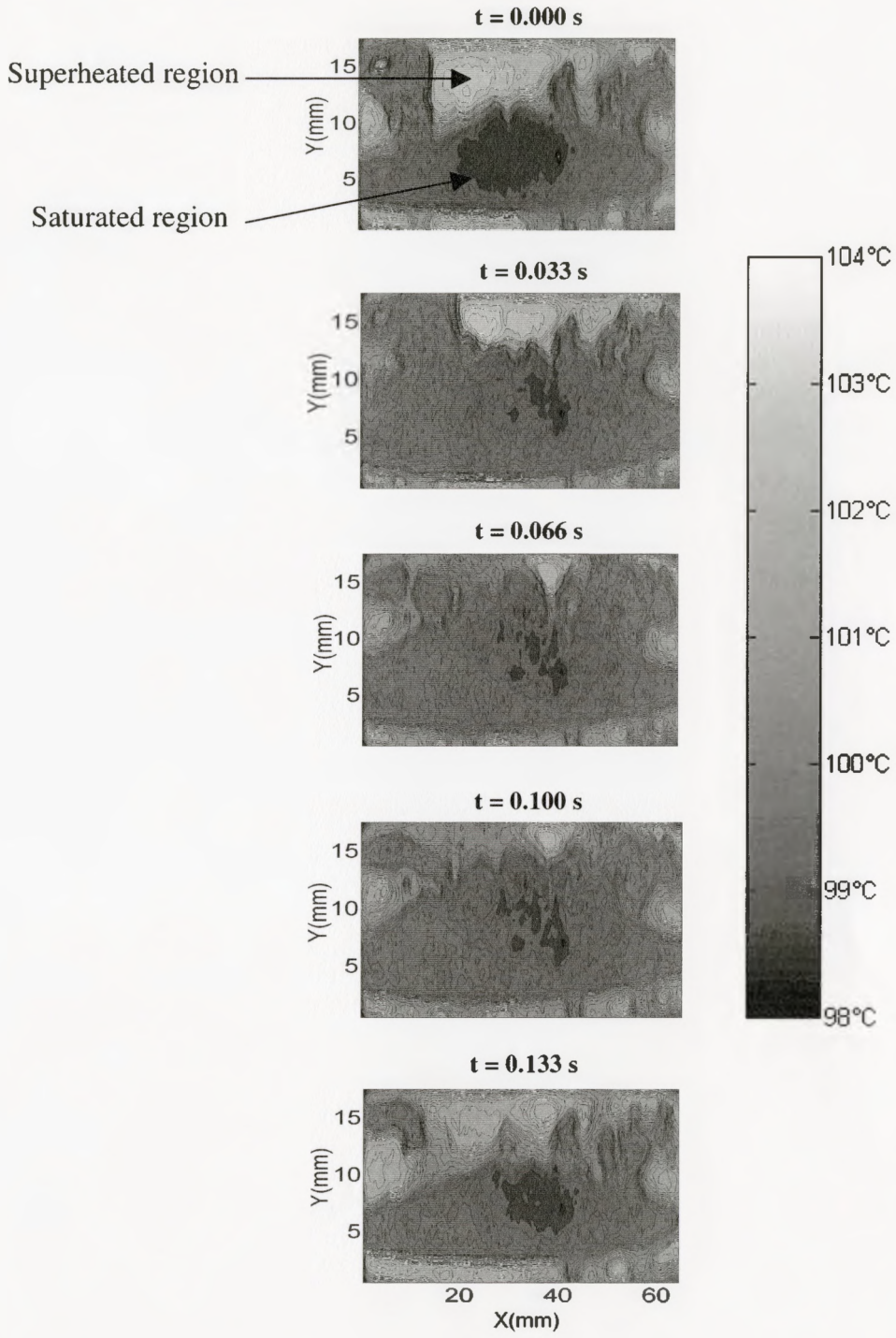

Figure 4.2. Distribution of the instantaneous temperature for a heat flux of 11.7 kW/m^2 when the foil was in contact with the porous plate.

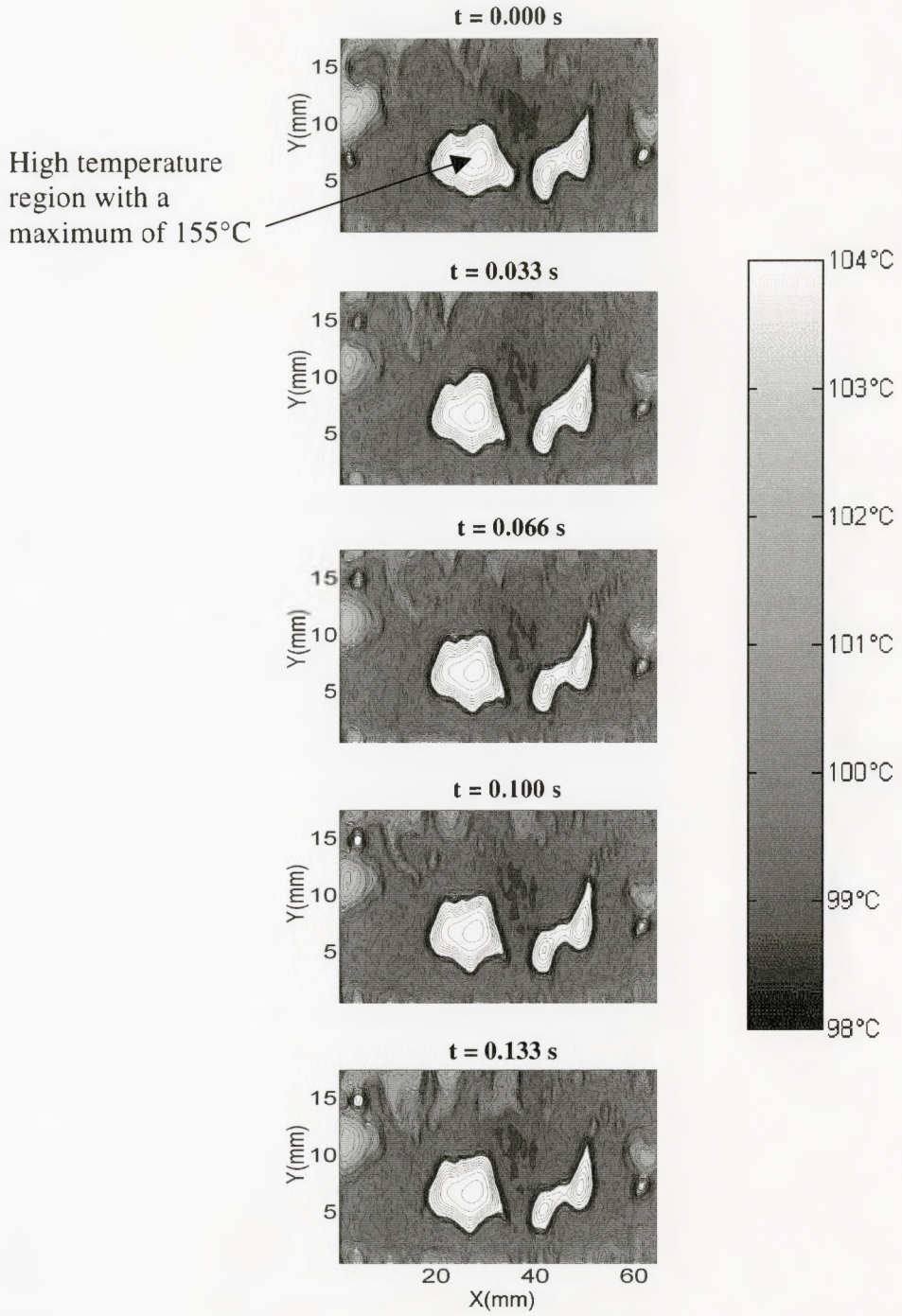

Figure 4.3. Distribution of the instantaneous temperature for a heat flux of 18.4 kW/m^2 when the foil was in contact with the porous plate.

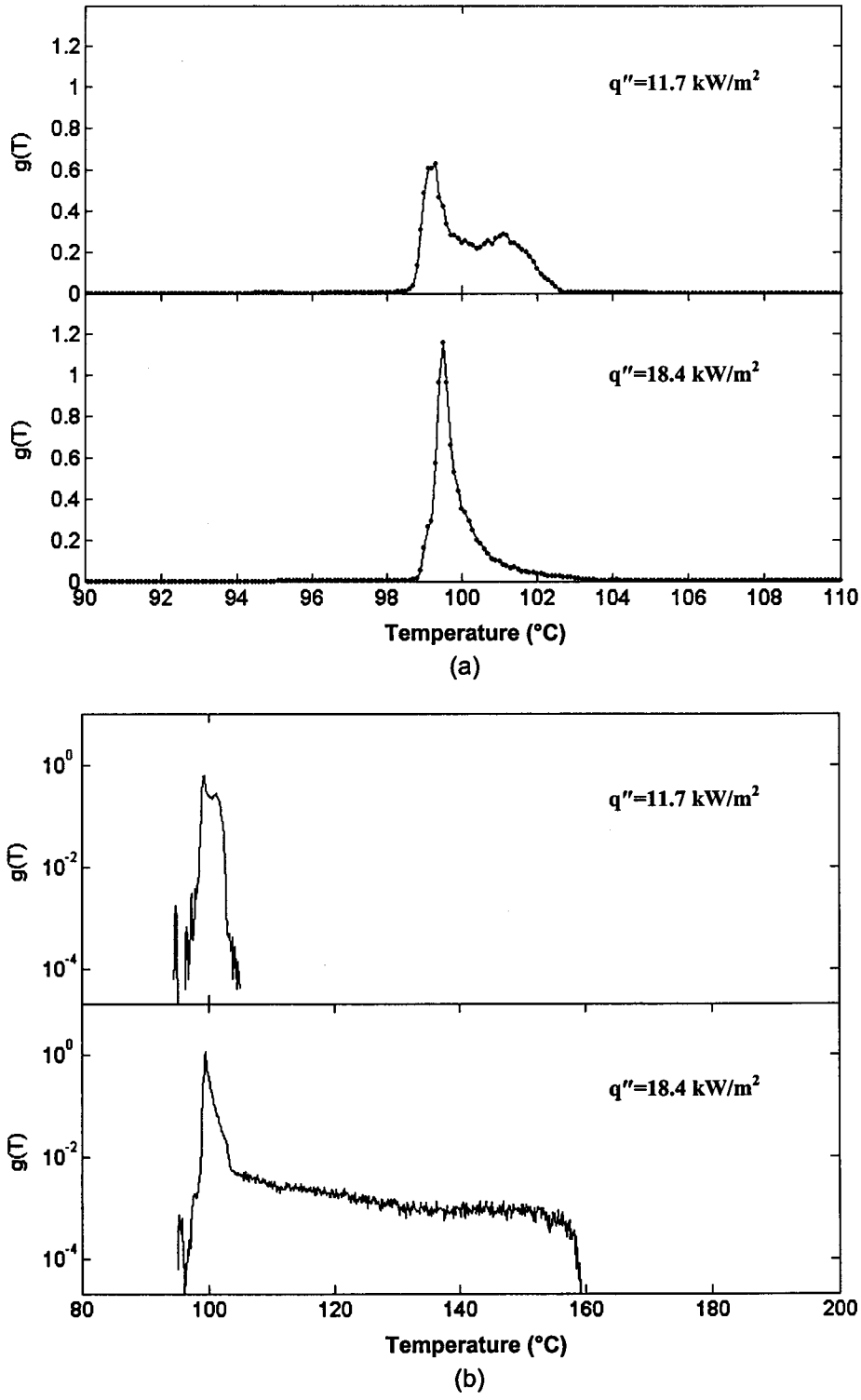

Figure 4.4. Probability density function of the temperature on the foil at zero gap height (a) on a linear scale and (b) on a logarithmic scale.

figure 4.4. For a heat flux of 11.7 kW/m^2, there is a broad peak between 99.2°C and 102.5°C because there are both superheated regions and cooler saturated regions on the foil. When the heat flux was increased to 18.4 kW/m^2 the distribution had a sharper peak at a temperature of 99.5°C and the distribution near the superheated region between 100°C and 103°C decreased, which is consistent with what was observed in figure 4.3. The formation of the high temperature regions on the foil at 18.4 kW/m^2 can be seen in figure 4.4.b where there is a clear tail extending to 159°C in the temperature distribution presented on a logarithmic scale.

The effect of the heat flux on the temperatures spatially averaged on the foil $\overline{T}_{ave}$ is shown in figure 4.5. It is clear that as the heat flux was increased from 11.7 kW/m^2 to 18.4 kW/m^2 the average temperature increased from 100°C to 102°C because of the formation of the high temperature region on the foil. When the heat flux was increased further to 25.1 kW/m^2 the mean temperature increased up to 145°C due to the expansion of the high temperature region on the heating surface. The heat transfer coefficient given by

$$\overline{h} = \frac{q''}{\left(\overline{T}_{ave} - T_b\right)}, \tag{4.1}$$

where q'' is the applied heat flux and T_b the temperature of the liquid below the porous plate, for this case is shown in figure 4.6. The average heat transfer coefficient increased when the heat flux was increased from 11.7 kW/m^2 to 18.4 kW/m^2 and then decreased at a heat flux of 25.1 kW/m^2.

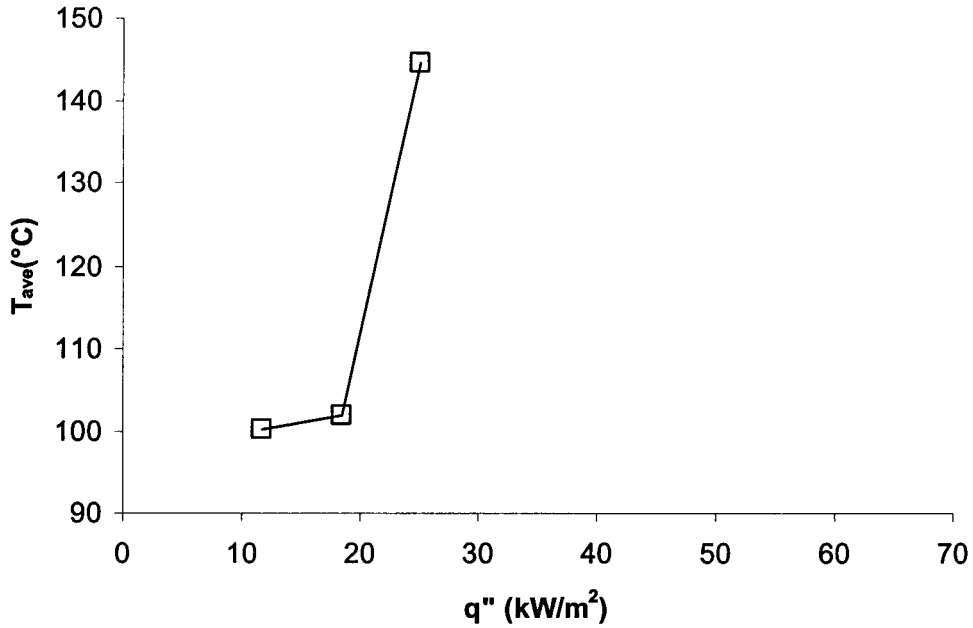

Figure 4.5. Change in the average foil temperature $\overline{T}_{ave}$ with heat flux for a zero gap height.

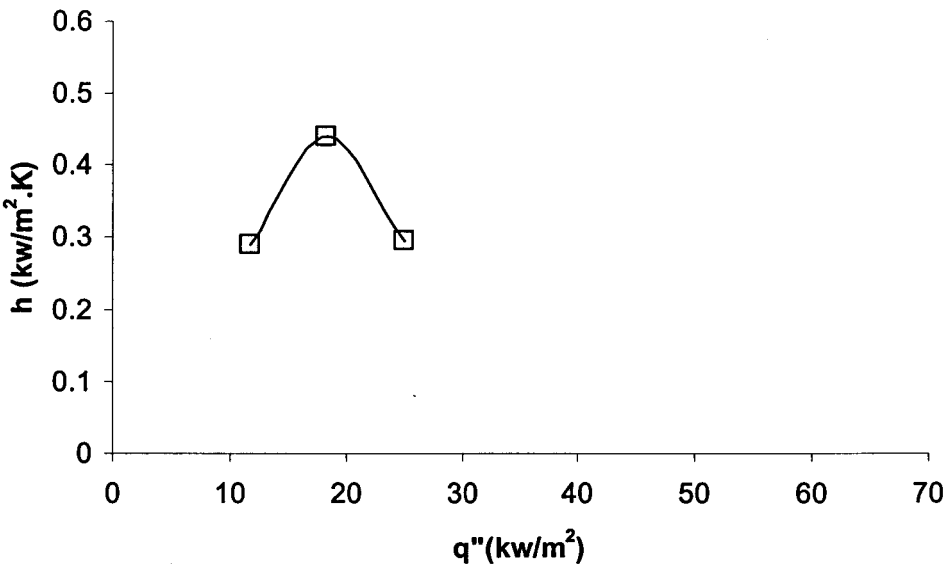

Figure 4.6. Change in the heat transfer coefficient $\overline{h}$ with heat flux for a zero gap height.

Experiments were then performed to examine how the heat transfer from the heated foil changed when the gap height between the heated foil and the porous plate was increased. Distributions of the time averaged temperature on the heating surface for typical gap heights of 300 μm and 600 μm are shown in figure 4.7 and figure 4.8. The heat flux for the 600 μm gap was increased to 58.3 kW/m^2, as compared to 38.4 kW/m^2 for the 300 μm gap and to 25.1 kW/m^2 for 0 μm gap. The results show that the distribution of the time averaged temperature on the foil for the gap of 300 μm was relatively uniform for heat fluxes up to 25.1 kW/m^2, but a high temperature region occurred in the time averaged foil temperature for heat fluxes of 31.7 kW/m^2 and above. When the gap height was 600 μm, the time averaged temperature of the foil was relatively uniform at 100°C for heat fluxes up to 38.4 kW/m^2, and there were only modest regimes of elevated mean temperatures for heat fluxes up to 58.3 kW/m^2. Thus, the gap height had a significant effect on the heat transfer produced by the foil over the porous media.

The measurements were also performed for a range of other gap heights between 100 μm and 1000 μm. The results from these cases can initially be compared by examining the change in the spatially and temporally averaged temperature on the foil shown in figure 4.9. It is clear that in all cases the average temperature $\overline{T}_{ave}$ was similar at the lowest heat flux. The average temperature was constant with the heat flux before increasing as hot spots appeared on the foil. The heat flux where the average temperature began to increase changed with the gap height. For gap heights between 0 μm and 600 μm, the heat flux where this occurred increased as the gap height was increased. However, for gap heights over approximately 600 μm, the heat flux where the average

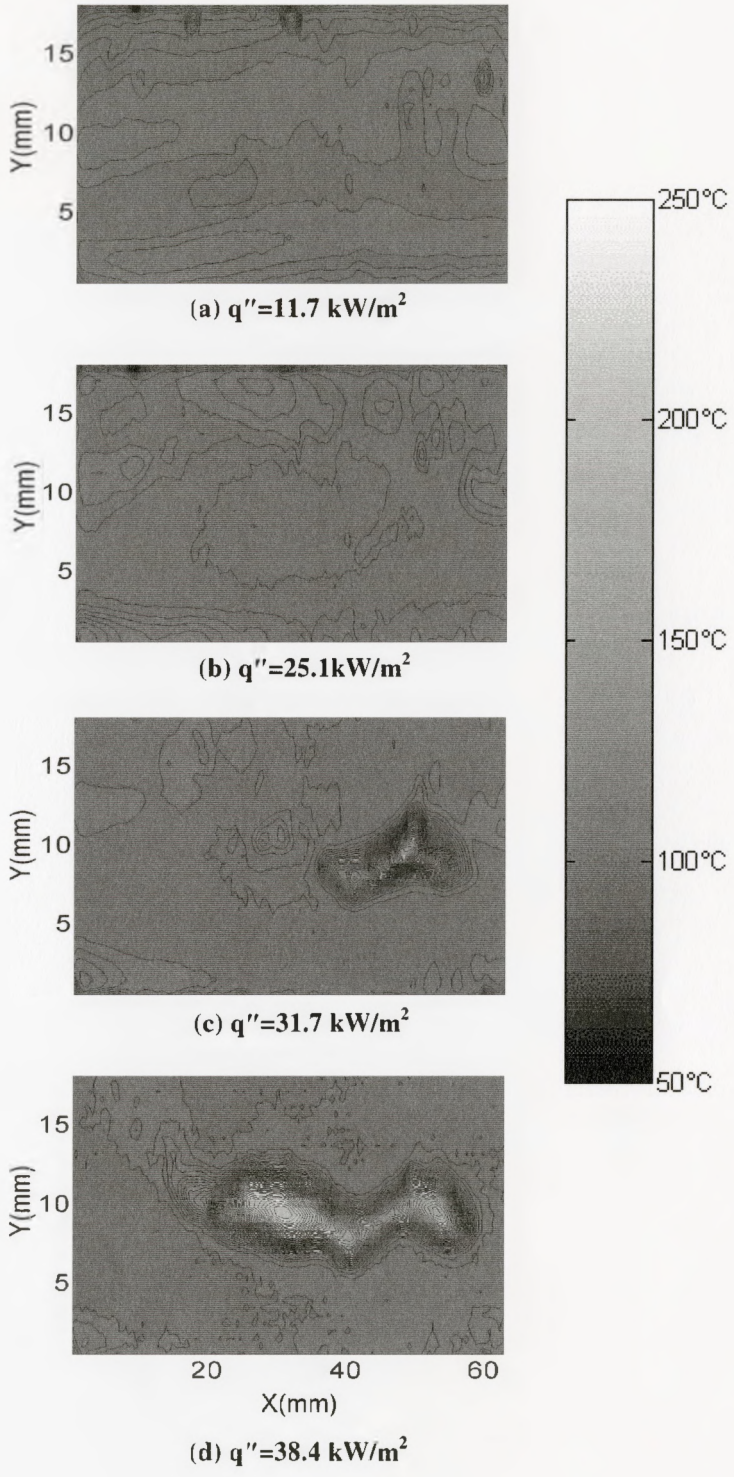

Figure 4.7. Change in the temperature distribution on the foil with heat flux for a 300 μm gap between the foil and the porous plate.

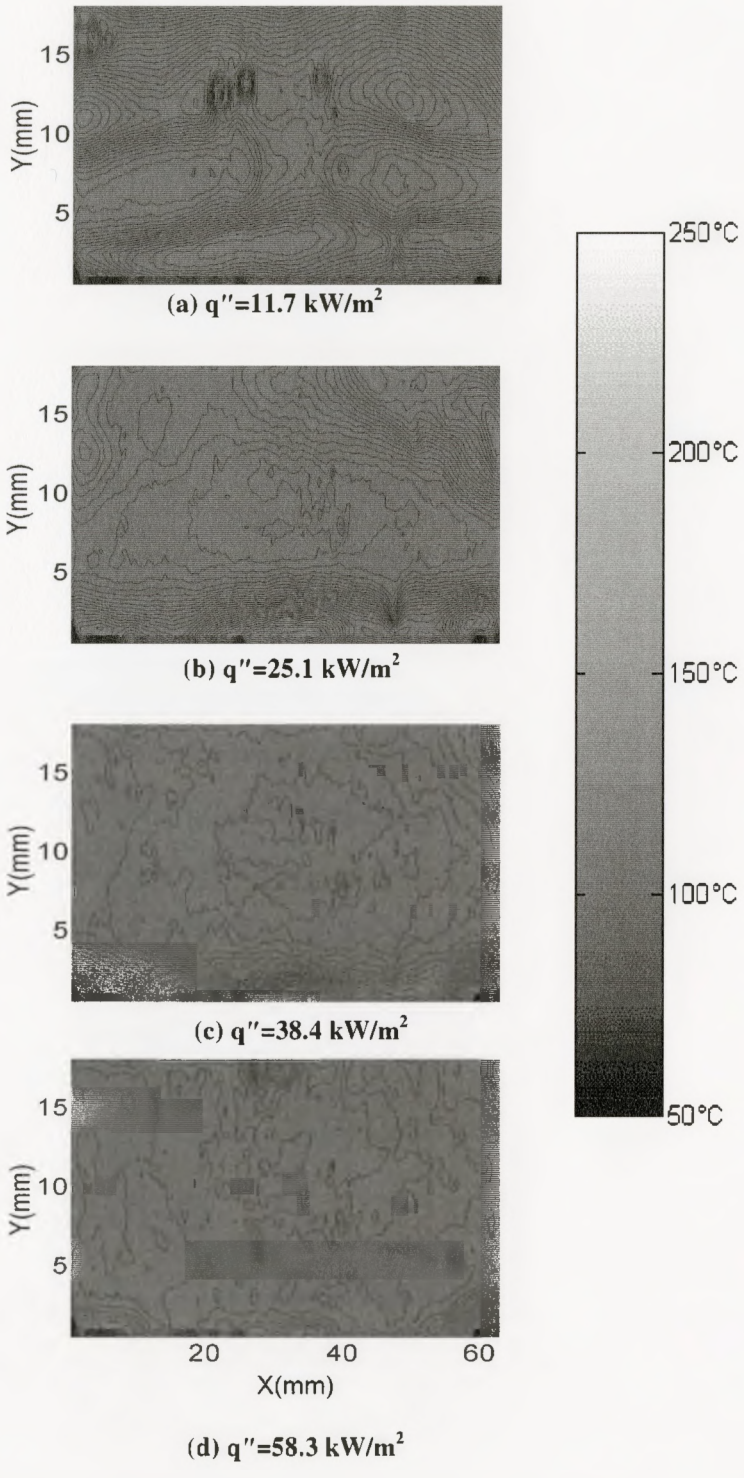

Figure 4.8. Change in the temperature distribution on the foil with heat flux for a 600 μm gap between the foil and the porous plate.

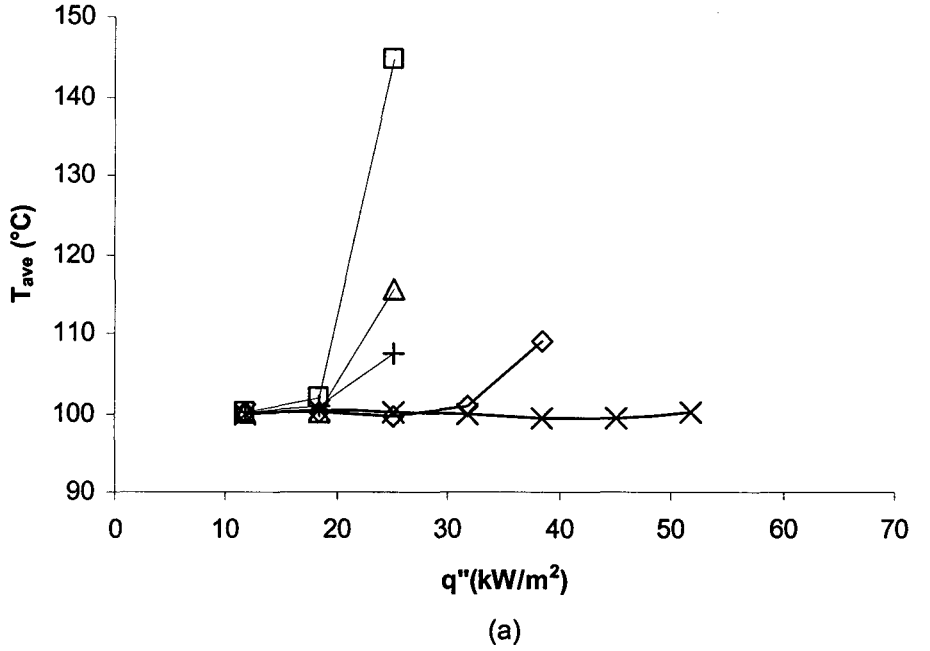

(a)

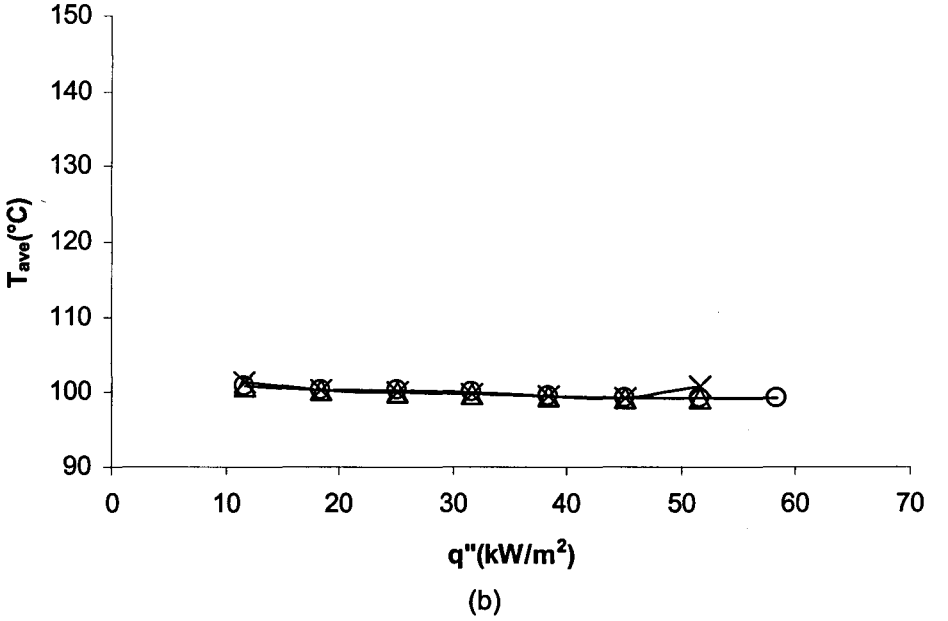

(b)

Figure 4.9. Change in the average temperature $\overline{T}_{ave}$ with heat flux for cases where the gap between the plate and the foil was (a) □ 0 μm , Δ 100 μm, + 200 μm, ◊ 300 μm and × 400 μm, (b) ○ 600 μm , Δ 700 μm, × 1000 μm.

foil temperature increased began to decrease with the gap height. The tests for the gaps of 700 μm and greater were stopped when irreversible hot spots began to appear on the foil, as will be discussed later. Thus, the large increase in the averaged temperature was not observed for these cases.

The change in the averaged heat transfer coefficient with the applied heat flux for these cases is shown in figure 4.10. In all cases, the average heat transfer coefficient initially increased approximately linearly with heat flux since the averaged temperature of the foil was approximately constant. The average heat transfer coefficient then began to decrease as hot spots began to form on the foil and the average temperature of the foil increased. It is clear that the maximum heat transfer coefficient that can be achieved increased from 0.44 kW/m^2 to 1.48 kW/m^2 when the gap height was increased from 0 μm to 600 μm. A further increase in the gap reduced the maximum heat transfer coefficient, down to 1.26 kW/m^2 for a gap height of 1000 μm. Thus, the heat transfer performance of the evaporator section increased as the gap between the foil and the porous plate was increased to 600 μm before decreasing. In all cases, the performance of the heat transfer was limited by the formation of hot spots on the foil similar to those observed at 0 μm gap.

It should be noted that the temperature distribution on the foil was not uniform spatially even when the average temperature was approximately constant. The change in the temperature profile was examined in more detail for the cases where the gap between the foil and porous plate was 300 μm, 600 μm, and 1000 μm. Typical time sequences of the instantaneous temperature distribution on the heating surface when the gap was

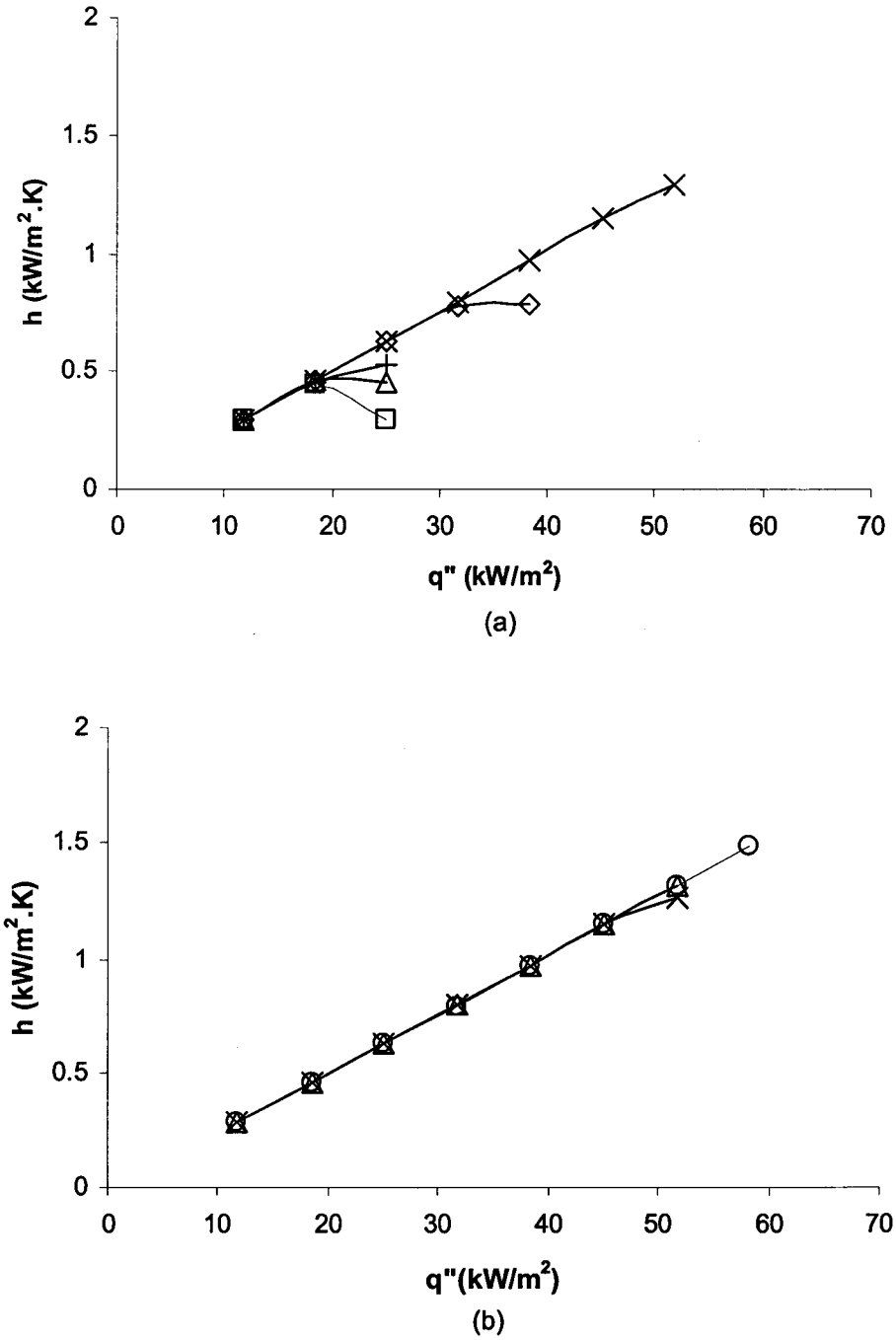

Figure 4.10. Change in the average heat transfer coefficient with heat flux for cases where the gap between the foil and the porous plate was (a) □ 0 μm , Δ 100 μm, + 200 μm, , ◊ 300 μm, × 400 μm, and (b) ○ 600 μm , Δ 700 μm, × 1000 μm.

300 μm for heat fluxes of 11.7 kW/m^2, 18.4 kW/m^2 and 31.7 kW/m^2 are shown in figures 4.11 to 4.13. The scale on these figures was 98°C to 104°C. It is clear that for a heat flux of 11.7 kW/m^2 and for a gap of 300 μm, both superheated regions and cooler saturated regions can be observed on the foil. The movement of these regions can be observed in figure 4.11 and is likely due to the foot print of the nucleation and motion of the vapor in the gap similar to what was visualized by Passos et al (2004). The saturated regions could correspond to regions where evaporation is occurring through a thin liquid film between the heating surface and the generated vapor. In particular, Yao et al(1983) explained the low superheats of 0.6°C observed in these cases by the microlayer evaporation to the vapor bubbles in the confined gap. When the heat flux was increased to 18.4 kW/m^2, more of the foil was at a temperature near the saturation temperature of the water but no high temperature regions were observed as shown in figure 4.12. At 31.7 kW/m^2, a high temperature superheated region appeared where the foil temperature was significantly higher than the saturation temperature. In these cases, the high temperature regions were as large as 140°C. It is thought that these regions may correspond to regions where the liquid is not constantly in contact with the foil. It is not possible to tell from these results if there is rewetting of the surface.

When the gap between the foil and the porous media was 600 μm, there were again superheated regions and saturated regions that coexist on the heating surface. However, in this case, the saturated regions have more rounded shapes, suggesting they correspond to vapor bubbles. The time sequence in figure 4.14 shows that as time increased from 0.000 s to 0.133 s these regions form over the superheated regions and

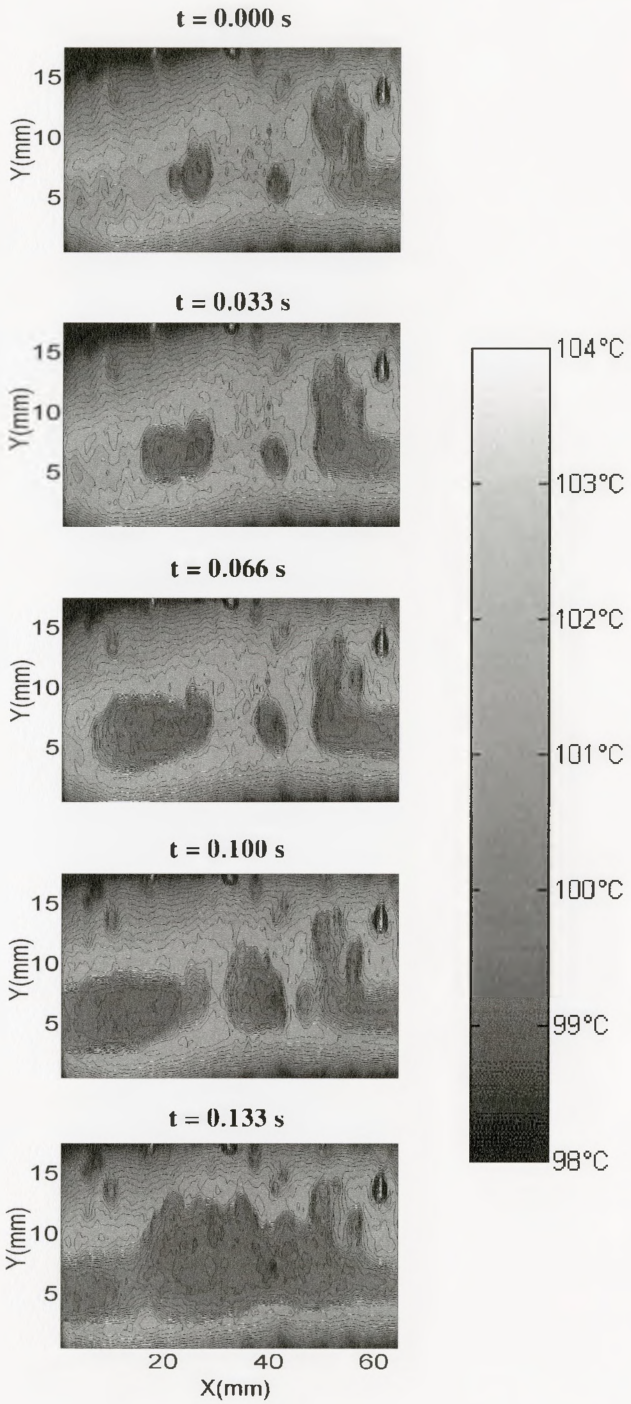

Figure 4.11. Instantaneous temperature distribution for cases where the gap is 300 μm and the heat flux was 11.7 kW/m^2.

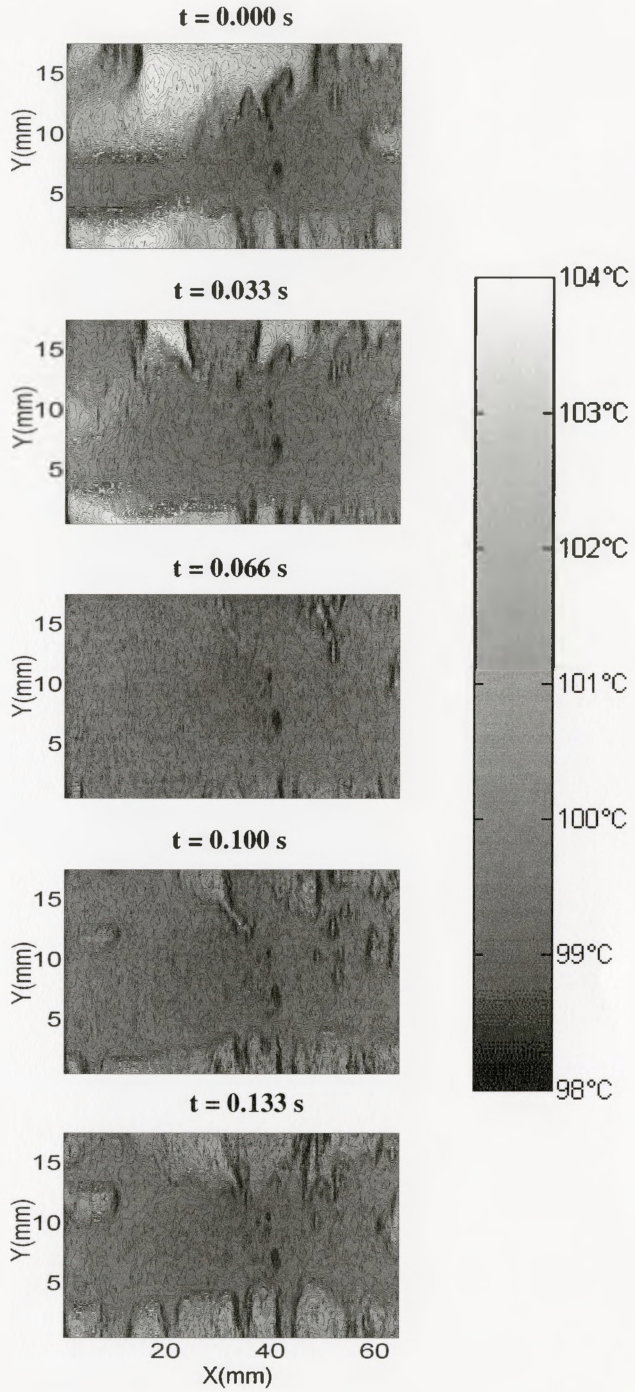

Figure 4.12. Instantaneous temperature distribution for cases **where the gap is 300 μm** and the heat flux was 18.4 kW/m^2.

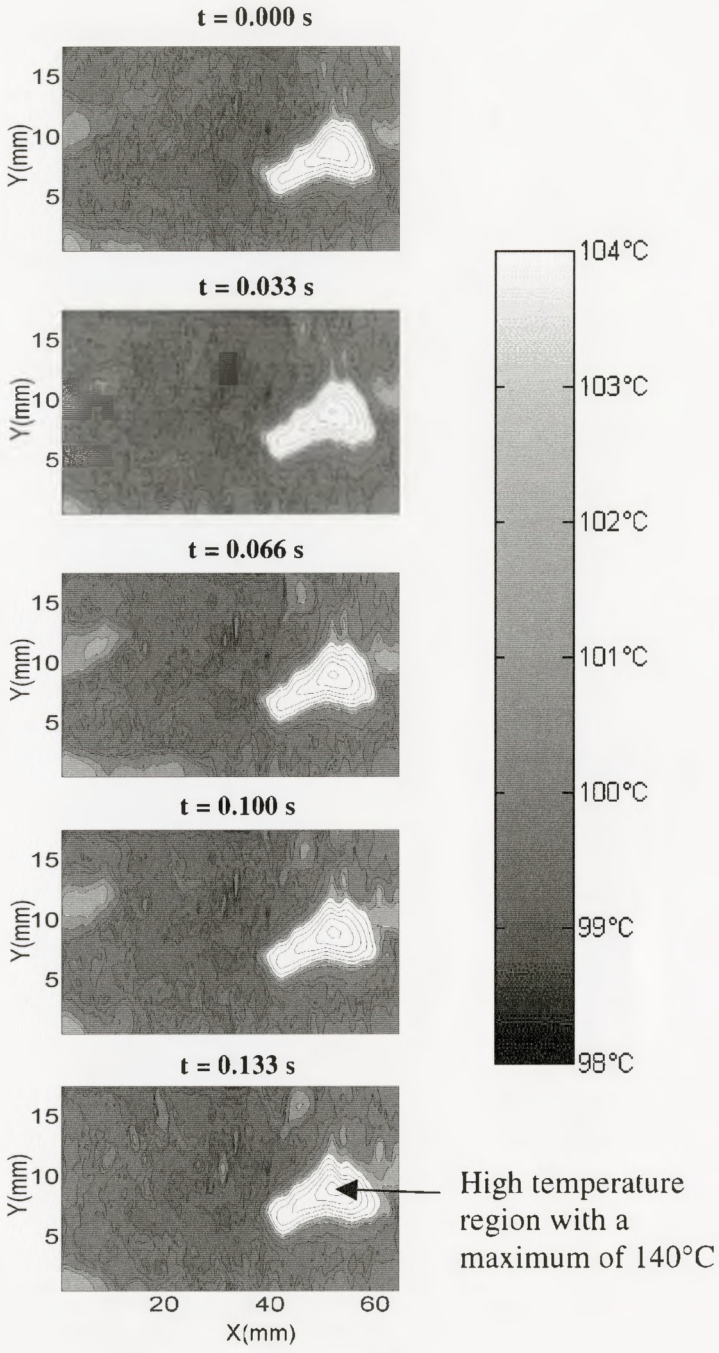

Figure 4.13. Instantaneous temperature distribution for cases where the gap is 300 μm and the heat flux was 31.7 kW/m^2.

began to move through the gap. For a heat flux of 31.7 kW/m^2 more of the foil was near the saturation temperature and no high temperature regions were observed. When the heat flux was further increased to 58.3 kW/m^2, the instantaneous temperature distribution shows that most of the foil is again at the saturation temperature. In this case, however, reversible high temperature regions appeared on the foil as shown in figure 4.16. For example, a high temperature region with a maximum temperature of 125°C appeared at t = 0.066 s and then was no longer present at t = 0.233 s.

When the gap between the foil and the porous media was further increased to 1000 μm, there were moving saturated regions and superheated regions that coexist on the heating surface for a heat flux of 11.7 kW/m^2 as shown in figure 4.17. For a heat flux of 31.7 kW/m^2 more of the foil was near the saturation temperature and no high temperature regions were observed (fig 4.18). When the heat flux was further increased to 51.7 kW/m^2, the instantaneous temperature distribution shows that most of the foil was at the saturation temperature (fig 4.19), with a formation of high temperature regions at t = 0.198 s with a maximum temperature of 160°C that covered a large area of the foil, this region was then no longer present at t = 0.792 s suggesting it was again a reversible high temperature region.

The probability density functions of the temperature distribution on the foil surface for the case of 300 μm gap are shown in figure 4.20.a. For a heat flux of 11.7 kW/m^2 there is a broad peak between 99.2°C and 102.5°C because there are both superheated regions and saturated regions on the foil. When the heat flux was increased to 18.4 kW/m^2 and 25.1 kW/m^2 the distribution narrows and the distribution near the superheated

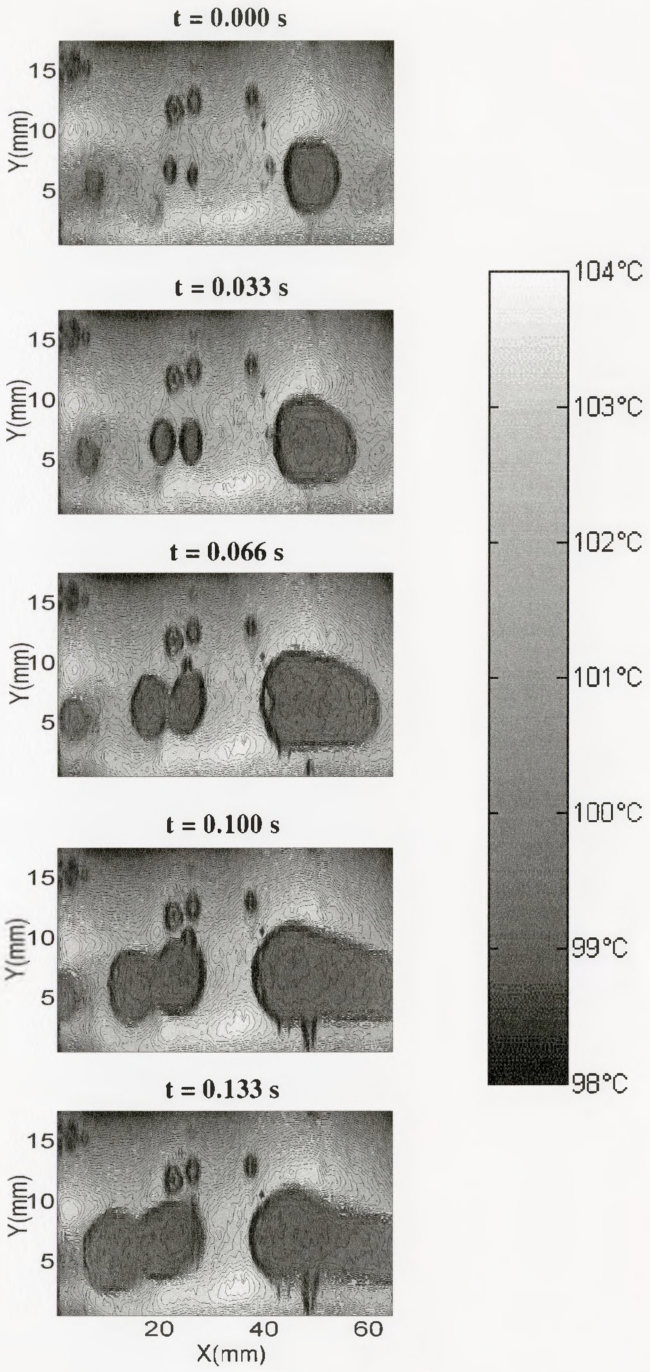

Figure 4.14. Instantaneous temperature distribution for cases where the gap is 600 μm and the heat flux was 11.7 kW/m^2.

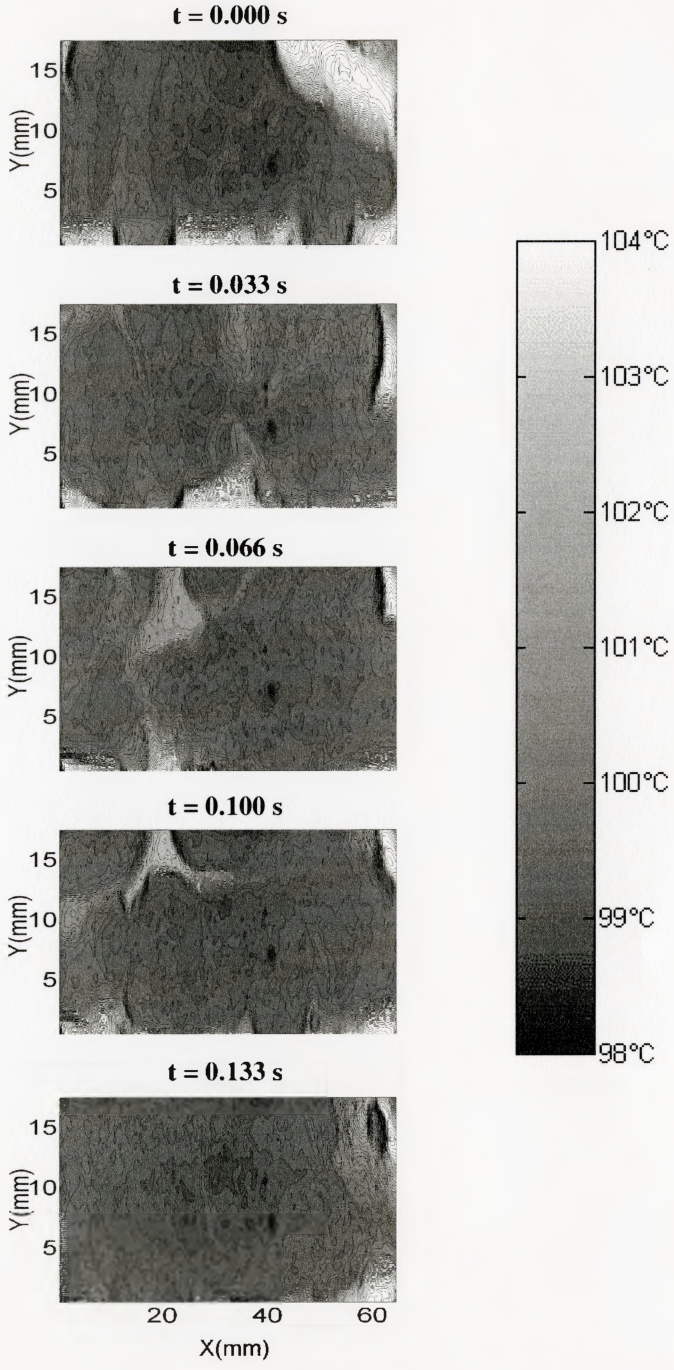

Figure 4.15. Instantaneous temperature distribution for cases where the gap is 600 μm and the heat flux was 31.7 kW/m^2.

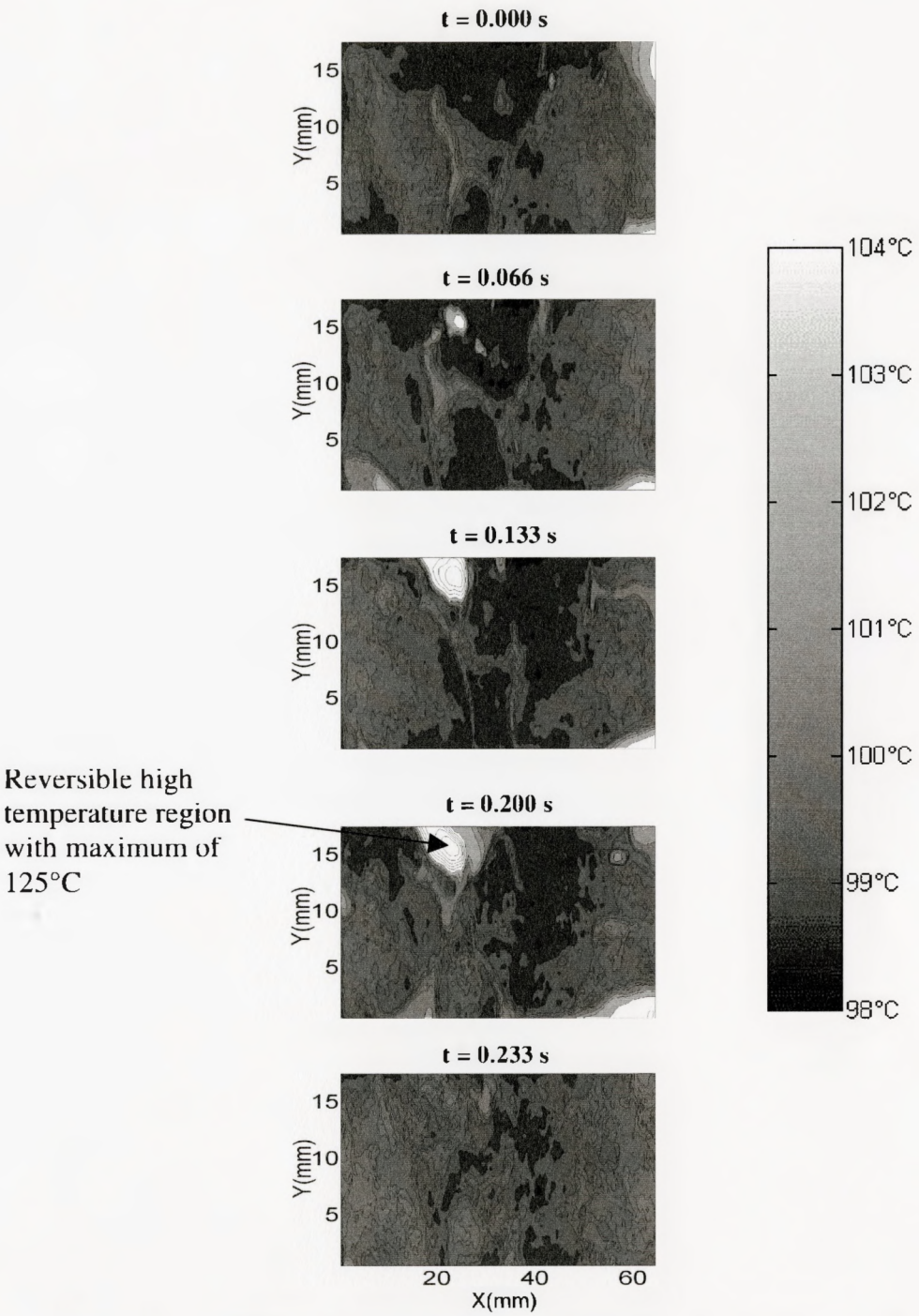

Figure 4.16. Instantaneous temperature distribution for cases where the gap is 600 μm and the heat flux was 58.3 kW/m^2.

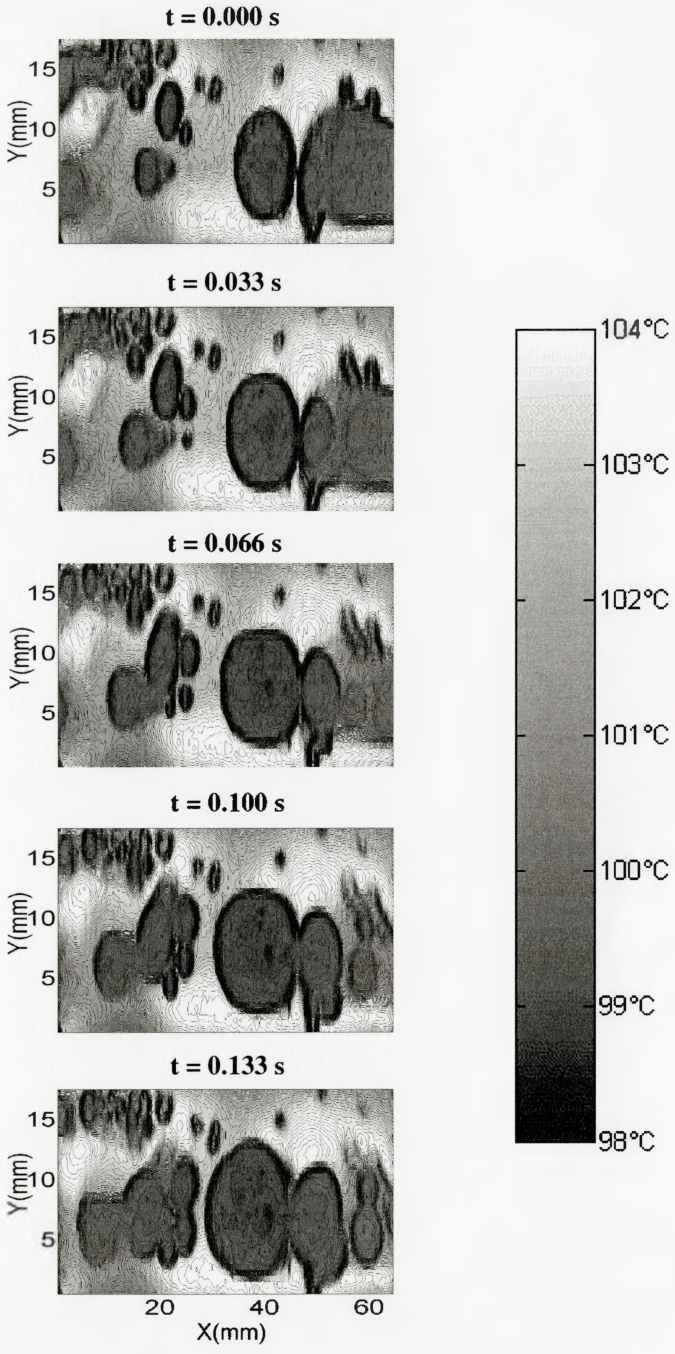

Figure 4.17. Instantaneous temperature distribution for cases where the gap is 1000 μm and the heat flux was 11.7 kW/m^2.

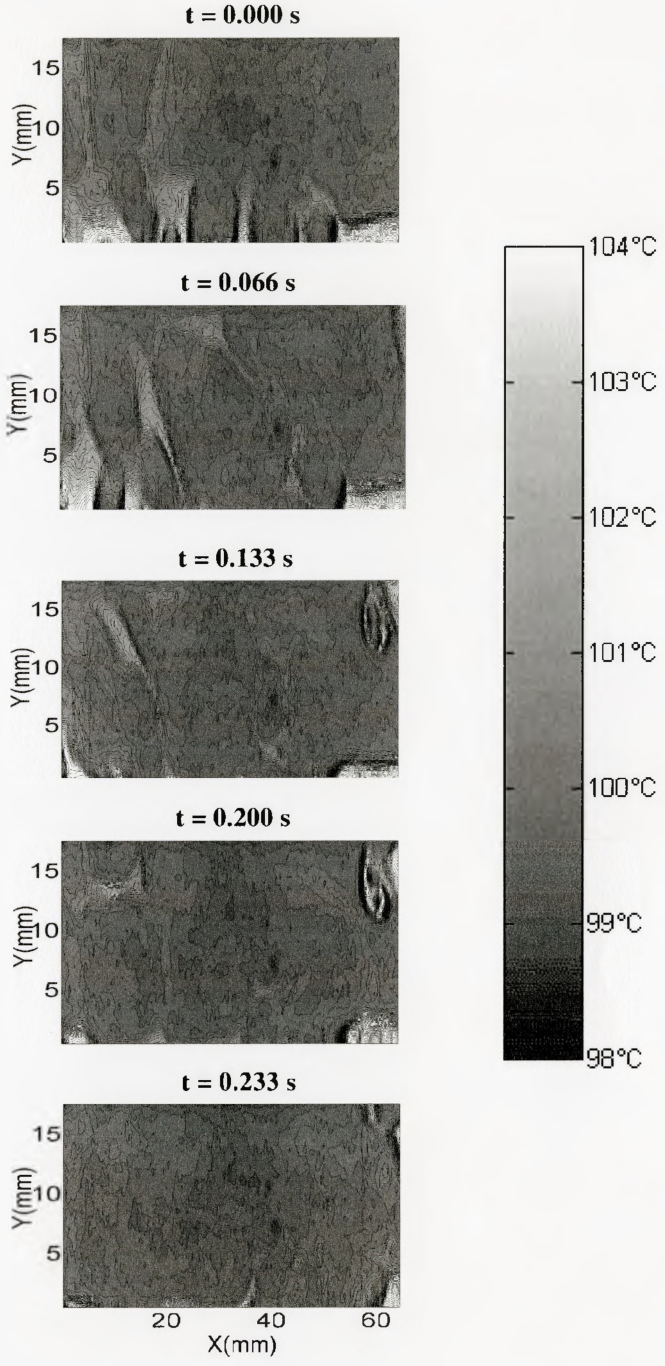

Figure 4.18. Instantaneous temperature distribution for cases where the gap is 1000 μm and the heat flux was 31.7 kW/m^2.

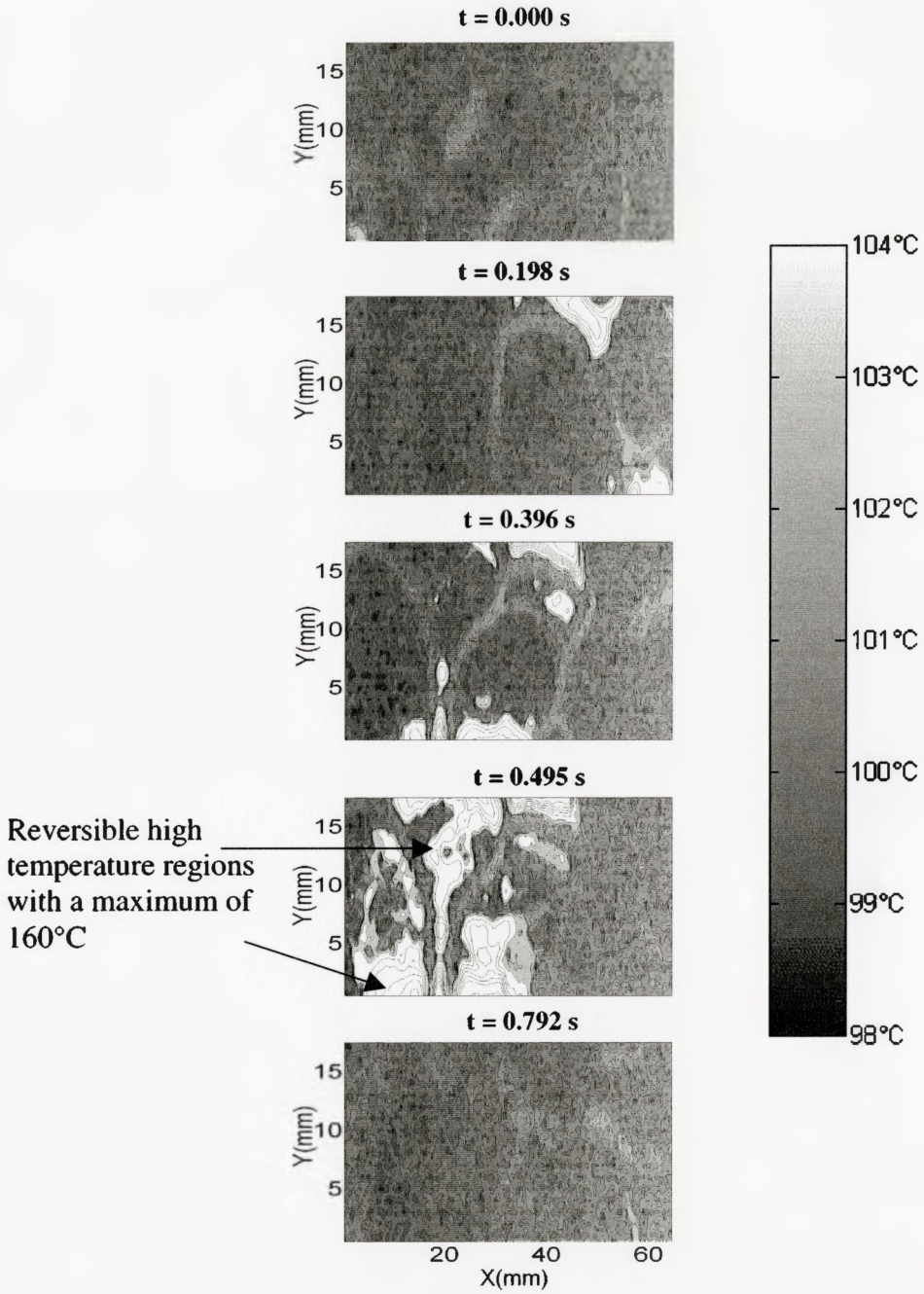

Figure 4.19. Instantaneous temperature distribution for cases where the gap is 1000 μm and the heat flux was 51.7 kW/m^2.

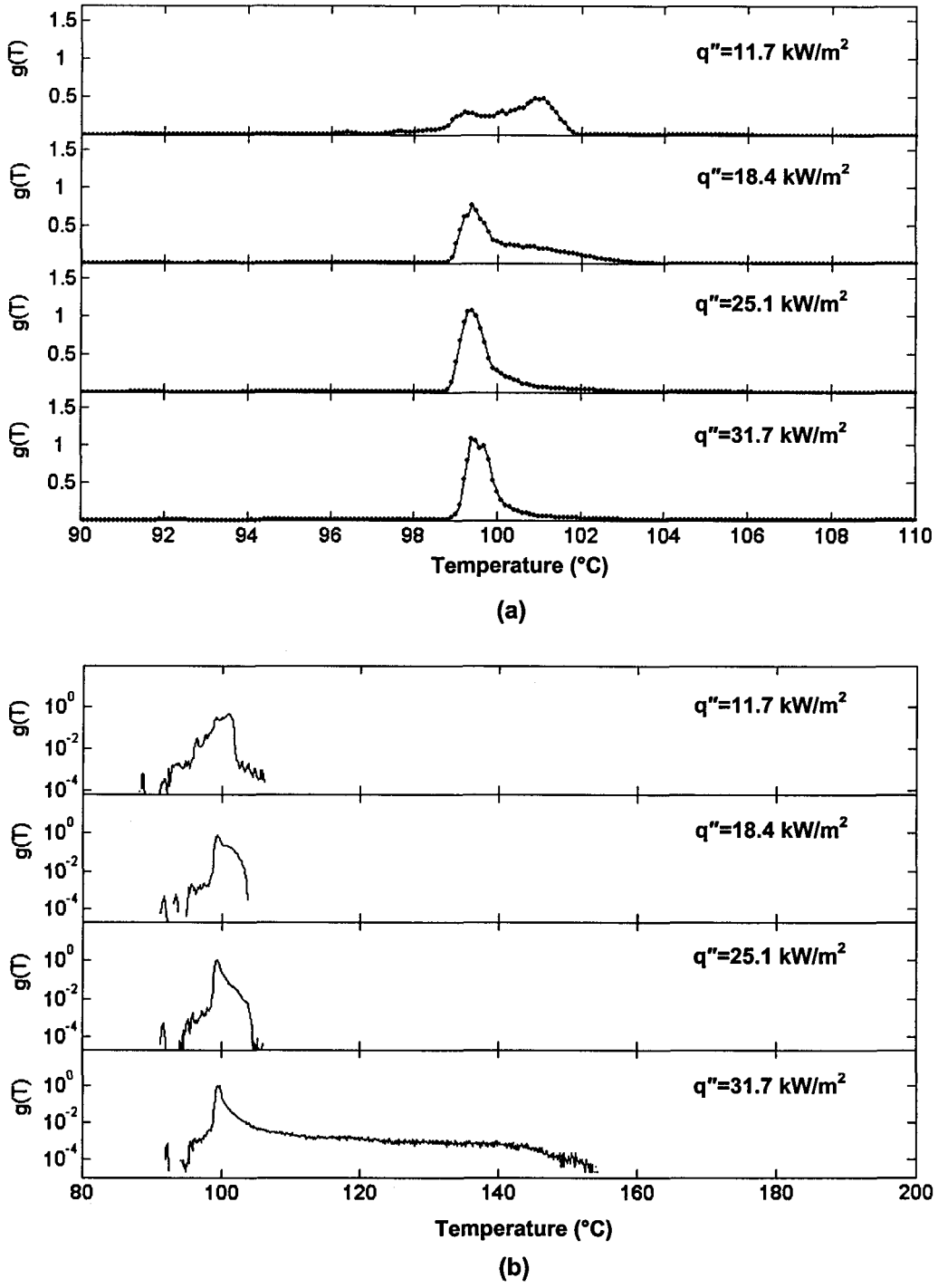

Figure 4.20. Probability density function of the temperature distribution on the foil for a gap of 300 μm (a) on a linear scale and (b) on a logarithmic scale.

region between 100°C and 103°C decreased. This suggests that more of the foil is near the saturation temperature. If the saturated regions are regions where there is microlayer evaporation then it is occurring over more on the heating surface as the heat flux increased. The formation of the high temperature regions on the foil at 31.7 kW/m^2 can be clearly seen in figure 4.20.b where the probability density function is presented on a logarithmic scale. There is a clear tail extending to 154°C that was not observed at any of the lower heat fluxes.

The probability density functions of the temperature distributions on the foil surface for a gap of 600 μm are shown in figure 4.21. At a heat flux of 11.7 kW/m^2, there is again a broad temperature distribution due to the presence of the superheated regions. As the heat flux increased to 45.1 kW/m^2, the distribution narrows with a peak at 99.2°C, that indicates again that more of the surface is near the saturation temperature. The appearance of the reversible hot spots over the heating surface are reflected on figure 4.22.a. In particular, for a heat flux of 45.1 kW/m^2 there is a tail extending to 115°C that extends further to 125°C when the heat flux was increased to 58.3 kW/m^2.

When the gap height was further increased to 1000 μm, the reversible high temperature regions formed on the heating surface at 51.7 kW/m^2 can be seen on the probability density function of the temperature distributions presented on a log scale for different heat fluxes shown in figure 4.22.b. This figure shows that the temperature distribution extended to 190°C at 51.7 kW/m^2 as compared to 125°C for 600 μm gap case at this heat flux (fig. 4.22.a). This indicates there was a deterioration of the heat transfer performance at large gaps because of the increase of the maximum temperature and

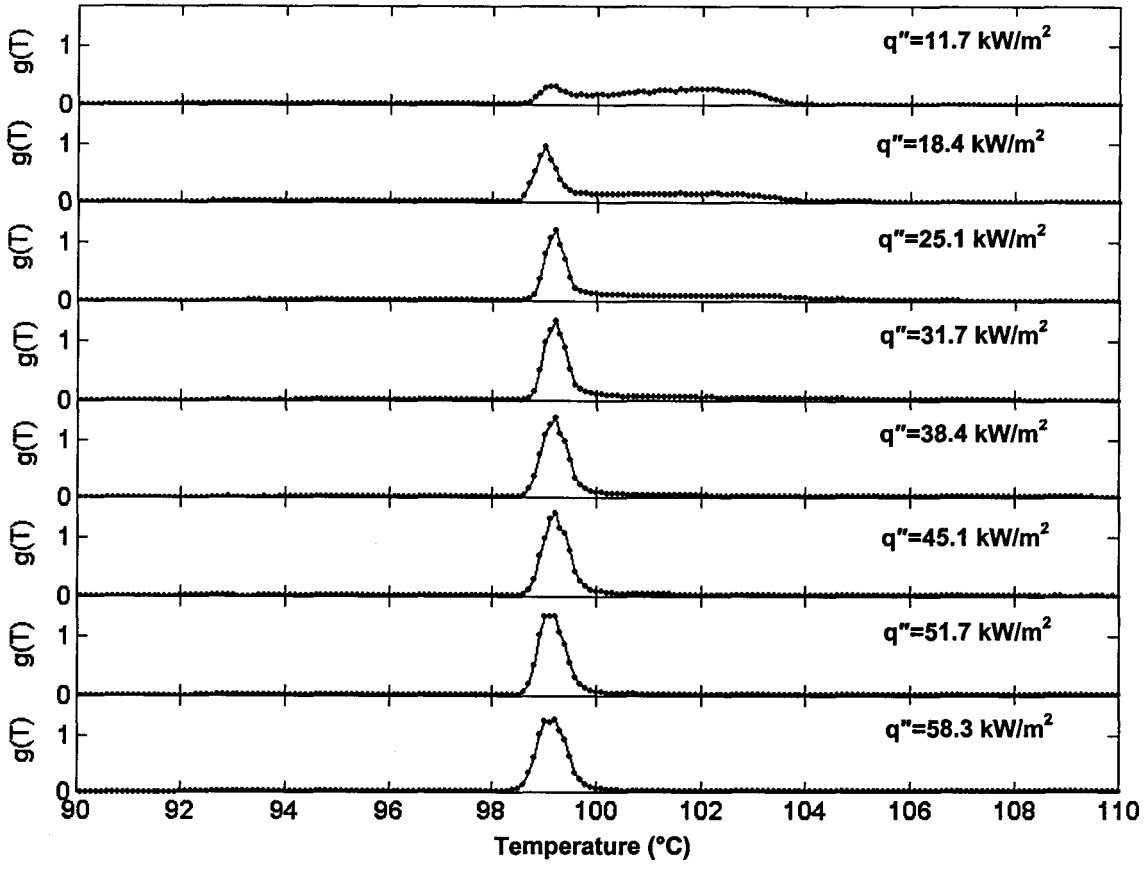

Figure 4.21. Probability density function of the temperature distribution on the foil for a gap of 600 μm for different heat fluxes.

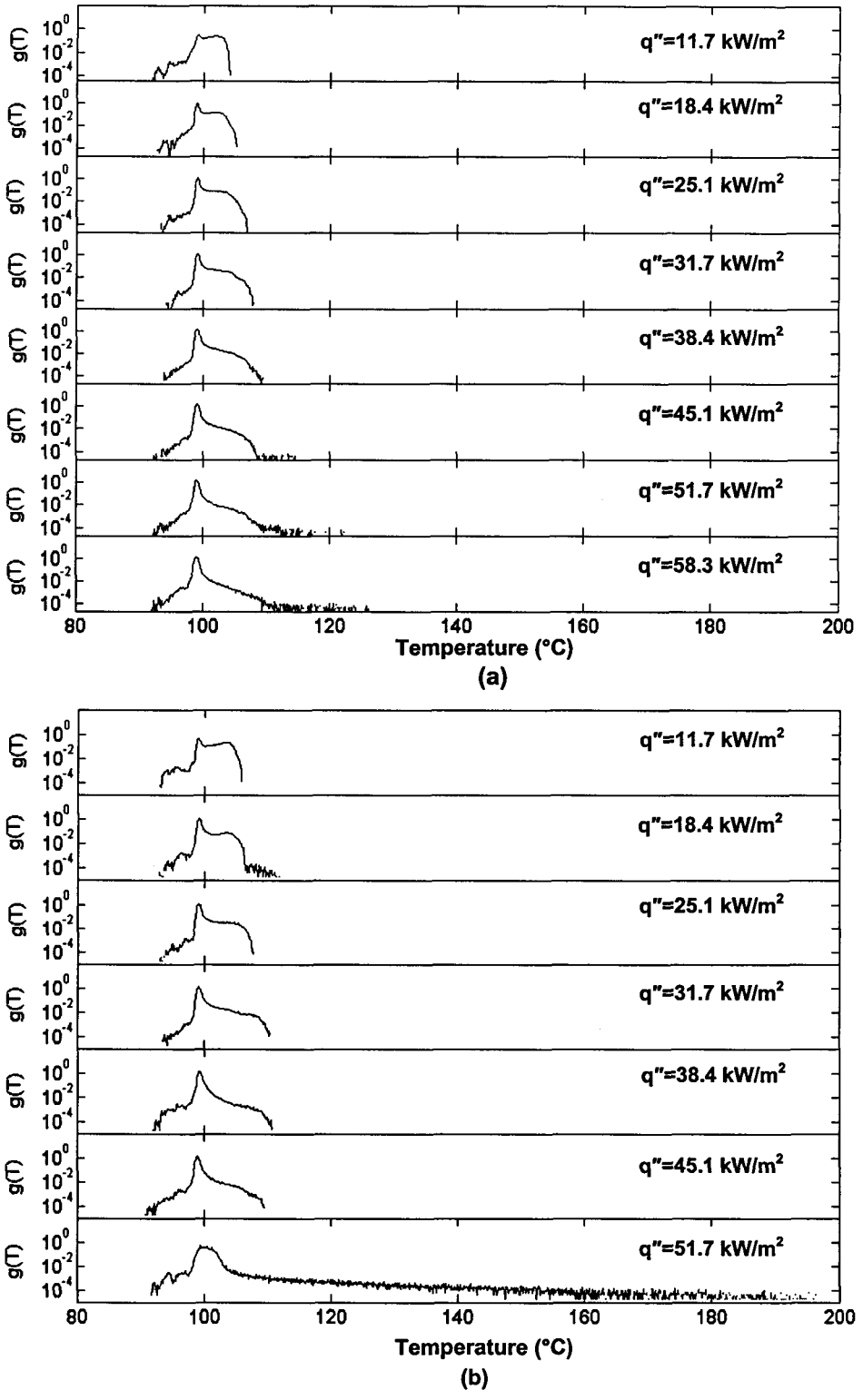

Figure 4.22. Probability density function of the temperature distribution on a logarithmic scale for gaps of (a) 600 μm and (b) 1000 μm.

area covered by the high temperature regions over the foil for the 1000 μm gap case as compared with the 600 μm gap case. One way to explain this result is that the capillary pressure responsible for the replenishment of the evaporative microlayer becomes weaker at higher gap sizes (Lee et al 1992).

The above results have shown that when the heat flux was applied to the heating surface, there was boiling in the confined space between the heating surface and the saturated porous structure. The formation of the high temperature regions on the foil surface at 0 μm gap occurred for a heat flux of 18.4 kW/m^2, where as it occurred at a heat flux of 31.7 kW/m^2 for the case of 300 μm gap. At a gap height of 600 μm, the high temperature regions were not observed and only reversible hot spots appeared over the heating surface for a heat flux of 58.3 kW/m^2. Therefore, these results indicate that increasing the gap height from 0 μm to 600 μm enhanced the heat transfer performance because it delays the formation of the hot spots on the heating surface to higher heat fluxes. This can be explained by the fact that when the gap height is increased, it permits more vapor generated at high heat fluxes to be released without formation of hot spots on the heating surface. It is thought that as the gap height is increased, the vapor would be released through the gap without travelling through the porous media.

4.2. Effect of the subcooled liquid temperature on the confined boiling.

The effect of the subcooling below the porous plate on the heat transfer process was examined by repeating the measurements at different gap heights for the cases where the liquid temperature below the porous plate was at 75°C and 90°C. The time averaged

temperature distributions on the foil at a heat flux of 11.7 kW/m^2 for the different liquid temperatures when the foil was in contact with the porous plate are shown in figure 4.23. It is clear that when the liquid temperature was at 75°C and 90°C most of the foil surface was near the saturation temperature but there were regions of high average temperature present on the foil. This differs from the case where the liquid was at 60°C discussed above when the foil temperature was uniform. The maximum time averaged temperature was 125°C for the case where the incoming liquid was at 90°C, and 150°C when the liquid was at 75°C. The average temperatures of the foil $\overline{T}_{ave}$ was 100.1°C, 100.4°C and 105.0°C for the cases where the subcooled liquid temperatures were 60°C, 75°C and 90°C respectively. The differences in the average temperatures are due to the presence of the localized high temperature regions for the 75°C and 90°C subcooled liquid temperature cases.

The temperature distributions on the heating surface for a gap height of 100 μm and subcooled liquid temperatures of 60°C, 75°C and 90°C are shown in figure 4.24. For a heat flux of 11.7 kW/m^2 the entire foil surface had a time averaged temperature distribution close to the saturation temperature for all liquid temperatures (figures 4.24.i.a-iii.a). For a heat flux of 18.4 kW/m^2, however, localized hot spots were present in the time averaged temperature distributions. The maximum temperatures were 121°C, 180°C and 159°C for the cases of subcooled liquid temperatures of 60°C, 75°C and 90°C respectively (figures 4.24.i.b-iii.b). When the heat flux was further increased to 25.1 kW/m^2, the high temperature regions expanded on the heating surface for all the cases.

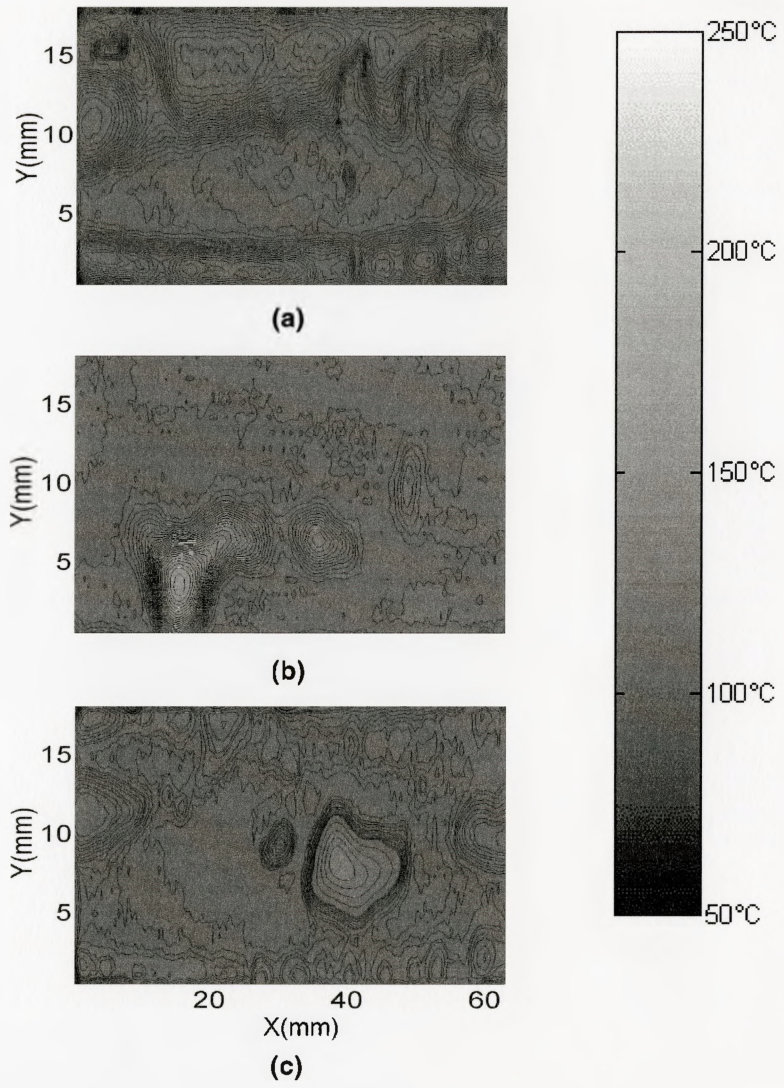

Figure 4.23. Time average temperature distribution for a zero gap and a heat flux of 11.7 kW/m^2 for (a) liquid temperature of 60°C, (b) liquid temperature of 75 °C, and (c) liquid temperature of 90°C.

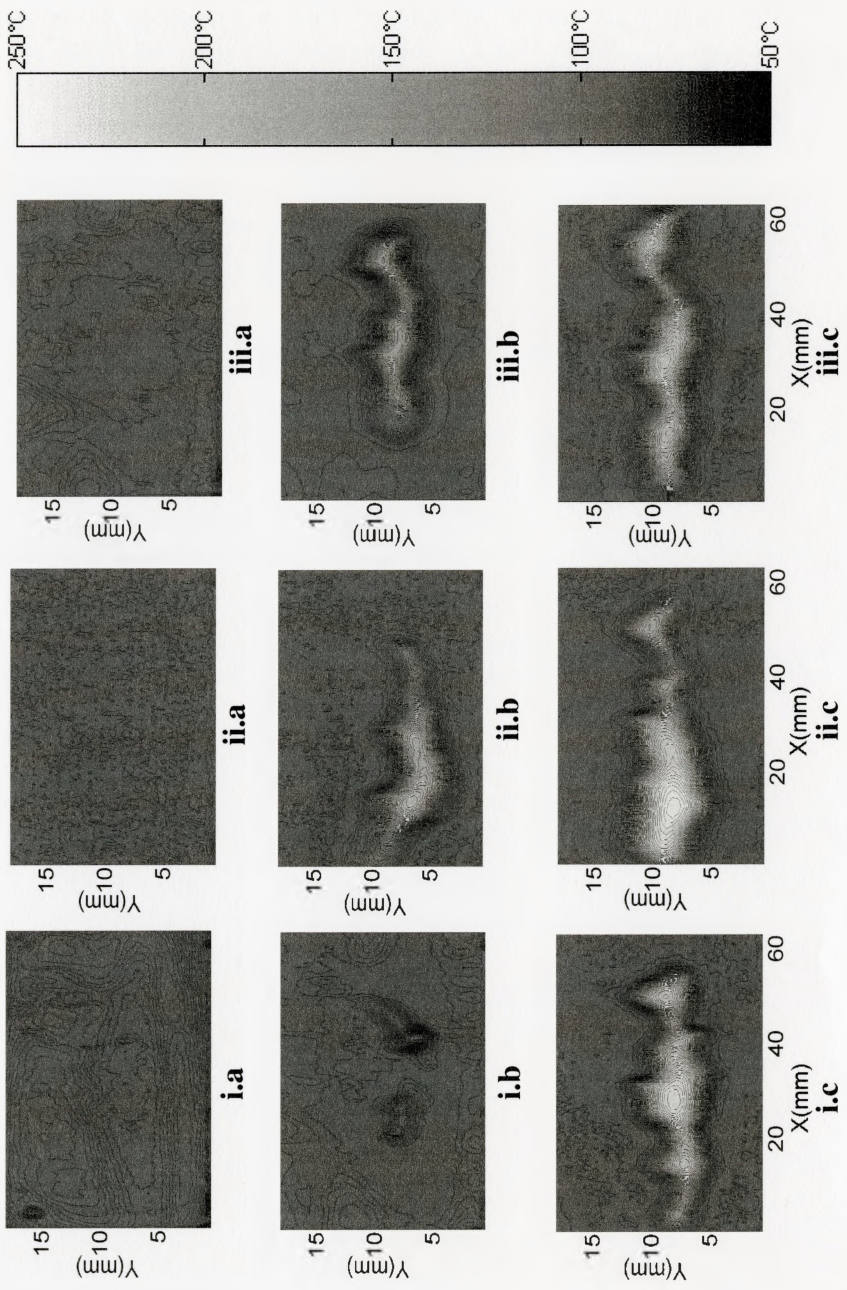

Figure 4.24. Time averaged temperature contours for a gap of 100 μm and (i) a liquid temperature of 60°C, (ii) a liquid temperature of 75°C, (iii) a liquid temperature of 90°C, and (a) an applied heat flux of 11.7 kW/m^2, (b) an applied heat flux of 18.4 kW/m^2 and (c) an applied heat flux of 25.1 kW/m^2.

There were smaller differences in the time average temperature profiles when the gap height was increased to 200 μm, and when the gap height was increased to 600 μm, the time averaged contours obtained were similar for all liquid temperatures. For example, a comparison of the average temperature distribution for a gap of 600 μm at three heat fluxes of 11.7 kW/m^2, 31.7 kW/m^2 and 51.7 kW/m^2 is presented in figure 4.25. In this case the time average temperatures over the surface were near 100°C in all the cases. The maximum temperature obtained on the temperature contours at a heat flux of 51.7 kW/m^2 were less than 106°C for this gap height.

The variation of the spatially averaged temperature $\overline{T}_{ave}$ on the foil with heat flux for the three liquid temperatures of 60°C, 75°C and 90°C and for gaps of 100 μm, 200 μm and 600 μm are shown in figures 4.26 through 4.28. For the gaps of 100 μm and 200 μm the average temperature on the foil for a given heat flux depended on the temperature of the liquid below the porous plate. When the gap was 600 μm, the temperature of the foil was independent of the liquid subcooling over the range tested. The results indicate that similar heat transfer characteristics were obtained for the different subcooled liquid temperatures, suggesting that the temperature of the liquid below the porous plate does not significantly effect the heat transfer in the confined gap over the porous structure.

The time averaged probability density functions of the temperature distributions for the liquid temperatures of 60°C, 75°C and 90°C at a gap height of 600 μm are shown in figures 4.29.a through 4.31.a. For a heat flux of 11.7 kW/m^2, the temperature distributions had one peak near 100°C, with a second broader distribution extending to 104°C indicating the presence of the saturated and superheated regions under the heating

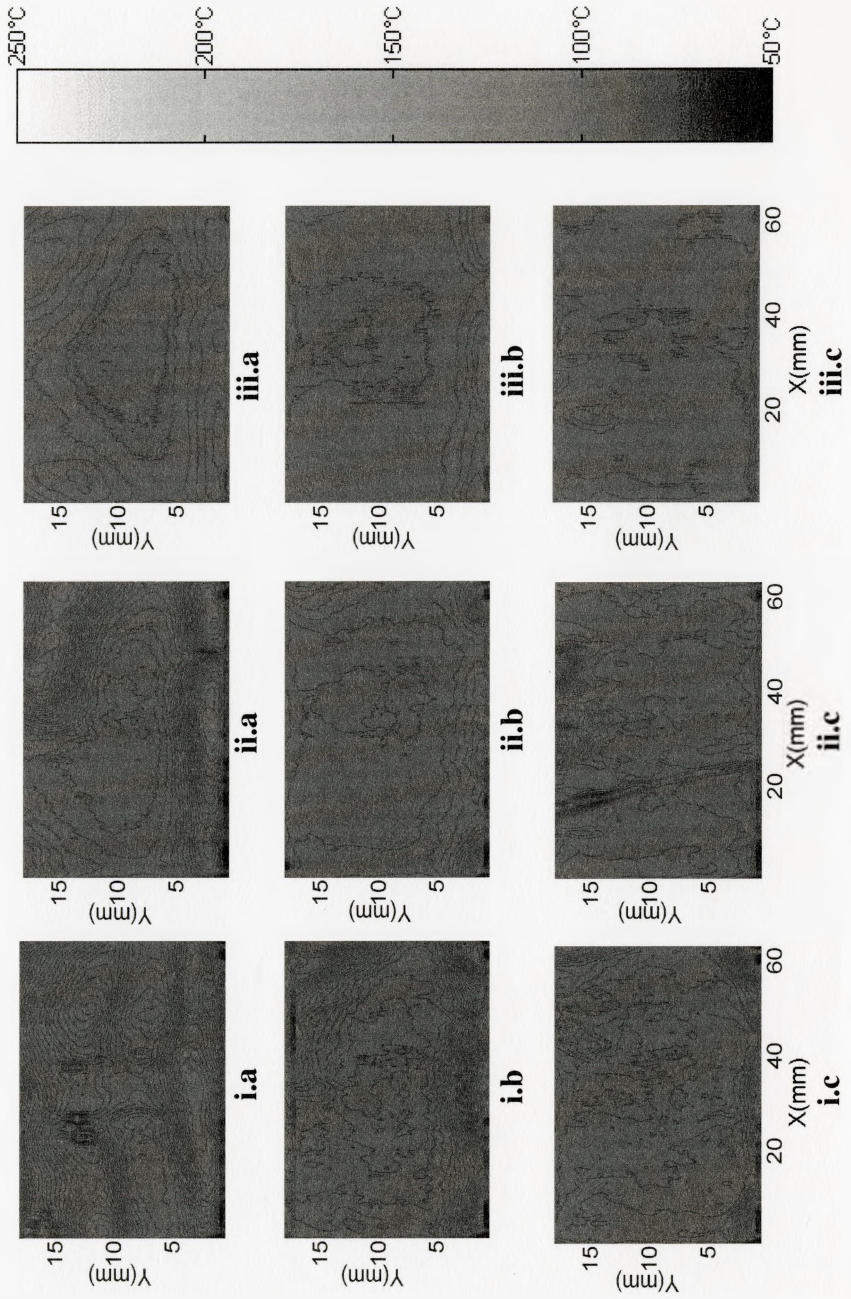

Figure 4.25. Time averaged temperature contours for a gap of 600 μm, (i) a liquid temperature of 60°C, (ii) a liquid temperature of 75°C, (iii) a liquid temperature of 90°C, and (a) an applied heat flux of 11.7 kW/m^2, (b) an applied heat flux of 31.7 kW/m^2, and (c) an applied heat flux of 51.7 kW/m^2.

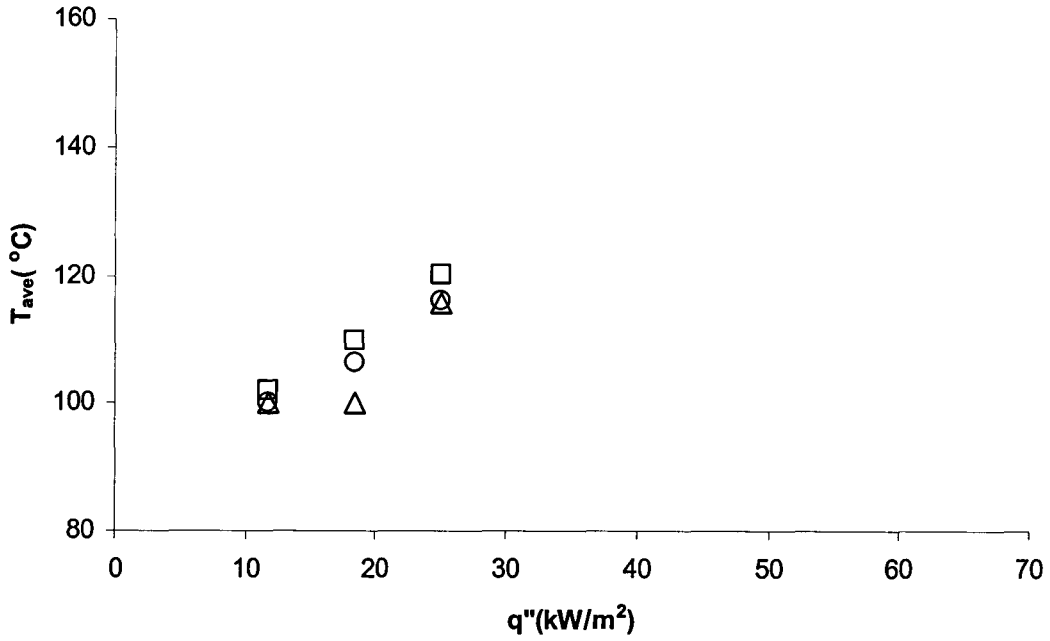

Figure 4.26. Comparison of the average temperature of the foil $\overline{T}_{ave}$ for a gap of 100 μm and Δ a liquid temperature of 60°C, □ a liquid temperature of 75°C, ○ a liquid temperature of 90°C.

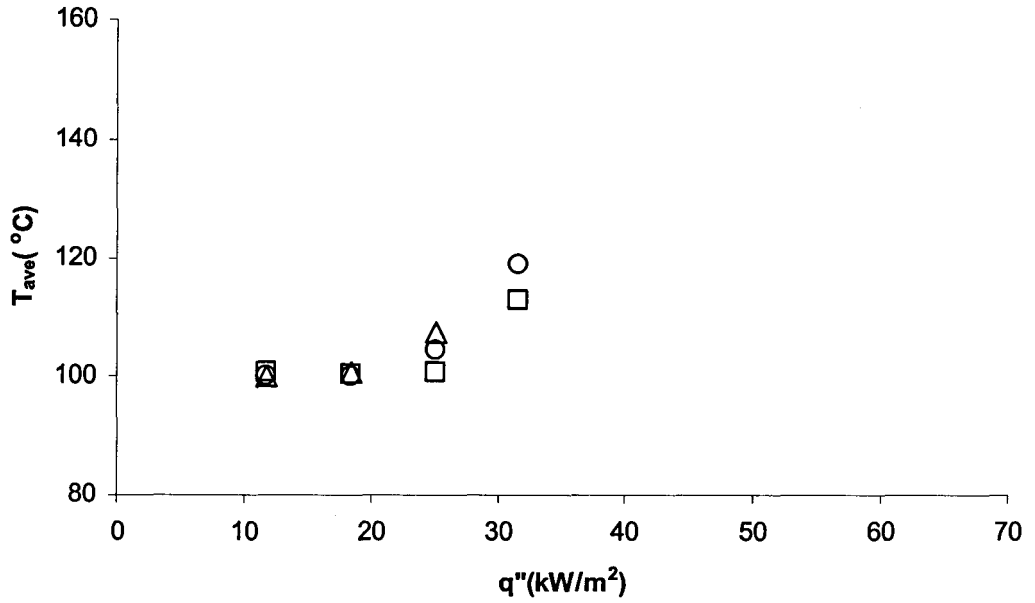

Figure 4.27. Comparison of the average temperature $\overline{T}_{ave}$ for a gap of 200 μm and Δ a liquid temperature of 60°C, □ a liquid temperature of 75°C, ○ a liquid temperature of 90°C.

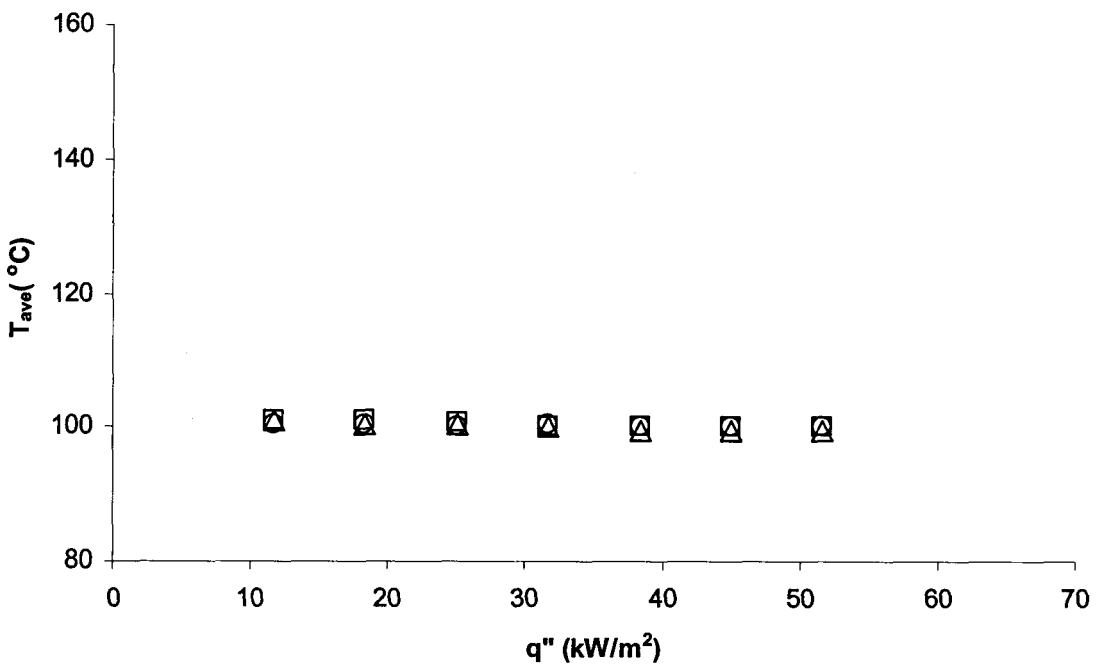

Figure 4.28. Comparison of the average temperature $\overline{T}_{ave}$ for a gap of 600 μm and Δ a liquid temperature of 60°C, □ a liquid temperature of 75°C, ○ a liquid temperature of 90°C.

foil. When the heat flux was increased to 18.4 kW/m^2 the temperature distribution between 100°C and 104°C decreased for all liquid temperatures. Finally, for a heat flux of 45.1 kW/m^2 the distribution presented a sharp peak near 100°C for all subcooled liquid temperature cases indicating most of the foil surface was at the saturation temperature of water in all cases.

Note that the temperature at the peaks near 100°C in the probability density function of the temperature distributions changed slightly when the heat flux was increased from 11.7 kW/m^2 to 45.1 kW/m^2. In particular, it changed from 99.1°C to 99.2°C for the liquid temperature of 60°C, and from 99.8°C to 100°C and 99.7°C to 100.1°C for liquid temperatures of 75°C and 90°C respectively. It was thought that these changes in the temperature at the peaks were due to the error of the temperature measurements of the thermal imaging camera rather than changes in the foil temperature. The temperature distributions presented on a logarithmic scale for the cases of subcooled liquid temperatures of 60°C, 75°C and 90°C are shown in figures 4.29.b-4.31.b. These figures show that the temperature distributions extended only to a maximum of 106°C for heat fluxes of 11.7 kW/m^2 and 18.4 kW/m^2 due to the presence of the superheated region on the foil surface. When the heat flux was increased to 45.1 kW/m^2, the temperature distributions extended to maximum temperatures of 111°C to 116°C due to the formation of reversible high temperature regions on the foil. The probability density functions of the temperature distribution for the three subcooled liquid temperatures were suggesting the same heat transfer mechanisms were occurring for all subcooled liquid temperatures. Thus, the results suggest that the subcooled liquid temperature did not have a significant

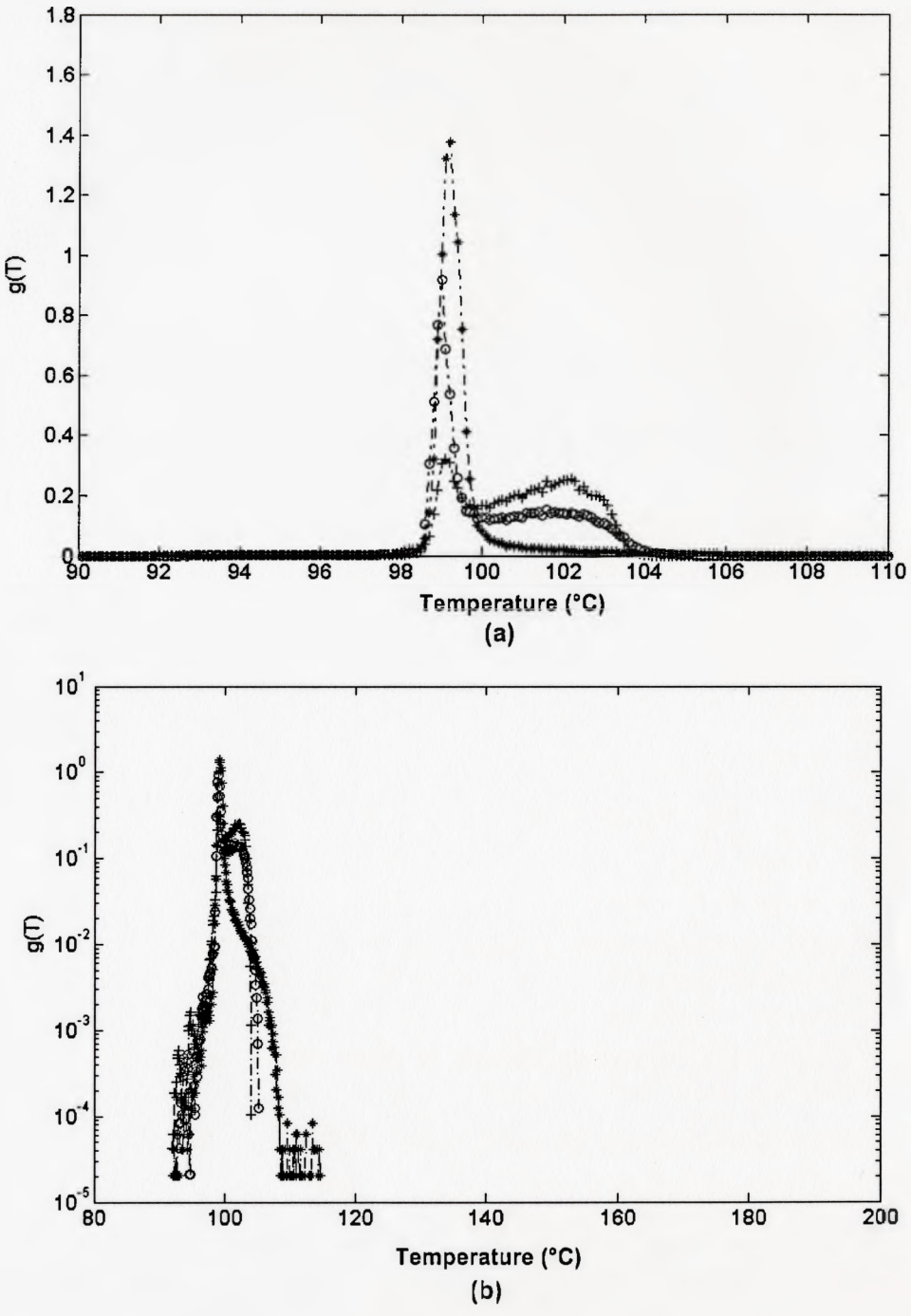

Figure 4.29. Temperature distribution on the foil surface for a gap of 600 μm and a subcooled liquid temperature of 60°C, and at heat fluxes of q" of + 11.7 kW/m^2, ○ 18.4 kW/m^2, * 45.1 kW/m^2, for (a) linear scale, (b) logarithmic scale.

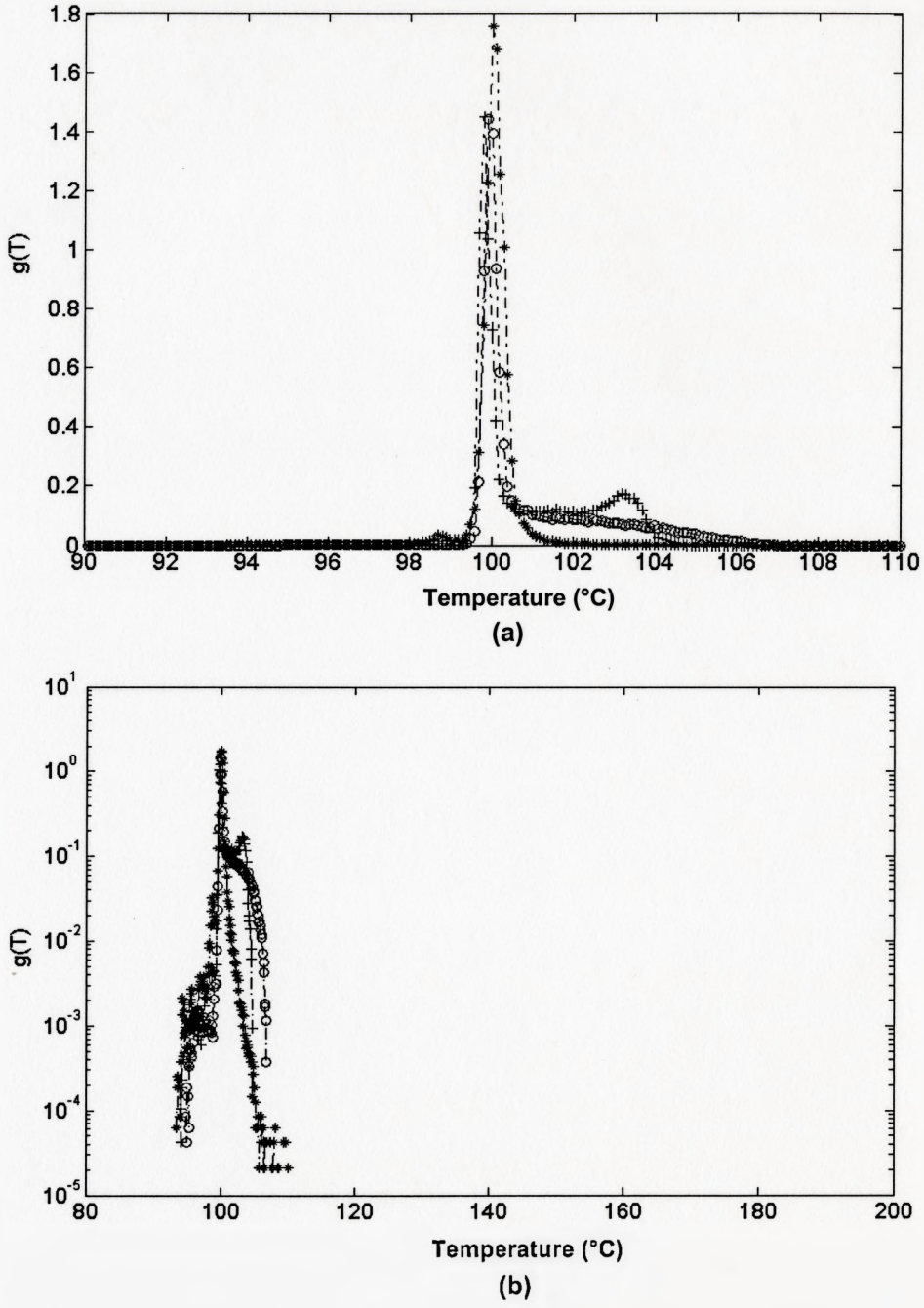

Figure 4.30. Temperature distribution on the foil surface for a gap of 600 μm and a liquid temperature of 75°C and at heat fluxes q″ of + 11.7 kW/m^2, ○ 18.4 kW/m^2, * 45.1 kW/m^2 for (a) linear scale, (b) logarithmic scale.

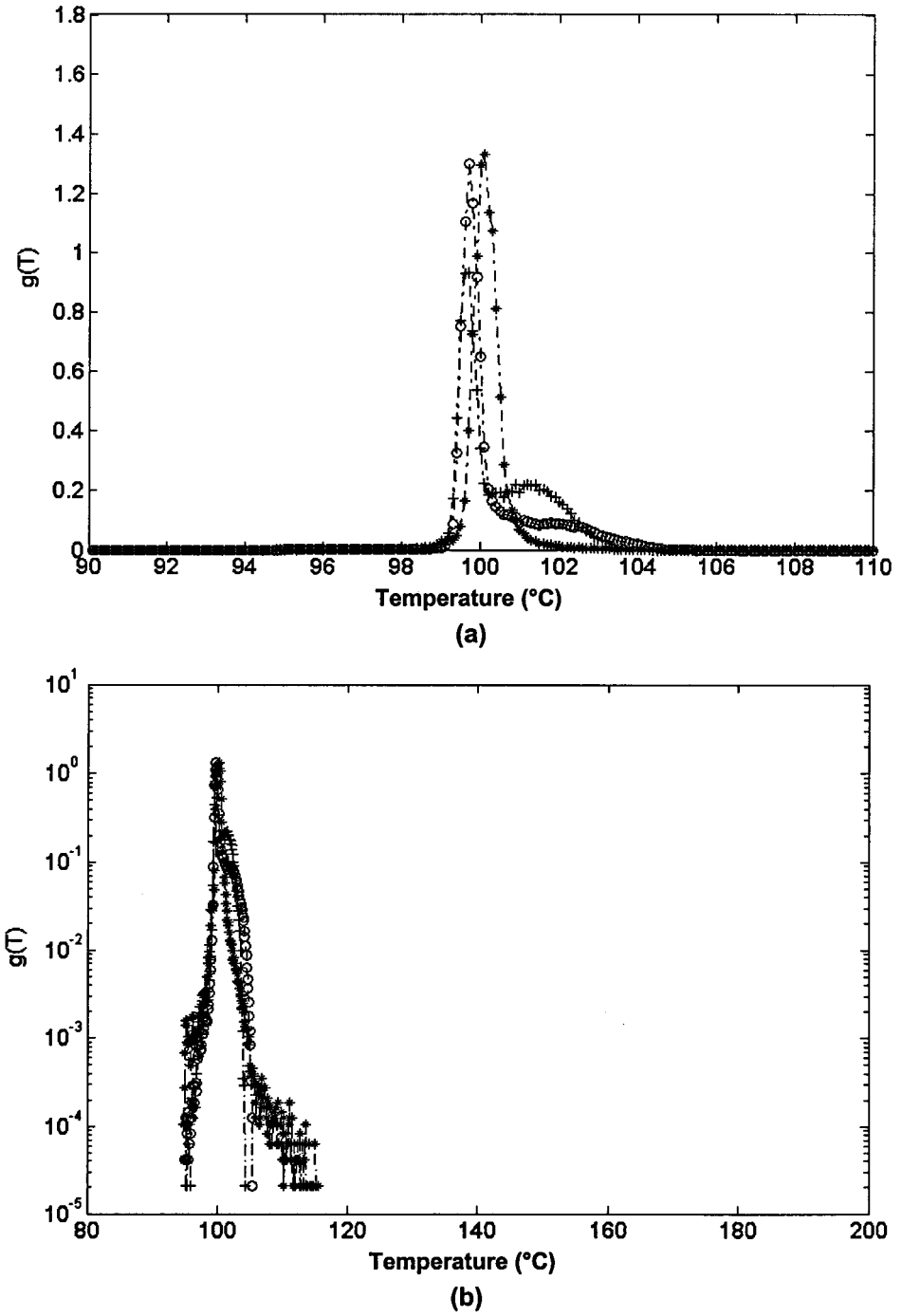

Figure 4.31. Temperature distribution on the foil surface for a gap of 600 μm and a liquid temperature of 90°C, and at heat fluxes q″ of + 11.7 kW/m^2, ○ 18.4 kW/m^2, * 45.1 kW/m^2 for (a) linear scale, (b) logarithmic scale.

effect on the boiling mechanism in the confined gap over the saturated porous structure in this experiment.

4.3. Effect of the pore size on the confined boiling

The effect of the pore size in the porous structure on the heat transfer to the liquid in the gap between the heated surface and the porous media was examined by performing measurements for a porous structure with a characteristic pore size of 200 μm for an inlet liquid temperature of 75°C. The experiments were performed for gaps of 0 μm, 100 μm, 200 μm and 600 μm between the heated surface and the porous plate and compared to the results for the porous plate with a 50 μm pore size. A comparison of the time averaged temperature contours for a 0 μm gap between the foil and the two plates and at a heat flux of 11.7 kW/m^2 is shown in figure 4.32. It is clear that a region of high time averaged temperature occurred on part of the foil surface for both cases, but the high temperature region was much larger for the porous plate with the 200 μm pore size. As a result, the spatially averaged temperatures $\overline{T}_{ave}$ were 105°C and 113°C for the 50 μm and 200 μm pore size cases. Thus, it is clear that higher thermal resistance is obtained for the plate with the larger pore size.

The time averaged temperature contours for a gap of 100 μm are shown in figure 4.33. At a heat flux of 11.7 kW/m^2, the temperature distribution was nearly uniform at 100°C for the 50 μm pore size, but a region of high temperature formed on the foil surface for the 200 μm pore size. When the heat flux was increased to 18.4 kW/m^2, a high temperature region started to form on the foil for the 50 μm pore size porous plate,

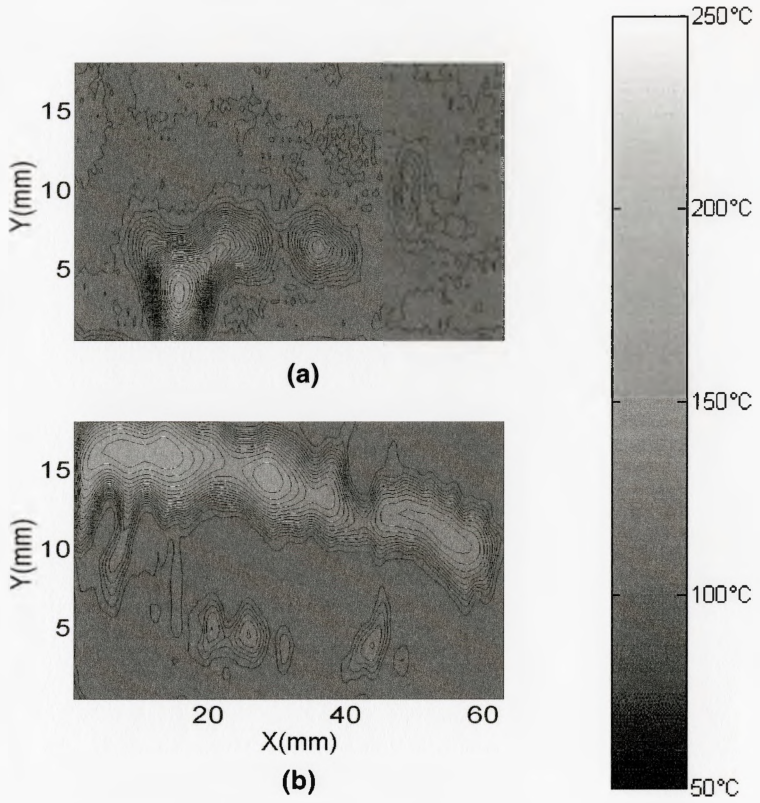

Figure 4.32. Distribution of the time averaged temperature for a gap of 0 μm at a heat flux of 11.7 kW/m^2 and a liquid temperature of 75°C for (a) a pore size of 50 μm (b) a pore size of 200 μm.

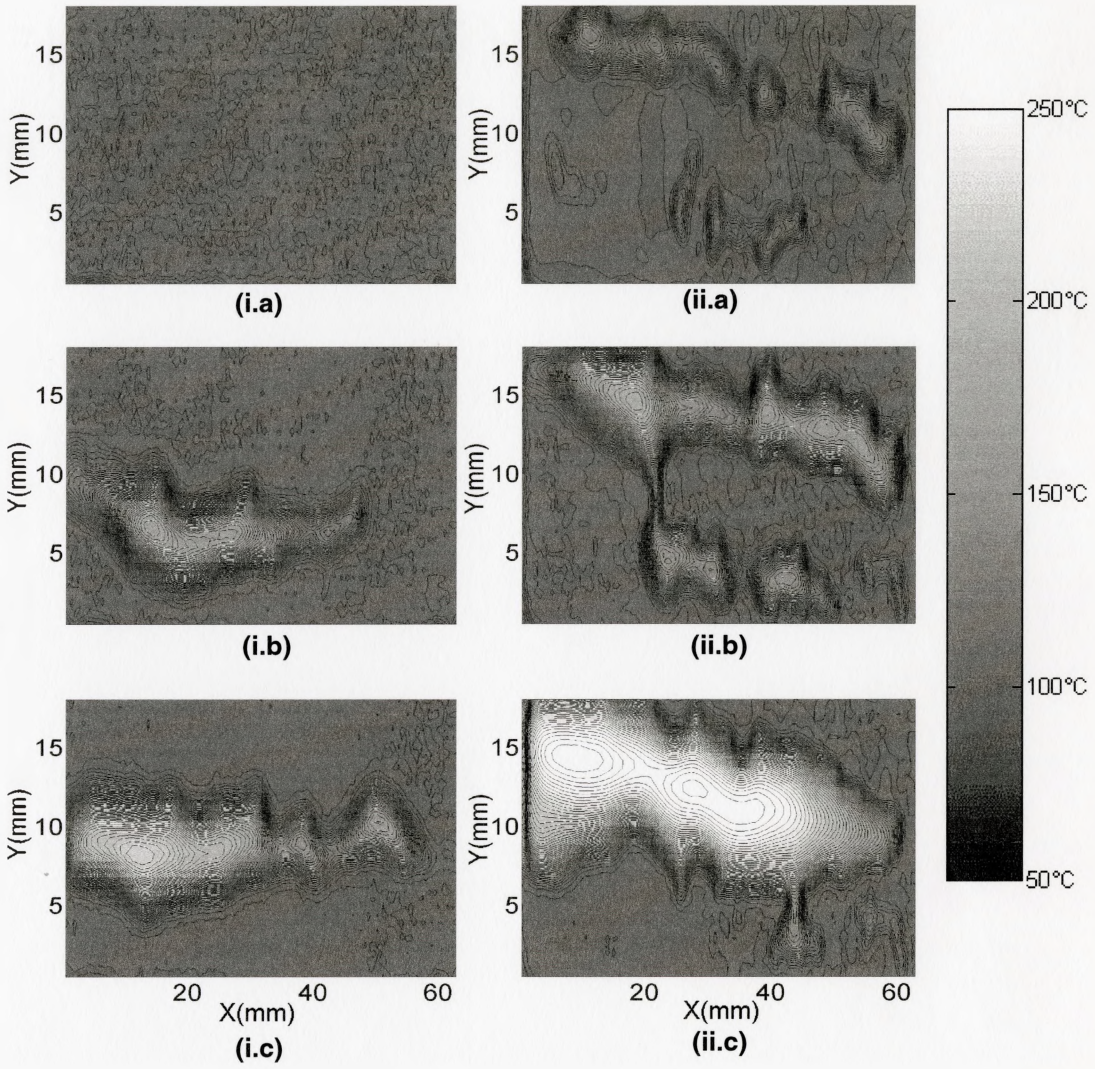

Figure 4.33. Distribution of the time averaged temperature on the foil for a gap of 100 μm for (i) a pore size of 50 μm and (ii) a pore size of 200 μm and (a) an applied heat flux of 11.7 kW/m^2, (b) an applied heat flux of 18.4 kW/m^2, and (c) an applied heat flux of 25.1 kW/m^2.

while for the case of 200 μm pore size the high temperature region expanded on the foil and increased significantly in temperature. Finally, at the heat flux of 25.1 kW/m^2 the high temperature region on the foil further expanded and increased in temperature in both cases.

For a gap height of 200 μm, the time averaged temperature contours for the plates with the two different pore sizes and heat fluxes in the range 11.7 kW/m^2 to 31.7 kW/m^2 are shown in figure 4.34. For the pore size of 50 μm, there were no localized hot spots for heat fluxes up to 18.4 kW/m^2, whereas a localized high temperature region formed at 25.1 kW/m^2, and expanded and increased in temperature at higher heat fluxes. For the 200 μm pore size, however, the region of high temperature formed on the foil at 11.7 kW/m^2 and expanded and increased in temperature with heat flux. Larger high temperature regions were obtained for the case of 200 μm pore size than for 50 μm pore size case. The results for 600 μm gap are presented in figure 4.35. For this gap height, the entire area of the foil had a nearly uniform time averaged temperature near the saturation temperature for both pore sizes and for heat fluxes up to 51.7 kW/m^2. Therefore, it can suggested that the time averaged temperature contours are not dependent on the pore size for the case of 600 μm gap.

The variations of the averaged temperature $\overline{T}_{ave}$ with heat flux for both pore sizes of 50 μm and 200 μm and for gap heights of 100 μm, 200 μm and 600 μm are shown in figures 4.36 through 4.38. The results for the case of 100 μm gap (figure 4.36) show that when the heat flux was increased from 11.7 kW/m^2 to 25.1 kW/m^2, the average temperature $\overline{T}_{ave}$ increased more radically for the plate with 200 μm pores. For the

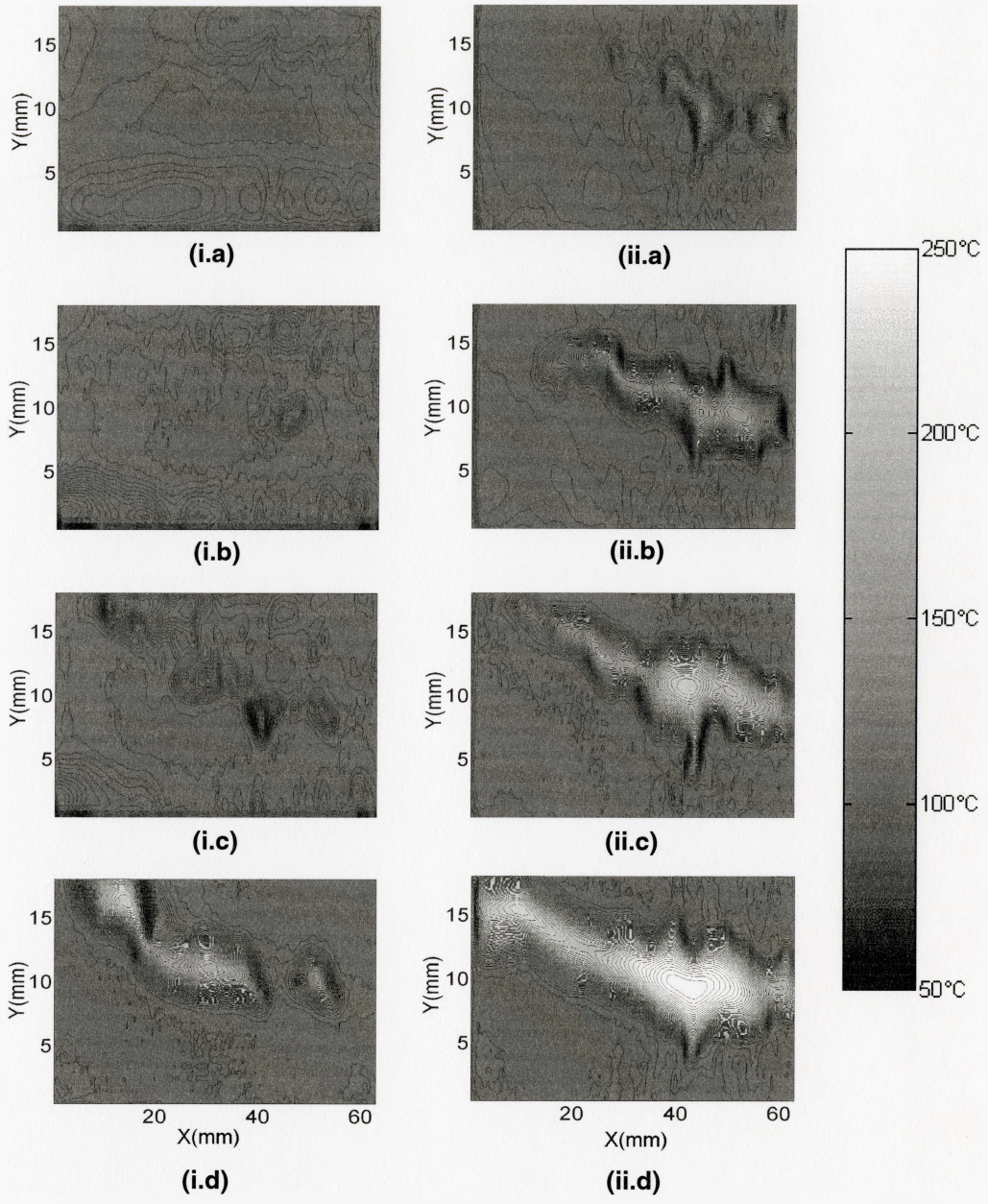

Figure 4.34. Distribution of the time averaged temperature for a gap of 200 μm, (i) a pore size of 50 μm (ii) a pore size of 200 μm and applied heat fluxes of (a) 11.7 kW/m^2, (b) 18.4 kW/m^2, (c) 25.1 kW/m^2 and (d) 31.7 kW/m^2.

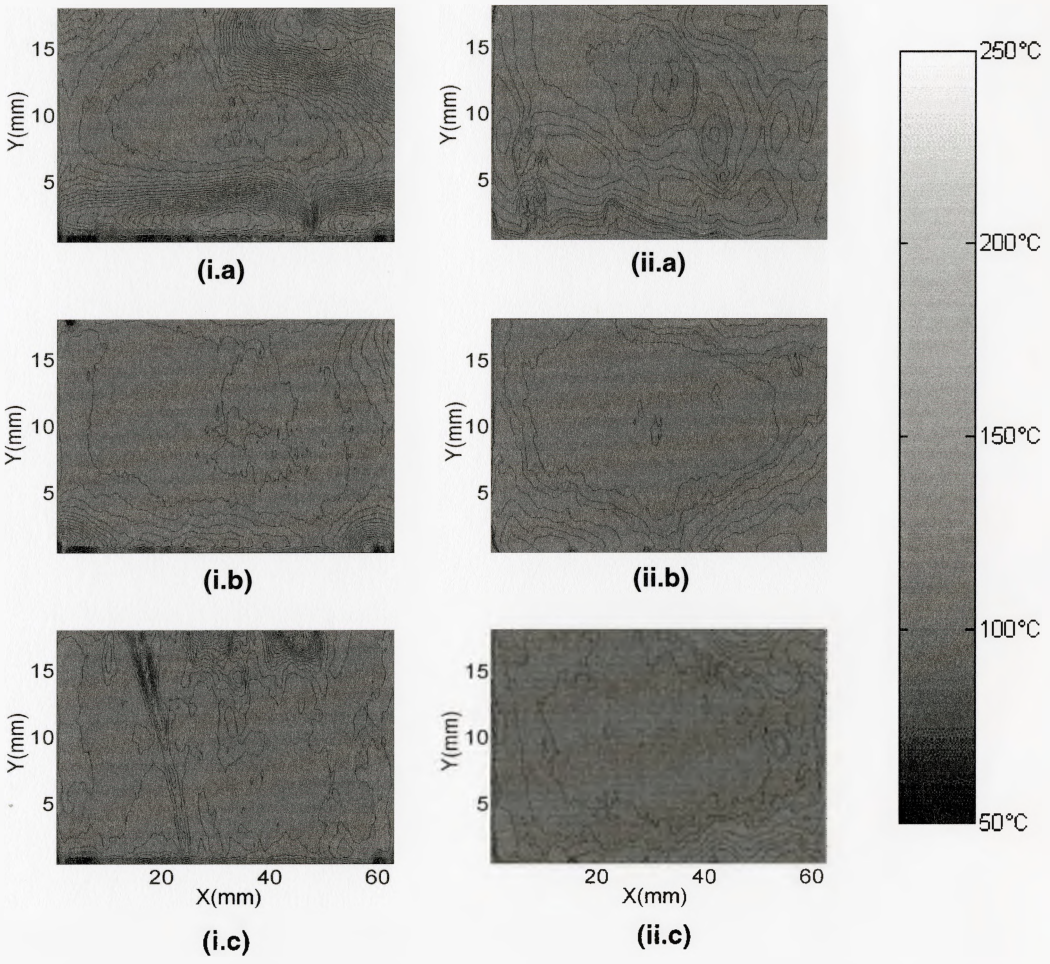

Figure 4.35. Distribution of the time averaged temperature contours for a gap of 600 μm and (i) a pore size of 50 μm (ii) a pore size of 200 μm, at applied heat fluxes of 11.7 kW/m^2, (b) 31.7 kW/m^2 and (c) 51.7 kW/m^2.

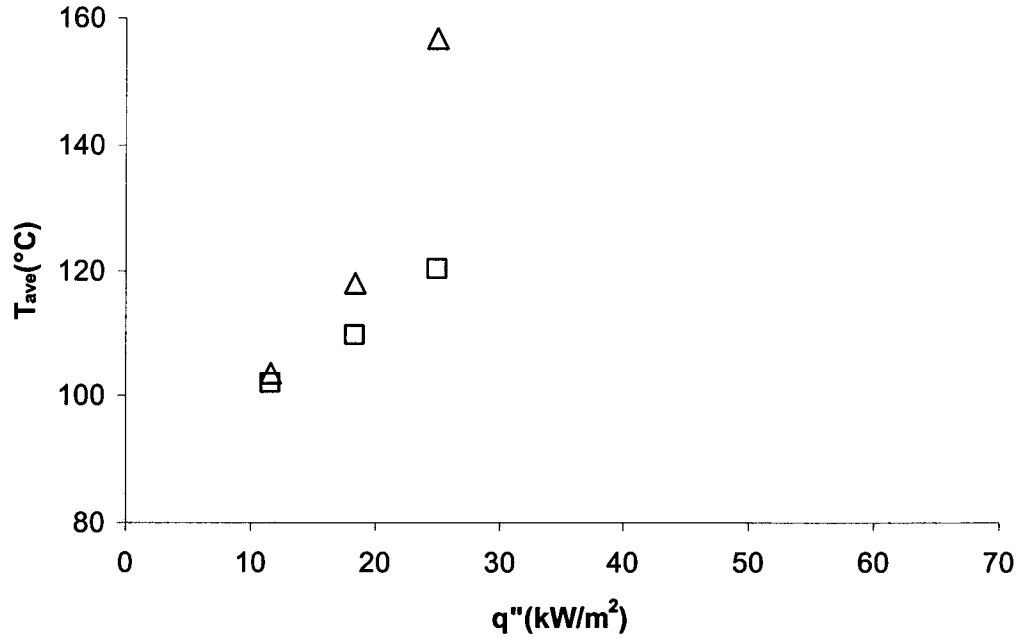

Figure 4.36. Comparison of the average temperature T_{ave} for a gap of 100 μm on the plates with □ 50 μm pore size , Δ 200 μm pore size.

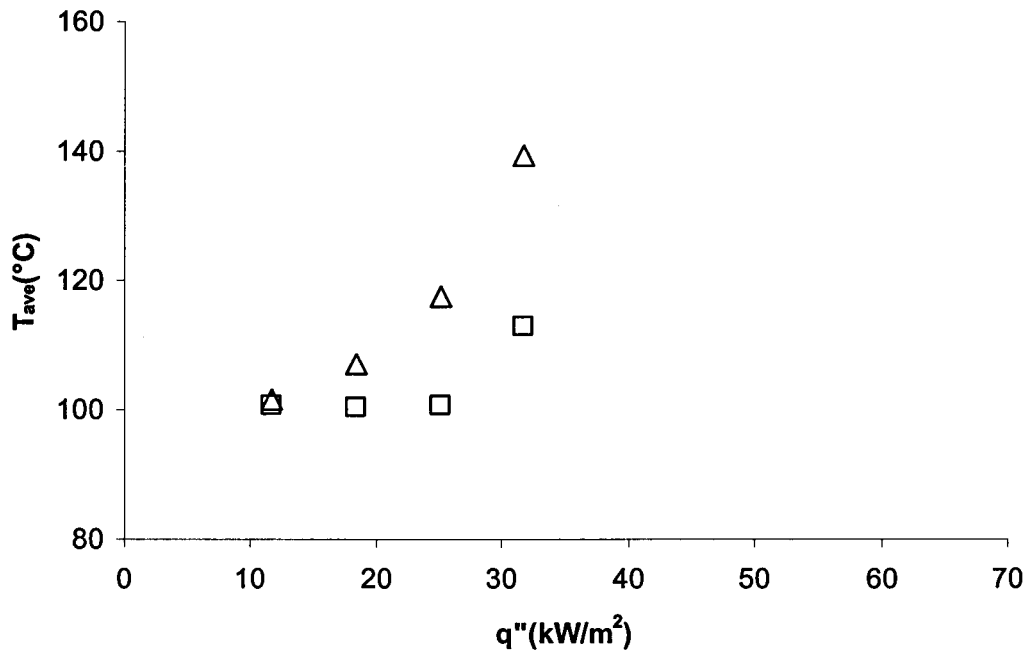

Figure 4.37. Comparison of the average temperature $\overline{T}_{ave}$ for a gap of 200 μm on the plates with □ 50 μm pore size , Δ 200 μm pore size.

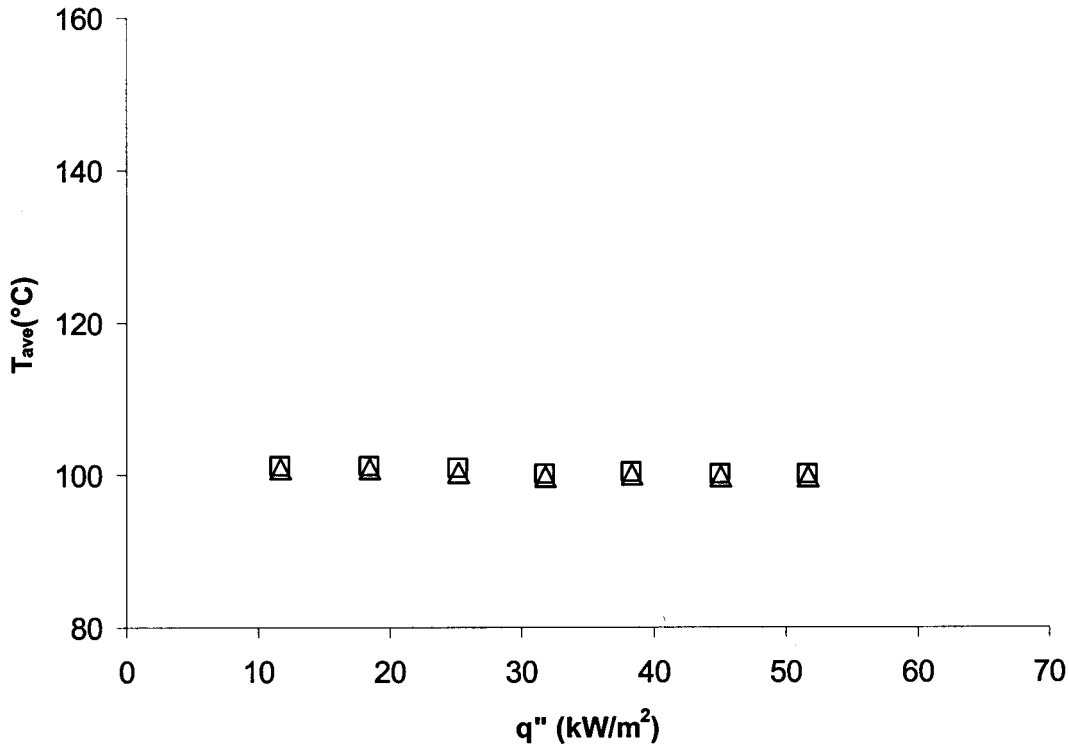

Figure 4.38. Comparison of the average temperature $\overline{T}_{ave}$ for a gap of 600 μm on the plates with □ 50 μm pore size , Δ 200 μm pore size.

200 μm gap, shown in figure 4.37, higher temperatures were again obtained for the 200 μm pore size cases but the difference was smaller than the 100 μm gap. When the heat flux was increased from 11.7 kW/m^2 to 31.7 kW/m^2, the averaged temperature increased from 101°C to 140°C for the 200 μm pore size, while it increased only to 113°C for the 50 μm pore size. At a gap height of 600 μm, the average temperature $\overline{T}_{ave}$ was nearly constant at 100°C for both pore sizes up to a heat flux of 51.7 kW/m^2. This suggests that at this gap height, the heat transfer performances were similar for the cases of 50 μm and 200 μm pore sizes.

The time averaged probability density function of the temperature distributions on the foil at 200 μm gap for the plates with 50 μm and 200 μm pore sizes are shown in figures 4.39.a and 4.40.a respectively. For the plate with 50 μm pore size and an applied heat flux of 11.7 kW/m^2, the temperature distribution was broad between 99.6°C and 103°C with a peak at the saturation temperature, suggesting that both superheated regions and saturated regions were present on the foil. When the heat flux was increased to 18.4 kW/m^2 the probability of the temperature distribution between 100°C and 103°C decreased and there was a sharp peak near 100°C, indicating that most of the heating foil was at the saturation temperature. For the case of 200 μm pore size however (fig. 4.39.a), the temperature distribution was broad between 99°C and 103°C with a peak at the saturation temperature for a heat flux of 11.7 kW/m^2, and when the heat flux was increased to 18.4 kW/m^2 the temperature distribution was broader while the peak near the saturation temperature did not sharpen. In this case, the temperature distribution on a logarithmic scale (fig. 4.40.b) indicates that the maximum temperature on the foil

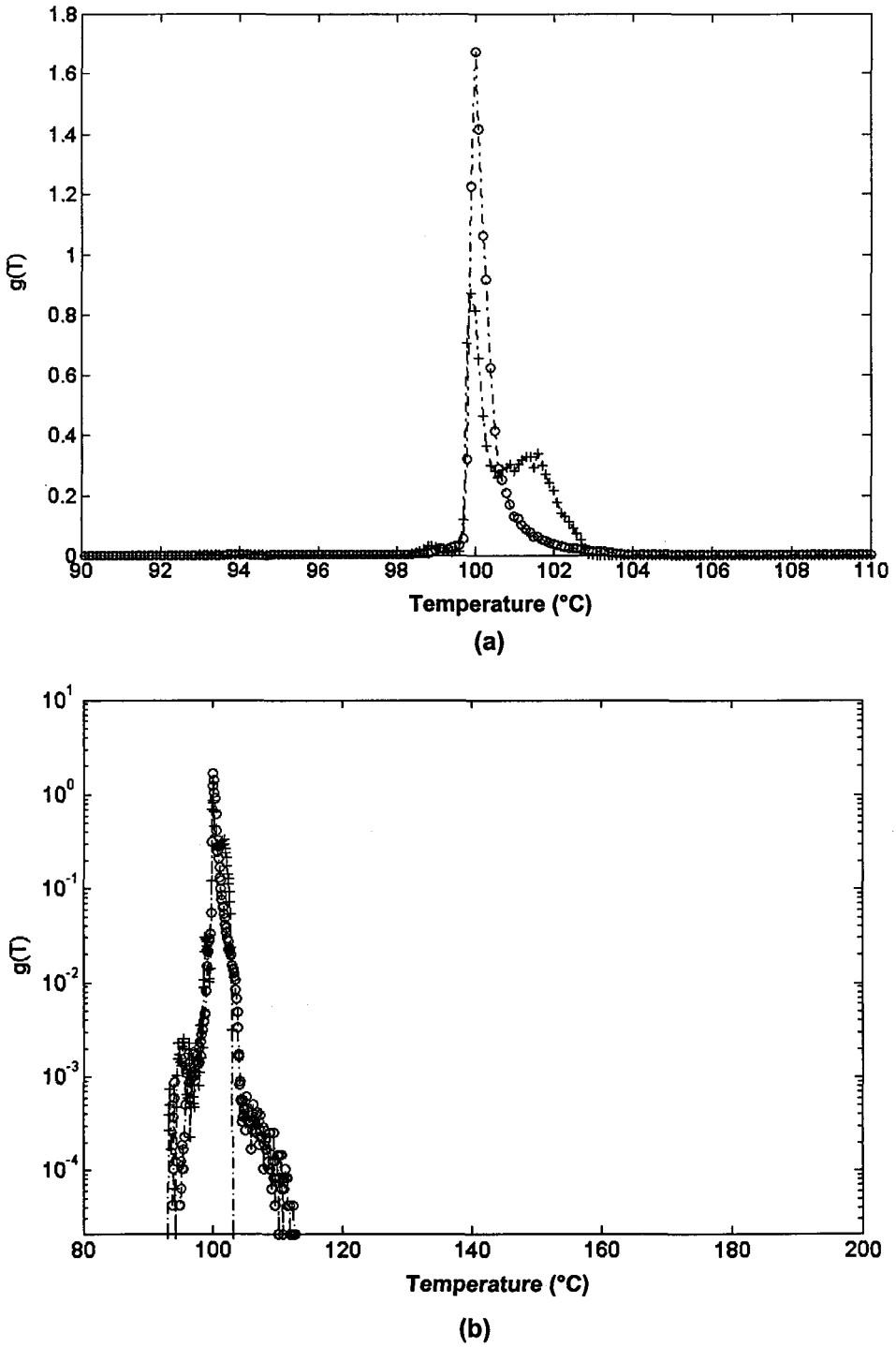

Figure 4.39. Temperature distribution on the foil surface for a gap of 200 μm and a pore size of 50 μm, and at heat fluxes q″ of + 11.7 kW/m^2, o 18.4 kW/m^2 for (a) linear scale, (b) logarithmic scale.

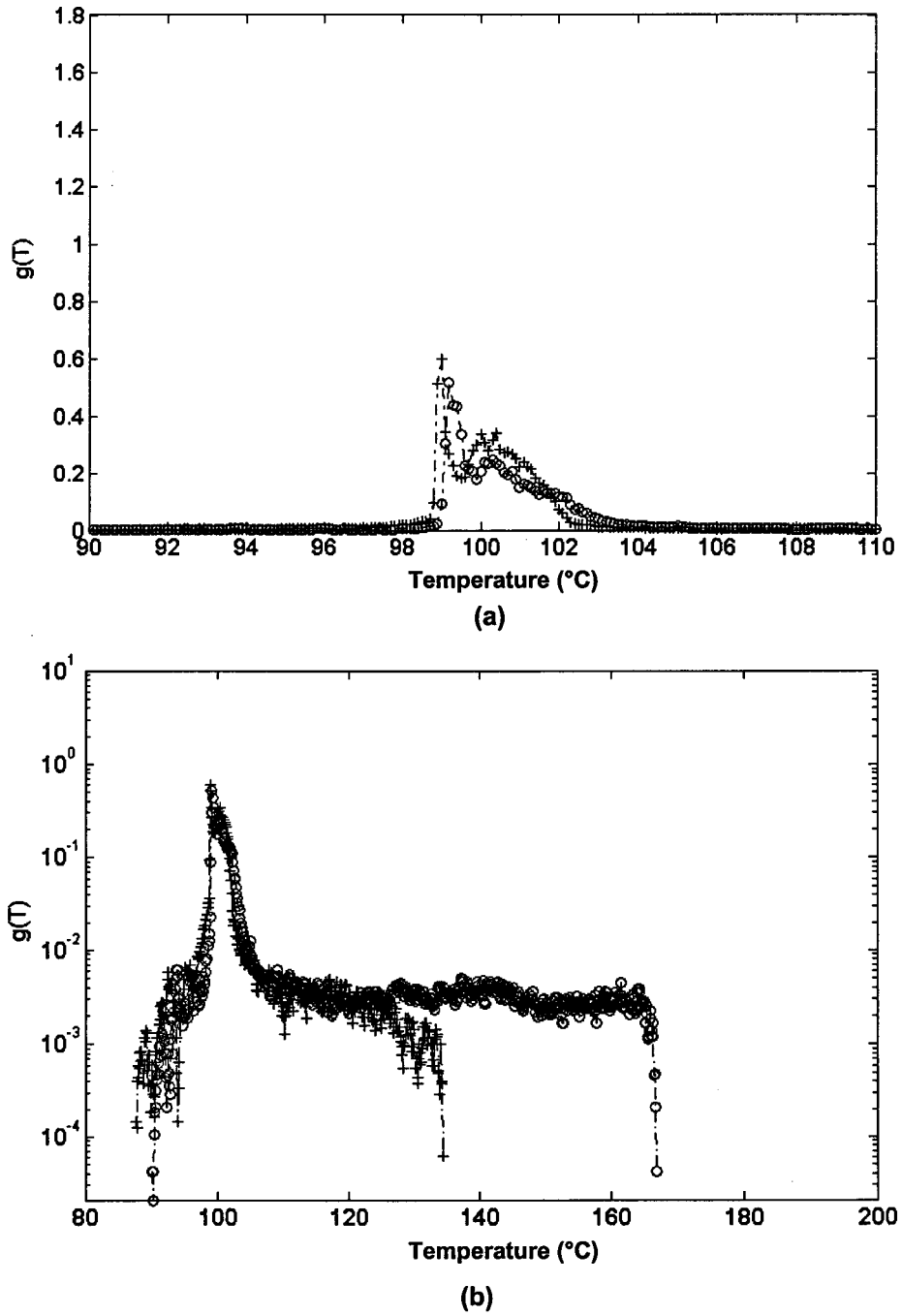

Figure 4.40. Temperature distribution on the foil surface for a gap of 200 μm and a pore size of 200 μm and at heat fluxes q″ of + 11.7 kW/m^2, ○ 18.4 kW/m^2 for (a) linear scale, (b) logarithmic scale.

increased from 135°C to 167°C due to the expansion of the high temperature region on the foil shown previously in figures 4.34.ii.a and 4.34.ii.b, while the maximum temperature increased only from 103°C to 113°C (fig. 4.39.b) for the plate with 50 μm pore size when the heat flux was increased from 11.7 kW/m^2 to 18.4 kW/m^2 due to the formation of moderate high temperature regions on the foil surface (figure 4.34.i.b).

The increase in heat flux for the 200 μm pore size was not accompanied by a sharpening in the peak at the saturation temperature, but it was accompanied by an increase in the maximum temperature in the high temperature region from 135°C to 167°C. It is thought that in this case not all the generated vapor moved laterally through the gap to cool the heating surface by thin film evaporation, but part of the vapor would rather penetrate into the pores, since in this case the pore and the gap size have the same dimension, to form a vapor zone in the wick. Although there are no additional measurements to confirm the presence of the vapor zone in the wick, it is thought that the vapor zone contacts the heating surface which would increase significantly the thermal resistance by forming high temperature regions on the foil (eg. fig. 4.34.ii.a, fig 4.34.ii.b). For the case of the 50 μm pore size however, it is thought that the increase in heat flux was accompanied by an increase of the vapor moving through the gap without travelling through the porous media, which would make most of the heating foil surface cooled by thin film evaporation and result in a sharp temperature concentration around the saturation temperature.

The difference in the results presented above suggest that there are different mechanisms for the vapor generated in the gap to escape. In particular, part of the vapor

could leave through the gap to be released at the sides of the foil to the ambient, and the other part could penetrate into the pores and travel through the porous media when the pore size is larger or on the order of the gap size. In this case, the vapor would be more likely trapped in the pores or move through the porous media similar to the mechanism described by Embacher et al(1990) and Figus et al(1996). When the gap size is larger than the pore size, the vapor generated is more likely to move through the gap to be released at the sides. The boiling mechanism in that case could be considered similar to boiling in confined space with an impermeable interference surface as described by Yao et al(1983) and Lee et al(1992). However there were no additional measurements to confirm these mechanisms.

When the gap height was increased to 600 μm (fig.4.41.a-4.42.a), the time averaged temperature distributions for the cases of 50 μm and 200 μm pore sizes show that when the heat flux was increased from 11.7 kW/m^2 to 45.1 kW/m^2, the temperature distribution had one sharp peak near 100°C and a distribution between 100 and 104°C. The probability of the temperature falling in the slightly superheated temperature range decreased as the heat flux increased for both pore sizes. The probability density function of the temperature distributions on a logarithmic scale (fig.4.41.b-4.42.b) show that the temperature distributions extended to a maximum of 107°C for heat fluxes of 11.7 kW/m^2 and 18.4 kW/m^2, and when the heat flux was increased to 45.1 kW/m^2 the temperature distribution extended up to 111°C for the case of a pore size of 50 μm and it extended to 122°C for the case of a pore size of 200 μm due to the formation of reversible high temperature regions on the foil surface.

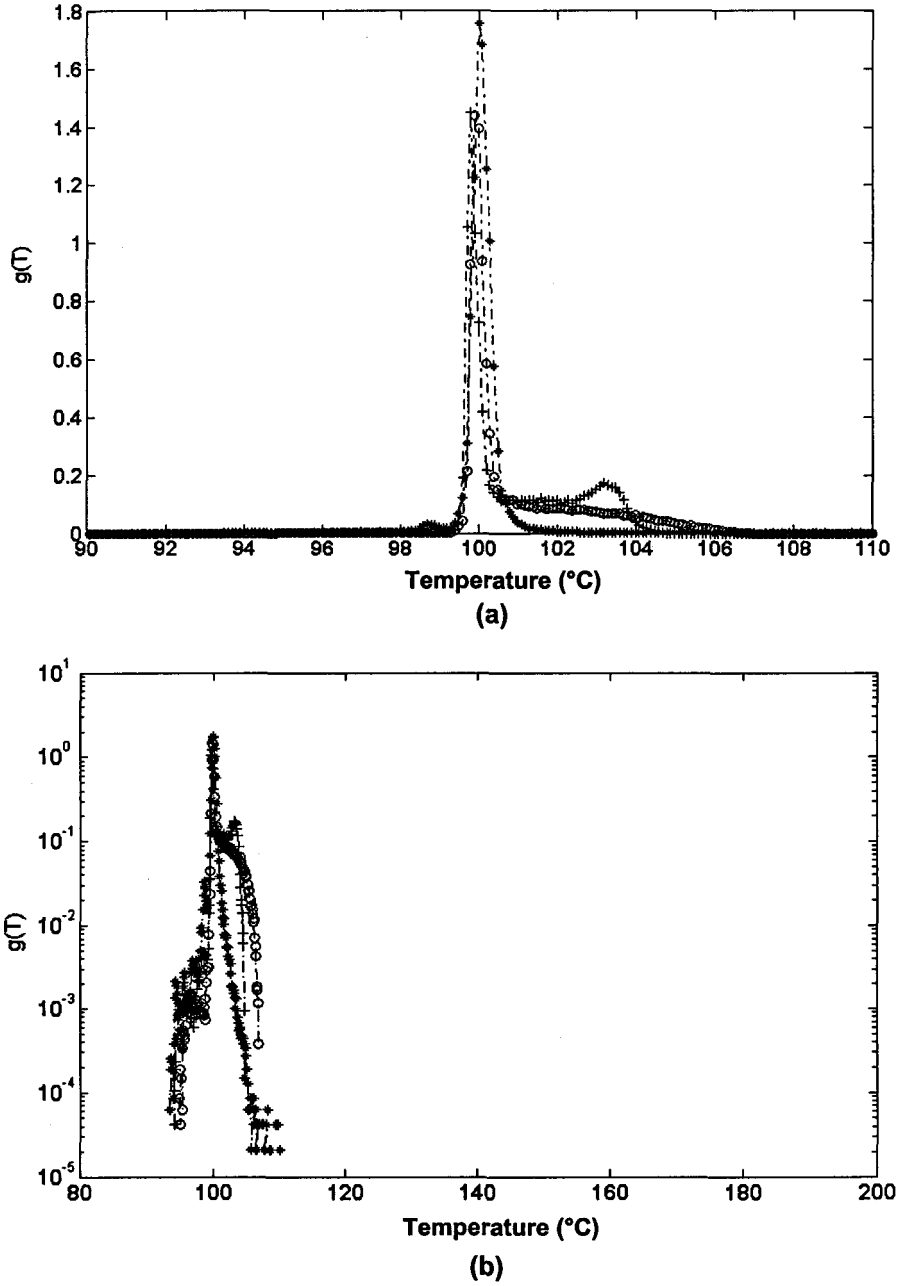

Figure 4.41. Temperature distribution on the foil surface for a gap of 600 μm and a pore size of 50 μm and at heat fluxes q″ of + 11.7 kW/m^2, ○ 18.4 kW/m^2, * 45.1 kW/m^2 for (a) Linear scale, (b) Logarithmic scale.

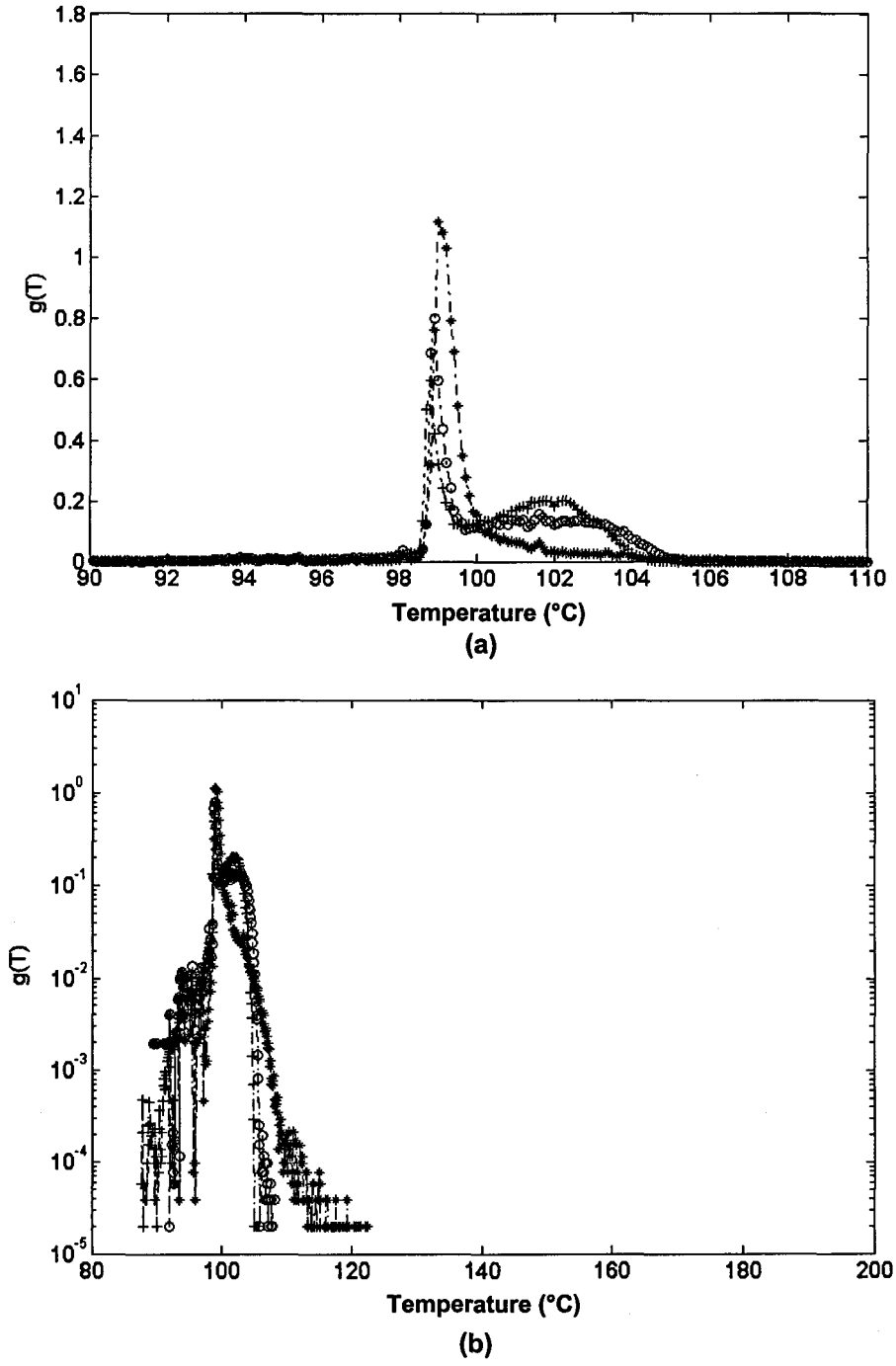

Figure 4.42. Temperature distribution on the foil surface for a gap of 600 μm and a pore size of 200 μm and at heat fluxes q″ of + 11.7 kW/m^2, ○ 18.4 kW/m^2, * 45.1 kW/m^2 for (a) linear scale, (b) logarithmic scale.

The temperature distribution results for a 600 μm gap indicate that for both pore size cases of 50 μm and 200 μm, the increase in the heat flux was accompanied by an increase of the temperature concentration near 100°C. This result could be due to the increase of the foil area cooled by microlayer evaporation in the gap. The vapor bubbles in this case would flow through the gap to be released at the sides of the foil. In these conditions the boiling in the confined space could also be considered similar to confined boiling with an impermeable surface as described by Yao et al (1983) and Lee et al (1992), however, there were no additional measurements to confirm these mechanisms.

The time averaged probability density function of the temperature distribution results for gap sizes of 200 μm and 600 μm suggest that the boiling mechanism in the confined space over the saturated porous plate would be dependent on the gap and the pore size. For a 200 μm gap, the vapor bubbles generated on the foil would likely move through the gap to be released at the sides for a porous plate with a pore size of 50 μm, and they could be partly trapped in the pores to form a vapor zone for the case of the 200 μm pore size. When the gap height was increased to 600 μm, the vapor bubbles nucleating on the foil would flow through the gap to be released at the sides for both the 50 μm and 200 μm pore size cases.

4.4. Discussion and proposed model.

When the gap height was increased from 0 μm to 1000 μm , a liquid meniscus was observed to be formed between the foil and the porous plate (fig.4.43), and the liquid is thought to be maintained in the confined gap due to the dominance of the capillary

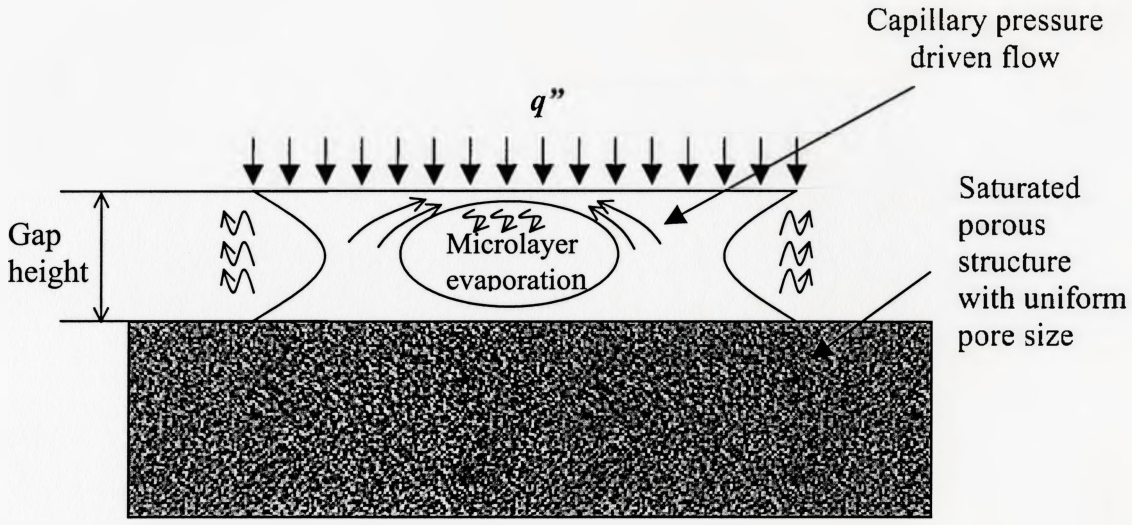

Figure 4.43. Schematic of the proposed heat transfer mechanisms during boiling in a confined gap over a saturated porous structure.

forces over the gravity forces. This relative effect can be estimated using the Bond number given by

$$Bo_{gap} = \sqrt{\frac{(\rho_l - \rho_g)gS}{\sigma/S}} = \frac{Gravtational\ Force}{Capillary\ Force} \tag{4.2}$$

As the gap height was increased from 100 μm to 1000 μm the Bond number was increased from 0.04 to 0.4.

When the heat flux was applied, vapor bubbles would nucleate on the heating surface. The boiling mechanisms and the heat transfer performance in this case were observed to be dependent on the gap size and the pore size. When $\beta \leq 1$, β being the ratio between the gap height and the pore size, the vapor bubbles are thought to be partly trapped in the pores and flow through the porous structure to form a vapor zone in the wick as proposed by Platel et al(1996). This vapor zone would then correspond to the high temperature regions that occurred on the foil surface for the case of $\beta \leq 1$. The vapor zone in the wick would limit the heat transfer performance of the phase change process similar to what was described by Embacher et al(1990), Demidov et al(1994), Khrustalev et al(1995) and Figus et al(1996). However, there were no additional measurements to confirm the penetration of the vapor bubbles into the pores and the formation of the vapor zone in the wick, which makes the identification of the heat transfer mechanism in this case a difficult task.

For the case of $\beta > 1$, the heat transfer performance is thought to become more independent of the pore size of the wick structure. In this case, the vapor bubbles likely do not penetrate into the saturated wick as suggested again by Platel et al(1996). The

boiling in the confined gap over the saturated porous structure would be similar to confined boiling with an impermeable surface as described by Yao et al (1983) and Lee et al (1992). It is thought that in these conditions and at each gap height, the microlayer evaporation to the vapor bubbles in the gap maintains the temperature of the foil nearly uniform as the heat flux was increased. Although there were no additional measurements to confirm the microlayer evaporation mechanism in the gap, it was observed that the increase in the heat flux applied to the foil was accompanied by an increase of the temperature concentration on the foil around the saturation temperature. At a critical value of the heat flux, the time scale of the vapor expansion in the gap $\left(\frac{\rho_g h_{fg} S}{q''}\right)$, defined as the time at which the vapor bubble diameter reaches the gap height S (Yao et al 1983), becomes so small that part of the evaporative microlayer would dry out, leading to the formation of high temperature regions over the heating surface. One way to increase the time scale of the vapor expansion in the gap was to increase the gap height. This would allow more vapor to be generated without partial dry out of the microlayer and consequently increase the critical heat flux. Thus, the critical heat flux increased when the gap was increased from 100 μm to 600 μm. For larger gaps, the results at 1000 μm suggest that the effect of the gravity forces begin to increase compared to the capillary forces in the gap. This would reduce the rate of the liquid replenishment to the evaporative microlayer, and as a result, the microlayer would dry out partially at lower heat fluxes as compared with the 600 μm gap case.

The effect of the liquid subcooling was investigated by performing experiments at subcooled liquid temperatures of 60°C, 75°C and 90°C. The results in all cases had similar characteristics, and it can be suggested that the subcooling level does not have a significant effect on the boiling over the saturated porous structure. It is thought that the liquid gets preheated to a temperature close to the saturation temperature as it flows through the porous structure before reaching its upper surface. This is contrary to what was reported by Zhao et al (2000), because in their case the porous structure was not a thermally conductive material. The wick structure used in that case consisted of separated copper cylinders with a characteristic pore size of approximately 1 mm.

Chapter 5. Conclusions and Recommendations

5.1. Conclusions

The heat transfer in a partially heated saturated porous structure was investigated to understand the heat transfer mechanisms in the evaporator of a capillary pumped loop. A thin stainless steel resistive foil heater stretched between two copper electrodes was used to heat the saturated porous plate surface and a high speed thermal imaging camera was used to determine the unsteady surface temperature distribution on the foil. Measurements were performed at different gap heights between a heater surface and porous plates with pore sizes of 50 μm and 200 μm. It was observed that the boiling was dependent on the gap height and the pore size. For the case where $\beta \leq 1$, a high thermal resistance was obtained, and it is thought that this is due to the penetration of the vapor bubbles into the pores. This result in the formation of a vapor zone in the wick that would limit the heat transfer performance of the phase change process as suggested by Embacher et al(1990), Demidov et al(1994), Khrustalev et al(1995) and Figus et al(1996). However, there were no additional measurements to confirm the presence of the vapor zone in the wick. For the case where $\beta > 1$, the boiling could be considered similar to confined boiling with an impermeable surface. For this case, the foil temperature was initially constant and then started to increase as high temperature regions formed on the

foil surface. It is thought that this is due to the formation of dry regions on the heating surface as suggested by Yao et al(1983). When the gap height was increased to 600 μm, the maximum heat flux increased because of the increase of the time scale of the vapor expansion in the gap (Yao et al 1983). At higher gap heights, the critical heat flux decreased due to the decrease of the capillary pressure in the gap, which is thought to be one mechanism driving the liquid to the evaporative microlayer as suggested by Lee et al(1992). Therefore an optimal gap would exist between the heating surface and the saturated porous structure for maximum heat transfer.

The effect of the subcooled liquid temperature was investigated by performing experiments with subcooled liquid temperatures of 60°C, 75°C and 90°C. It was observed that the subcooled liquid temperature did not have a significant effect on the heat transfer characteristics. This was attributed to the preheating of the liquid in the porous structure.

5.2. Recommendations

The experimental facility used in this study allowed us to study the confined boiling in the gap between a saturated porous plate and a heated surface by measuring the unsteady temperature distribution on the heating surface. However, no measurements were performed to determine the phase distribution in the wick. Also, no information was obtained on possible vapor nucleation in the subcooled liquid on the immersed surface of the porous structure. It would then be useful to measure the temperature in the porous structure at different locations, and perform a visual investigation of the immersed surface of the porous plate. This is important because the formation of vapor zones in the

liquid core of the capillary evaporator would present a serious limitation to its steady state operation.

In this study, it was observed that an optimal gap height between the porous structure and the heater surface exists for maximum heat transfer. However, the effect of the heater width relative to the pore size was not investigated. This would be important to understand the applicability of the results of this investigation to the evaporator of a CPL.

References

[1] Bendat J.S, Piersol A.G, " Engineering applications of correlation and spectral analysis", John Wiley & Sons, 1980.

[2] Cao Y., Faghri A., "Analytical solutions of flow and heat transfer in a porous structure with partial heating and evaporation on the upper surface", International Journal of Heat and Mass Transfer, Vol. 37, pp 1525-1533, 1994.

[3] Cao Y., Faghri A., "Conjugate analysis of a flat-plate type evaporator for capillary pumped loops with three-dimensional vapor flow in the groove" , International Journal of Heat and Mass Transfer, Vol. 37, pp 401-109, 1994.

[4] Demidov A. S., Yatsenko E. S. " Investigation of heat and mass transfer in the evaporation zone of a heat pipe operating by the 'inverted meniscus' principle", International Journal of Heat and Mass Transfer, Vol. 37, pp 2155-2163, 1994.

[5] Dupont V. , Joly J. L., Miscevic M., Platel V.,"Capillary Pumped Loop Startup: Effects of the Wick Fit on Boiling Incipience", Journal of Thermophysics and Heat Transfer, Vol. 17, pp 138-144, April-June 2003.

[6] Embacher E., Wulz H. G.," Capillary pumped loops for space applications: experimental and theoretical studies on the performance of capillary evaporator designs ", 5th Joint Thermophysics and Heat Transfer Conference, Seattle WA., USA, Paper AIAA-90-1739, 1990.

[7] Faghri, "Heat Pipe Science and Technology", Taylor and Francis, Washington, DC, 1995.

[8] Figus C., Bories S., Prat M, " Investigation and analysis of a porous evaporator for a capillary pumped loop", PD-Vol. 78, Engineering Systems Design and Analysis, ASME, Vol. 6, pp 99-106, 1996.

[9] Figus C., Dunbar N., Bories S., Supper W., "Experimental evaluation of a novel microscopic model of a capillary pumped evaporator", Proceedings of the Sixth European Symposium on Space Environmental Control Systems, ESA Publication Division, pp. 377-383, 1998.

[10] Figus C., Le Bray Y., Bories S., Prat M., "Heat and mass transfer with phase change in a porous structure partially heated: continuum model and pore network simulations" , International Journal of Heat and Mass Transfer , Vol. 42, pp 2557-2569, 1999.

[11] Figus C., Ounougha L., Bonzom P., Supper W., Puillet C., "Capillary fluid developments in Astrium", Applied Thermal Engineering, Vol. 23, pp 1085-1098, 2003.

[12] Fujita Y., Ohta H., Uchida S., Nishikawa, "Nucleate boiling heat transfer and critical heat flux in narrow space between rectangular surfaces", International Journal of Heat and Mass Transfer, Vol. 31, pp 229-239, 1988.

[13] Gao N., "Heat transfer enhancement in impinging round jets", M.A.Sc Thesis, Department of Mechanical Engineering, McMaster University, 2000.

[14] Huplik V., Raithby G. D., "Surface Tension effects in boiling from a downward facing surface", Journal of Heat Transfer, Vol. 92, pp 403-409, 1972.

[15] Incropera F. P., Dewitt D. P., "Introduction to heat transfer", Wiley, 1990.

[16] Ishibashi E., Nishikawa K., "Saturated boiling heat transfer in narrow spaces", International Journal of Heat and Mass Transfer, Vol. 12, pp 863-894, 1969.

[17] Ishigai S., Inoue K., Kiwaki Z., Toshiki I., "Boiling heat transfer from a flat surface facing downward", Proceedings of the 1961-1962 International heat transfer conference; Boulder, Colo, pp 224-229.

[18] Katto Y., Yokoya S., Teraoka K., "Nucleate and Transition Boiling in a Narrow Space between two Horizontal, Parallel Disk-Surface", Bulletin of the JSME, Vol. 20, pp 638-643. 1977.

[19] Khrustalev D., Faghri A., " Heat transfer in the inverted meniscus type evaporator at high heat fluxes ", International Journal of Heat and Mass Transfer, Vol. 38, pp 3091-3101, 1995.

[20] Kline S. J., McClintock F. A., "Describing uncertainties in single-sample experiments", Mechanical Engineering, Vol. 78, pp 3-8, 1953.

[21] Kenning D.B.R., Kono T., Wienecke M., "Investigation of boiling heat transfer by liquid crystal thermography", Experimental Thermal and Fluid Science, Vol. 25, pp 219-229, 2001.

[22] LaClair T. J., Mudawar I., "Thermal transient in a capillary evaporator prior to the initiation of boiling", International Journal of Heat and Mass Transfer, Vol. 43, pp 3937-3952, 2000.

[23] Lee M. T., Yang Y. M., Maa J. R., "Nucleate pool boiling in a confined space", Chemical Engineering Communication Vol. 117, pp 205-217, 1992.

[24] Passos J.C., Hirata F.R., Possamai L.F.B., Balsamo M., Misale M., "Confined boiling of FC72 and FC87 on a downward facing heating copper disk", International Journal of Heat and Fluid Flow, Vol. 25, pp 313-319, 2004.

[25] Platel V., Fudym O., Butto C., Briend P, "Heat transfer coefficient at vaporization interface of a two phase capillary pump ". Revue Generale de Thermique, Vol. 35, pp 592-598, 1996.

[26] Platel V., Butto C., Fudym O., Laurens M., "Experimental study and evaluation of a two phase capillary pumped loop performance", Revue Generale de Thermique, Vol. 34, pp 315-324. 1995.

[27] Pratt D. M., Brown J. R., Hallinan K. P., "Thermocapillary effects on the stability of a heated curved meniscus" , Transactions of the ASME, Vol. 120, pp 220-226, 1998.

[28] Theofanous T. G., Tu J. P., Dinh A. T., Dinh T. N., "The boiling crisis phenomenon part I: Nucleation and nucleate boiling heat transfer", Experimental Thermal and Fluid Science, Vol. 26, pp 775-792, 2002.

[29] Theofanous T. G., Tu J. P., Dinh A. T., Dinh T. N., "The boiling crisis phenomenon part II: Dry out dynamics and burn out", Experimental Thermal and Fluid Science, Vol. 26, pp 793-810, 2002.

[30] Tokos C. P., "Probability distributions: An introduction to probability theory with applications" , Duxbury Press, 1972.

[31] Wulz H. G., Mayinger F., " Heat and fluid transport in an evaporative capillary pump", International Journal of Energy Research, Vol. 16, pp 879-896, 1992.

[32] Yan Y. H., Ochterbeck J. M., "Numerical Investigation of the steady state operation of a cylindrical capillary pumped loop evaporator", Journal of Electronic Packaging, Vol. 125, pp 251-260, 2003.

[33] Yao S., Chang Y., "Pool boiling heat transfer in a confined space", International Journal of Heat and Mass Transfer, Vol. 26, pp 841-848, 1983.

[34] Zhao T.S., Liao Q., "On capillary-driven flow and phase-change heat transfer in a porous structure heated by a finned surface: measurements and modeling", International Journal of Heat and Mass Transfer, Vol. 43, pp 1141-1155, 2000.

[35] Zhao T. S., Liao Q., "A visual study of phase-change heat transfer in a two dimensional porous structure with a partial heating boundary", International Journal of Heat and Mass Transfer, Vol. 43, pp 1089-1102, 2000.